LAB-ON-CHIP MICRODEVICES FOR CAPTURING, IMAGING AND COUNTING WHITE BLOOD CELLS

by

Anurag Tripathi

A dissertation submitted in partial fulfillment
of the requirements for the degree of
Doctor of Philosophy
(Mechanical Engineering)
in The University of Michigan
2012

Doctoral Committee:

Associate Professor Nikolaos Chronis, Chair
Associate Professor Katsuo Kurabayashi
Assistant Professor Jianping Fu
Assistant Professor Sunitha Nagrath

To The Almighty

And

To My Family & Friends

ACKNOWLEDGEMENTS

It is my honor and absolute pleasure to acknowledge people who made this thesis possible. First and foremost, I would like to thank my advisor Dr. Nikos Chronis whose guidance and training enabled me to develop skills in microfabrication and microfluidics technology. More than the technical knowledge I gained from Dr. Chronis in the past five years, he taught me the virtues of hard work, sincerity and integrity. In the toughest of situations, his patience and understanding provided me with courage and confidence and enabled me to see through those hard times. He inculcated a strong aptitude for research in me and his 'never give up' principle left an indelible impression on my problem solving approach. I would be eternally grateful to Dr. Chronis for mentoring me and transforming me into a better researcher and a better human being.

A big gratitude is in order for the other three members of my thesis dissertation committee, Dr. Katsuo Kurabayashi, Dr. Jianping Fu and Dr. Sunitha Nagrath. It was a privilege to have them on my committee. I thank them wholeheartedly for their valuable inputs during the Ph.D. preliminary examinations. I acknowledge the encouragement they provided to my research and would like to thank them for their support and motivation all this while.

The years I spent in the Chronis' Lab were full of unlimited fun and learning thanks to the wonderful labmates I had the privilege to share my workspace with. I

would like to thank Trushal Vijaykumar Chokshi for being a great friend, colleague and mentor. I relish the great times we had discussing research and non-research topics and I learnt immensely from his clarity of thought and vision. I gratefully acknowledge the camaraderie and the intellectual and emotional support provided by Mostafa Ghannad-Rezaie, Daphne Bazopoulou, Eleni Gourgou, Rahman Sabahi-Kaviani, Alexandros Pantazis, Ning Gulari and Philip Choi. I would also like to thank Suhasa B Kodandaramaiah, Ani Siyahian, Gokul Ramaswami, Spencer Marsh and Amrita Ray Chaudhury for their companionship. I acknowledge the past and the present members of the labs of Prof Katsuo Kurabayashi, Prof Edgar Meyhofer and Prof Jianping Fu for the stimulating research discussions.

I acknowledge the National Institutes of Health (NIH) for supporting my education and research at the University of Michigan through the NIH Director's New Innovator Award #DP2OD006458. I also thank the Mechanical Engineering Department at the University of Michigan and the Rackham Graduate School for conferring upon me the Departmental and the Predoctoral Fellowships respectively. I would like to thank the staff of the Lurie Nanofabrication Facility for their help and guidance in the fabrication of the devices presented in this thesis. I also acknowledge the fabrication support provided by the Georgia Institute of Technology Nanotechnology Research Center. I would also like to thank the Mechanical Engineering staff for doing everything they could to make our work smooth and easy. Special thanks to Kelly Chantelois, Patty Freundl, Matt Navarre, Mike Lazarz and the ME Academic Service Office staff for their help and support over the years. Thanks are in order for Dr. James Riddell IV for his help and guidance with the biochip experiments.

The great time I had in Ann Arbor would not have been possible without my great friends Naveen Kumar Gupta, Ashwini Kumar, Jayesh Gaur, Shantanu Gupta, Abhishek Kumar and Karthik Visvanathan. They created a 'home away from home' for me and I was very fortunate to be in their company. I acknowledge all my cricket teammates as well as the racquetball club members for the great joy and thrill I experienced playing alongside them. I thank Razaik Singh, Kaustubh Pandit, Tejkaran Gill, Ashwini Kamath, Aalap Doshi, Komal Anand, Siddharth Saxena and all the friends in Ann Arbor for the fun times I had in their company. I would like to thank Rahul Luthra, Nikhil Jog, Cherian Joseph, Rupal Jain, Anjali Rawat and my friends in India and all over the world for their friendship and support.

Lastly, none of this would have been possible without the love and support of my family. I am grateful to the Almighty who blessed me with the most loving and caring parents in Mridula and Ravindra Nath Tripathi and the most wonderful brother in Anupam Tripathi. They believed in my capabilities in the toughest of times when my confidence itself had wavered and provided me with their unconditional love and support. I have also been blessed with the most lovely and caring wife in Bhavini Tewari who has become my pillar of strength in the short time that we have been together. These people make my world and mean everything to me and I thank them for being there in my life. I would also like to thank the members of my extended family in India and in Ann Arbor for always showering their boundless love on me and for wishing for my happiness, success and wellbeing. I would like to acknowledge the contributions of all my friends and colleagues whom I might have inadvertently missed out on in this acknowledgement.

Table Of Contents

Dedication……...ii

Acknowledgements……...iii

List of Figures……x

List of Appendices……...xvi

Abstract……..xvii

Chapter 1 INTRODUCTION……...……1

1.1 Motivation……..1

1.2 Blood: a major disease biomarker……..3

1.2.1 Flow cytometry for counting WBCs and their subtypes….....5

1.3 Thesis Objective…….8

1.3.1 Microfluidics for lab-on-a-chip systems…….....11

1.3.2 Research goals……12

1.4 Thesis Organization…….15

Chapter 2 Literature Review……17

2.1 Introduction……..17

2.2 Microfluidic biochips for WBC capture and enumeration……..18

2.2.1 Size-based capture of WBCs……..18

2.2.2 Immunoaffinity based capture of WBCs....……21

2.3 Microlens arrays for imaging micron-sized biological objects……24

2.3.1 Microlens fabrication methods……...25

2.3.1.1 Fixed focal length microlenses..……26

2.4 Conclusions...……...31

Chapter 3 A 3D Microfluidic Cell Trapping Biochip For Counting White Blood Cells…….....32

3.1 Introduction……..32

3.2 Materials and methods…….36

3.2.1 Materials…….36

3.2.2 Biochip design……36

3.2.3 Biochip microfabrication…….....39

3.2.4 Fluid flow simulations and modeling…….40

3.2.5 Blood sample preparation and biochip operation……...……41

3.2.6 WBC counting……42

3.3 Results……..……43

3.3.1 Uniform pressure and flow rate distribution in the biochip.....43

3.3.2 Maximum WBC trapping efficiency……..47

3.3.3 WBC trapping efficiency versus number of processed WBCs…….49

3.4 Discussion……....51

3.5 Conclusions……..52

Chapter 4 A Polymer-based, Planar Microlens Array For Imaging Micron-Sized Objects……..54

4.1 Introduction…….....54

4.2 Design and microfabrication of the microlens array……56

4.3 Results……..……61

4.4 Conclusions……..72

Chapter 5 A High Numerical Aperture Doublet Microlens Array……..…….73

5.1 Introduction……..74

5.2 Design and microfabrication of the doublet microlens array……...77

5.3 Results and Discussion……81

5.4 Conclusions...……...89

Chapter 6 Conclusions and Future Work...…….....90

6.1 Conclusions…….....90

6.1.1 Microfluidic biochip with a 3D architecture for capturing WBCs……..91

6.1.2 High numerical aperture microlens arrays for imaging micro-objects……...92

6.2 Future Work…….....94

6.2.1 Cell trapping biochip with an integrated volume metering and RBC lysis chamber……..94

6.2.2 Microfluidic-based oil immersion lens array……..96

6.2.3 Integrated biochip for on-chip capture, imaging and counting of WBCs……97

APPENDICES……100

BIBLIOGRAPHY……..117

List Of Figures

Figure 1.1: A scanning electron microscope image of blood cells [adapted from the wikipedia website: http://en.wikipedia.org/wiki/White_blood_cell]. The doughnut shaped cells are the RBCs, the spherical shaped cells are the WBCs and the small disc-shaped cells are the platelets……..4

Figure 1.2: Mechanism by which Fluorescence activated cell sorter (FACS) counts and sorts cells [adapted from http://classes.midlandstech.com, Copyright 2004 Pearson Education, Inc.]..……...7

Figure 1.3: Image of a two-laser FACS Calibur Flow Cytometer [adapted from http://www.georgiahealth.edu/cancer/shared/flow/equipment.html]. The flow cytometer is expensive, bulky, needs electricity and refrigerated reagents and trained personnel for its operation and maintenance…….....8

Figure 1.4: Portable system for obtaining counts of WBCs and their subtypes at the point of care….....……...9

Figure 1.5: Disposable WBC capturing biochip obtained by the integration of microfluidic (cell capturing) and microoptics (cell imaging) components. ….....…….....10

Figure 1.6: Cross-sectional schematic of the WBC counting biochip…….....11

Figure 2.1: The membrane flow cell device for counting CD4+ T-lymphocytes from human blood [adapted from [26]]. (A) Upon processing the whole blood through the flow cell, the white blood cells are captured on the micro holes and the red blood cells and platelets filter through. The arrows indicate the red blood cells filtering through the microholes. (B) Fluorescence image showing T-lymphocytes (stained with fluorescent antibodies) captured on the membrane……..…19

Figure 2.2: Schematic representation of the silicon microfilter designs used for WBC capture [adapted from [27]]. The designs are a) weir filter (side view), b) pillar filter (top view), c) crossflow filter (top view) and d) membrane filter (side view).……20

Figure 2.3: Microfluidic device with protein (E-selectin) functionalized pillars for capturing leukocyte cell lines [adapted from [28]]. (A) Square array of 25x25 μm square posts spaced 25 μm apart. (B) Alternating arrays of thin posts with 30 μm longitudinal post to post spacing and the adjacent rows offset by 15 μm in the flow direction…….22

Figure 2.4: Microfluidic device used for capturing and counting CD4+ T-cells from human whole blood [adapted from [32]]. (A) Schematic of the steps of operation of the CD4+ T-cells counting microdevice. (B) Microfabricated device with dimensions for optimal shear stress to capture T-lymphocytes……...23

Figure 2.5: Schematic representation of a two stage cascaded device for CD4+ T-cell capture [adapted from [33]]. Reduced monocyte contamination results into an increased T-cell capture purity……..24

Figure 2.6: Scanning electron micrographs of the microlenses fabricated using photoresist melting and reflow methods. (A) 1.5 μm in diameter microlenses can be fabricated using this approach [adapted from [35]]. (B) High fill factor square microlens array fabricated using photoresist melt and reflow method [adapted from [36]]……27

Figure 2.7: Ink-jet printing process for fabricating microlenses. (A) Schematic of the ink-jet printing setup for dispensing UV curable polymer [adapted from [37]]. (B) Microscopic image of an array of ink-jet printed microlenses [adapted from [38]]……...28

Figure 2.8: (A) Scanning electron microscope (SEM) image of the microlens fabricated using focused ion beam milling [adapted from [39]]. (B) SEM image of hexagonal microlens array fabricated using femtosecond laser direct writing. A 100% microlens fill factor is obtained using this technique [adapted from [40]]……..29

Figure 2.9: Microlens fabricated by molding various materials against the elastomer (polydimethylsiloxane PDMS) and silicon molds respectively. (A) Schematic of the fabrication of sol-gel glass microlens arrays by molding them against the PDMS mold [adapted from [42]]. (B) SEM image of sol-gel glass microlenses [adapted from [42]]. (C) Microlens mold obtained by the isotropic wet etching of silicon in an acid solution [adapted from [44]]. (D) SEM image of an array of microlenses obtained by molding a UV curable polymer against the isotropically etched silicon mold [adapted from [44]]……..……30

Figure 3.1: (A) 3D illustration of a WBC trapping microhole cluster of the biochip. The cell trapping layer is sandwiched between the top and the bottom microfluidic channels (Top cover is not shown for clarity). (B) A snapshot

of the microfluidic biochip (12 images were obtained with a 5x microscope objective and stitched together). Enlarged view of the trapping holes with the top microfluidic channels was obtained using a 20x microscope objective. A magnified view of an individual microhole cluster (obtained with a 50x microscope objective) has also been presented……..37

Figure 3.2: Schematic of the trapping of WBCs in the microhole array. Fluorescently tagged WBCs suspended in the buffer solution are injected into the biochip under pressure. While the buffer flows through the microhole array, the WBCs are confined and trapped in the microhole array and their squeezing out is prevented by the bottom microfluidic layer. ……38

Figure 3.3: The microfabrication process of the cell trapping biochip. The cell trapping and the sample delivery modules are fabricated separately and subsequently aligned and bonded under an upright microscope using a 5x microscope objective…….40

Figure 3.4: (A) COMSOL geometrical model used to simulate the pressure profile through an individual microhole cluster. The arrows signify the direction of flow into the device, passing through the microhole cluster and the bottom microfluidic layer and subsequently exiting through the outlet channel. The cross section schematic shows the pressure difference across an unoccupied microhole. (B) Pressure profile (in Pa) has been presented for the top plane of the bottom microfluidic layer (indicated in green). The white and the dark circles indicate the occupied and the unoccupied microholes respectively. (I), (II), (III) and (IV) correspond to 0, 18, 31 and 34 microholes occupied in the cluster (out of 37 holes). (C) Maximum pressure difference across a microhole cluster as a function of the % of the microholes (in the cluster) occupied by the cells……...44

Figure 3.5: (A) Resistive electrical circuit to analyze the distribution of flow through different trapping microhole clusters (1-17) along the length of one of the 17 microfluidic inlet arms. $R_{cluster\ 1\text{-}17}$ indicate the fluidic resistances of the microhole clusters 1-17 respectively. All the resistances used for the resistive electrical circuit modeling have been illustrated using a 3D cross section. $R_{connector}$ exceeds any other resistance in the network by at least two orders of magnitude. This resistive circuit was analyzed using LT Spice IV software to obtain the flow rates through each of the 17 microfluidic arms. (B) % of the total flow passing through each of the microhole clusters in the beginning of the flow (no cell trapped). Flow distributes almost equally among all the 17 clusters……...46

Figure 3.6: Biochip trapping efficiency and WBC escape % versus pressure. Each data point represents result from a single WBC trapping experiment using a new biochip for every experiment. Four devices were used for each pressure value. For all these experiments, the number of input cells was in the range 180-500. Maximum trapping efficiency was obtained for 3 psi pressure. Snapshot depicts the fluorescently tagged white blood cells trapped in the microholes.…….....48

Figure 3.7: (A) Biochip trapping efficiency versus number of input WBCs. (B) WBC escape % versus number of WBCs entering the cell trapping region (i.e. total number of input WBCs – number of WBCs stuck in the inlet region). Each data point represents result from a single WBC trapping experiment using a new biochip for every experiment. For all these experiments, 3 psi pressure was used. The trapping efficiency has an 8% range (max value – min value). Maximum escape % value of 3.65 was obtained from these experiments……50

Figure 4.1: (A) A picture of a 9x11 PDMS-based, planar microlens array. The right inlet is used to fill up the microfluidic network with the UV curable polymer (the left inlet is not used in the depicted design). Scale bar, 1.5 mm. (B) A close-up view of 16 cured microlenses of different diameters. Each microlens sits beneath a square microwell. Scale bar, 200 μm. A magnified top view of a 60 μm in diameter microlens cured at 30 psi and a schematic diagram of its cross section are shown on the right (I and II respectively). Scale bar, 50 μm…….…….....58

Figure 4.2: The microfabrication process of the microlens device.……60

Figure 4.3: Schematic of the experimental setup for characterizing the optical propereties (effective focal length (EFL), point spread function (PSF)) of the microlens device. A laser (532 nm) was used to obtain the EFL while a white light source was used to obtain the PSF.……..62

Figure 4.4: Effective Focal Length (EFL) versus curing pressure for (A) 40 μm and (B) 60 μm diameter microlenses. Experimental and opto-mechanically simulated EFL values are obtained for a pressure range of 7.5-30 psi. Each data point is the average of 16 measurements from 2 microlens devices (8 microlenses/device). The measured EFL values have standard deviation of 4.31% and 4.10% for 40 μm and 60 μm diameter microlenses respectively.……...64

Figure 4.5: Numerical Aperture (NA) versus curing pressure for (A) 40 μm and (B) 60 μm diameter microlenses. NA values are calculated using the EFL values presented in Figure 4.4. 60 μm diameter microlenses (with lower EFL) have higher NA than 40 μm diameter microlenses (with higher EFL)...……..…….....66

Figure 4.6: (A) Surface profile of a 60 μm diameter microlens (cured at 30 psi) obtained using a white light interferometer. (B) A 2D microlens profile measured along its midline (cross section A-A' in A). The profile has been curve fitted with a sixth order polynomial…..……68

Figure 4.7: (A) Relative intensity (maximum intensity for a given axial plane normalized with the maximum intensity measured at the best focused plane) along the optical axis of a 60 μm diameter microlens as a function of the distance from the best-focused plane. The pictures depict the focused laser beam as imaged at the focal plane and at two out-of focus planes. Scale bar, 10 μm. (B) The PSF of the same microlens represented as the in-plane intensity distribution ($I[x,y] - I_0$) at the best-focused plane, normalized with respect to the background intensity I_0...……..70

Figure 4.8: Micron-size resolution patterns imaged: (A) without using a microlens, and (B) through a 60 μm diameter microlens (NA ~ 0.3). Equally-spaced, 3 μm wide lines are magnified by a factor of ~2 and are clearly visible. Scale bar, 50 μm (A) and 25 μm (B)…….……71

Figure 5.1: (A) A 10x10 array of 56 μm in diameter doublet microlenses. Scale bar, 500 μm. (B) A schematic of the cross section of the microlenses array. The microlens diameter is defined by the diameter of the microhole. (C) A collimated light beam is focused at a point (focal point) right below the top surface of the PDMS layer. The distance between the focal point and the silicon dioxide surface is the microlens effective focal length (EFL). *a* is the microhole (microlens) diameter and *r* is the microsphere diameter. (D) Mechanism of image formation using the doublet microlens array. The object is placed on the surface of the microlens. A magnified image is formed directly on a CCD sensor……...78

Figure 5.2: Microfabrication process of the doublet microlens array. Key concept is the fluidic assembly of glass microspheres (step 4)……...80

Figure 5.3: Simulation results depicting the dependence of the numerical aperture (NA) on the microhole to microsphere diameter ratio (*a/r*). A NA value of 0.495 was estimated for our microfabricated microlenses…….82

Figure 5.4: Normalized intensity (with respect to the background corrected average intensity at the best focused plane) of a doublet microlens as a function of the axial distance from the best focused plane. The images depict a focused light beam at different axial planes. Scale bar, 10μm…..……84

Figure 5.5: (A) PSF of a 4x4 microlens array. Scale bar of the image: 100 μm. (B) PSF of an individual microlens. Scale bar of the image: 10 μm. (A) and (B) plots were obtained using a 4X (NA=0.15) and a 40X (NA=0.6) microscope objective respectively. In both (A) and (B), normalized

intensity values at a particular xy point were obtained by normalizing the background-corrected light intensity at that point with the maximum value in the entire image……..……85

Figure 5.6: (A) Schematic of the setup for imaging micron-size resolution patterns using the doublet microlenses array. (B) (I) & (II) Brightfield, transmission images of 1 and 2 μm line resolution patterns respectively using a 56 μm diameter microlens (NA~0.495). Equally spaced, 1 μm wide lines are clearly resolved by the doublet microlens. Scale bar, 20 μm. (III) Brightfield, transmission image of a 5 μm square grid. Scale bar, 20 μm. (IV) Fluorescence image of a polystyrene bead (4 μm in diameter)……...…….88

Figure 6.1: Snapshot of the first prototype of a cell trapping biochip with an integrated volume metering chamber. The metering chamber of this prototype has a total volume of 0.1 μl. Scale bar, 500 μm……..95

Figure 6.2: Cross sectional view of the proposed oil-immersion microlens array. A glass coverslip and a spacer will accurately define the distance between the lens and the sample object.……..97

Figure 6.3: Schematic of the proposed benchtop WBC counting system. The integrated biochip (cell trapping module + microlens array) will constitute the disposable part of the system. The benchtop reading equipment will comprise of the optical components like the laser diode, cylindrical lens, achromatic doublet lens, bandpass filter and CCD sensor. ……...98

List Of Appendices

Appendix A Fabrication Process Flow Of The Microfluidic Devices……...101

Appendix B Opto-mechanical Simulations Of Planar Microlens' Focal Length And Numerical Aperture……..113

ABSTRACT

White blood cells (WBCs) and their subtypes are important constituents of the human immune system as their concentration, quantified by a WBC count test, indicates the state of body's immune response against infections. These cell count tests are important prognostic and diagnostic indicators for a number of human immunological diseases, most prominent of them being AIDS. Flow cytometry (FC) is the gold standard for counting WBCs. Although high throughput and accurate, FC based instruments are bulky, expensive and require skillful and trained personnel for their operation and maintenance. This necessitates the development of inexpensive, portable point-of-care (POC) systems for capturing and enumerating WBCs and their subtypes.

We envision a portable, point-of-care WBC counting system which can capture thousands of WBCs and simultaneously image and count them. Towards this end, we have developed:

- A microfluidic biochip for trapping and counting WBCs. The biochip has a novel 3D cell trapping architecture and enables simultaneous capture and counting of thousands of WBCs. A WBC trapping efficiency of ~90% is achieved using the biochip.

- Microlens arrays with a large field of view (FOV) imaging capability that have an optical performance (numerical aperture, resolution) equivalent to a conventional microscope objective.

We envision that the cell trapping biochip and the microlens arrays proposed in this thesis can be integrated to perform simultaneous on-chip capture and imaging/counting of WBCs. The integrated microsystem can also be used as a generic platform for sorting and enumeration of different kinds of cells for disease diagnosis and research applications.

CHAPTER 1

INTRODUCTION

1.1 Motivation

Globalization and rapid industrial growth has led to significant improvement in the average standard of living of the people worldwide. This economic prosperity has spurred increased health awareness amongst the people from developed and developing countries. These people now subscribe to regular health checkup programs at their nearby hospitals and health clinics to keep a periodic record of their health and to prognose a disease or a disorder in its early state. However, lack of time due to busy work schedule and hectic urban life makes it difficult to make these regular hospital visits. Thus there is a huge demand to develop benchtop biomedical systems which are affordable and portable enough to be installed in one's house and which have diagnostic and monitoring performance comparable to the state-of-the-art equipments in the hospitals and health clinics.

On the other end of the health management spectrum are the underdeveloped regions of the world like the ones in sub-Saharan Africa and South Asia where there is an immense shortage of basic infrastructure like water, electricity and sanitation and hence are termed as "resource limited settings". Ironically, these regions have one of the world's highest densities of population and are the ones most severely hit by

the life threatening epidemics and diseases like Acquired Immune Deficiency Syndrome (AIDS), malaria and tuberculosis [1-3]. Illiteracy and lack of health and sanitation awareness leads to these diseases outbreak and consequently these people need to undergo diagnosis and monitoring tests at regular intervals to prevent a huge loss of human life. Extreme poverty and scarcity of basic infrastructure deprives these teeming millions of access to even primary healthcare facilities. With the intervention of global health agencies like the World Health Organization and non-governmental agencies like the Bill and Melinda Gates Foundation and several others, the hospitals and health clinics in these regions are equipped with state-of-the-art disease diagnostic and treatment systems [4-7]. However, a major proportion of the population in these regions resides in rural areas far from the urban health centers and hence, is unable to avail the benefits of these facilities. Consequently there is a major research emphasis on developing inexpensive healthcare devices and systems which can be used at the point-of-care (POC) in these resource-limited settings with a performance equivalent to the state-of-the-art systems and with minimal resource requirements [8, 9].

Interestingly, the two different demographics described above with totally different economic and social frameworks have an identical requirement of POC diagnostic and monitoring systems for an efficient health and disease management. Rapid technology strides in the past few decades have made it possible to design and develop systems to meet this huge need for POC biomedical devices. Development of these devices has primarily entailed the miniaturization of macroscale equipments and processes in a compact design with low sample requirements, using minimal

infrastructure like electricity, water and refrigeration and operable without the help of a trained health personnel. Design of these POC systems involves the identification and development of:

- A mechanism to manipulate the biological sample (blood, saliva, urine etc.) in order to isolate and capture the desired disease biomarker.
- A mechanism for making a quantitative/qualitative measure of the biomarker to ascertain the disease occurrence/stage.

In this thesis, we will discuss POC systems for the analysis of blood and its components which enable diagnosis and monitoring of a large number of diseases.

1.2 Blood: a major disease biomarker

Blood is one of the most common biological samples whose constituents are used for diagnosis and staging of a large number of diseases. Blood consists of three kinds of cells; red blood cells (RBCs), white blood cells (WBCs) and platelets contained in a fluid known as plasma (**Figure 1.1**) [10]. Blood is primarily composed of:

- Plasma which makes more than half the volume of the blood (~55%) and consists of about 92% of water and a number of other proteins, ions and hormones.
- RBCs also known as erythrocytes constitute 99% of all the blood cells and are responsible for delivery of oxygen to different parts of the body. These cells are doughnut shaped with a disk diameter of 6-8 μm and a thickness of 2 μm.

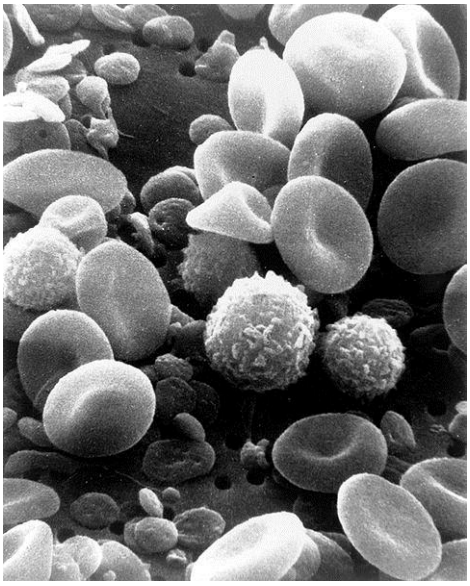

Figure 1.1: A scanning electron microscope image of blood cells [adapted from the wikipedia website: http://en.wikipedia.org/wiki/White_blood_cell]. The doughnut shaped cells are the RBCs, the spherical shaped cells are the WBCs and the small disc-shaped cells are the platelets.

- WBCs also known as leukocytes are divided into 6 subcategories: neutrophils, basophils, eosinophils, lymphocytes, monocytes and macrophages. WBCs are normally spherical in shape with their size ranging from 7 to 20 μm in diameter. These cells play an important role in defending the body against infections and hence constitute an important part of the body's immune system. The total count of WBCs and the differential count of their subtypes is therefore an important indicator for a number of immunological diseases.
- Platelets also known as thrombocytes are irregularly shaped blood cells which are 2-3 μm in diameter and play an important role in clotting of blood at the site of a cut or an injury.

In particular, WBCs or their subtypes constitute different aspects of human immune system and an increase or decrease in their count from the normal level usually indicates an immunological disorder [11]. WBCs and their subtype count is therefore an important measure for diagnosis and monitoring of immunological diseases like AIDS as well as other diseases like leukemia [12]. Patients afflicted with these diseases need to undergo WBC count tests (total as well as differential) at regular intervals (few days to months) to ascertain the efficacy and to accordingly modify the treatment regimen to check the proliferation of the disease. To summarize, WBC and their subtypes count tests constitute probably the most important tests for ascertaining the functioning of human immune system and hence are required to be conducted at frequent intervals to diagnose and stage an immunological disorder. It cannot be emphasized enough that a WBC and their subtypes counting system which can be used at the point-of-care (POC) will enable a more efficient disease management particularly in resource limited settings. Next, we review the current state-of-the-art techniques used for counting WBCs and their subtypes from human blood.

1.2.1 Flow cytometry for counting WBCs and their subtypes

Current techniques for counting WBCs and their subtypes are based on flow cytometry (FC) which is considered the gold standard for quantifying WBCs with a relatively small margin of error [13]. The operation principle of FC involves the hydro-dynamic focusing of cells which are registered to a counter while passing one by one through the focal point of a laser/detector setup. The interaction of the edge of cell with the laser light leads to forward light scatter whose magnitude indicates cell size. Light

photons interacting with the internal contents of a cell scatters at a wide angle and this side scatter provides information about the internal compostion (e.g. granularity) of a cell. A specialized type of flow cytometry, known as fluorescence activated cell sorting (FACS) is the most widely used method for counting individual cells (**Figure 1.2**) [14]. In this approach, the cells are labeled with a fluorescent dye which specifically tags the cells of interest. This dye gets excited by light in a certain wavelength range and emits light in another wavelength range. If a cell emits light upon passing through the focused laser beam (recorded by the detector), it is included in the total cell count.

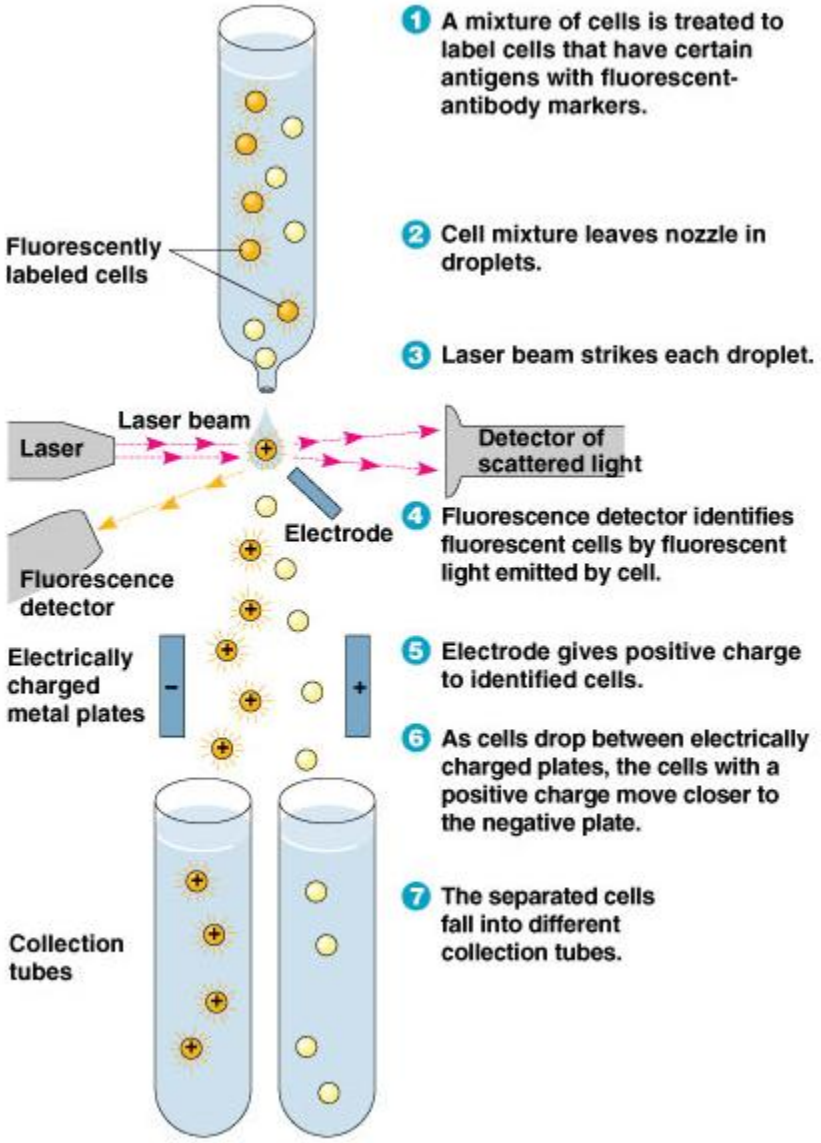

Figure 1.2: Mechanism by which Fluorescence activated cell sorter (FACS) counts and sorts cells [adapted from http://classes.midlandstech.com, Copyright 2004 Pearson Education, Inc.].

The state-of-the-art FC instrumentation consists of commercial available multi-purpose FACS cytometers or specialized single platform flow cytometers designed for counting WBCs. These instruments are expensive ($30,000-$150,000) and not realistic options for most POC settings as they are bulky, have continuous electricity requirements, require the use of filtered water and expensive refrigerated reagents, and

require technical expertise for operation (**Figure 1.3**). Single-purpose FC designs have constraints similar to standard flow cytometry: costs, electricity dependence, and operational inefficiencies. For all of these reasons, the use of FC systems has been mostly limited to hospitals and specialized clinics in big cities; they are almost unaffordable for the small health centers and inaccessible to the people in the resource limited settings. These limitations of the FC systems bring forward a pressing need to develop inexpensive, portable systems which can be used at the POC for isolating and counting WBCs from human blood.

Figure 1.3: Image of a two-laser FACS Calibur Flow Cytometer [adapted from http://www.georgiahealth.edu/cancer/shared/flow/equipment.html]. The flow cytometer is expensive, bulky, needs electricity and refrigerated reagents and a trained personnel for its operation and maintenance.

1.3 Thesis Objective

As discussed earlier, requirements of large volumes of samples and expensive reagents (in the order of ml), complicated and costly optical components and technical

personnel makes FC instruments unsuitable for the resource limited settings. Hence there is a pressing need to develop inexpensive portable WBC counting systems which can be used at the point of care in resource limited settings. We envision a WBC counting system similar in operation to a glucose level monitoring instrument (known as a glucometer) used by diabetic patients (**Figure 1.4**). In order to obtain the count of WBCs or their subtypes, an undiluted blood sample will be drawn from the patient using the standard finger-prick method and loaded by the user into a disposable biochip that will process the blood sample. The biochip will be inserted into the analysis module which will provide the WBC count in less than a minute. This system will enable to perform WBC count test for a few dollars and its portability and ease-of-use will make it suitable for the resource limited settings.

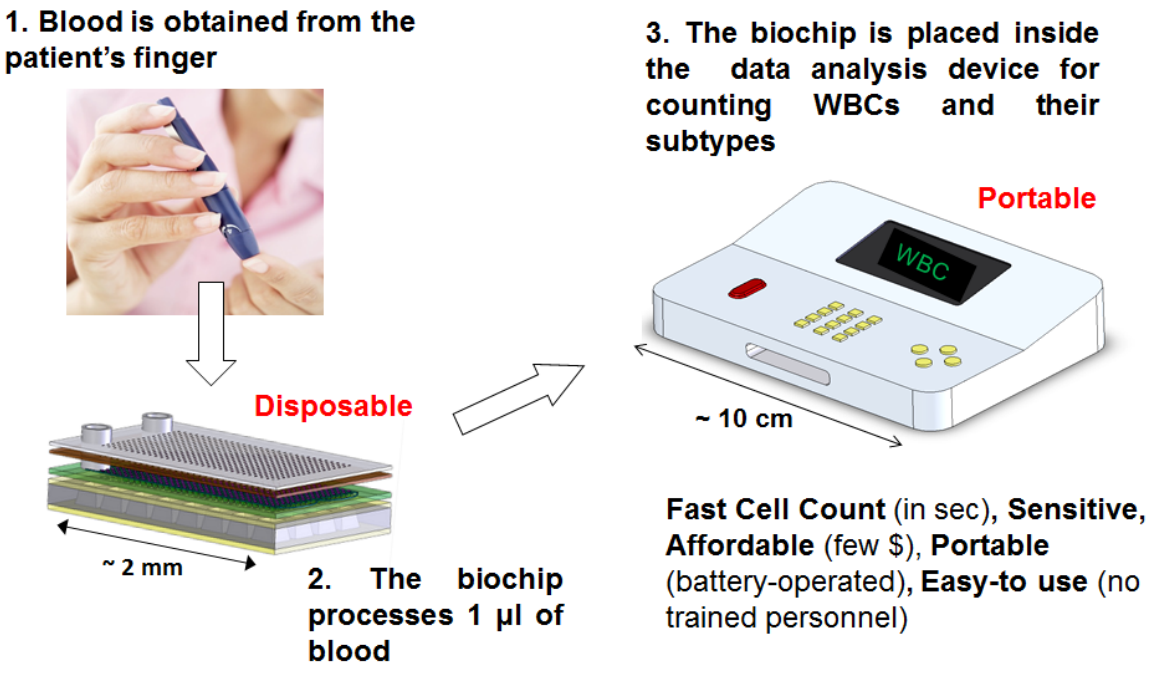

Figure 1.4: Portable system for obtaining counts of WBCs and their subtypes at the point of care.

In order to develop a compact WBC counting system, we envision a disposable biochip that can: a) capture WBCs from human blood and b) independently image and count the captured cells. The proposed biochip will be formed by integration of the microfluidic and microoptical devices respectively (**Figure 1.5**). The microfluidic component of the device will enable the capture of thousands of WBCs on the biochip surface and the microoptical component comprising of an array of microlenses will enable to image and count these cells. The incorporation of microoptical components on chip will preclude the need to use the conventional, bulky microscope elements resulting into a compact and cheaper WBC counting system.

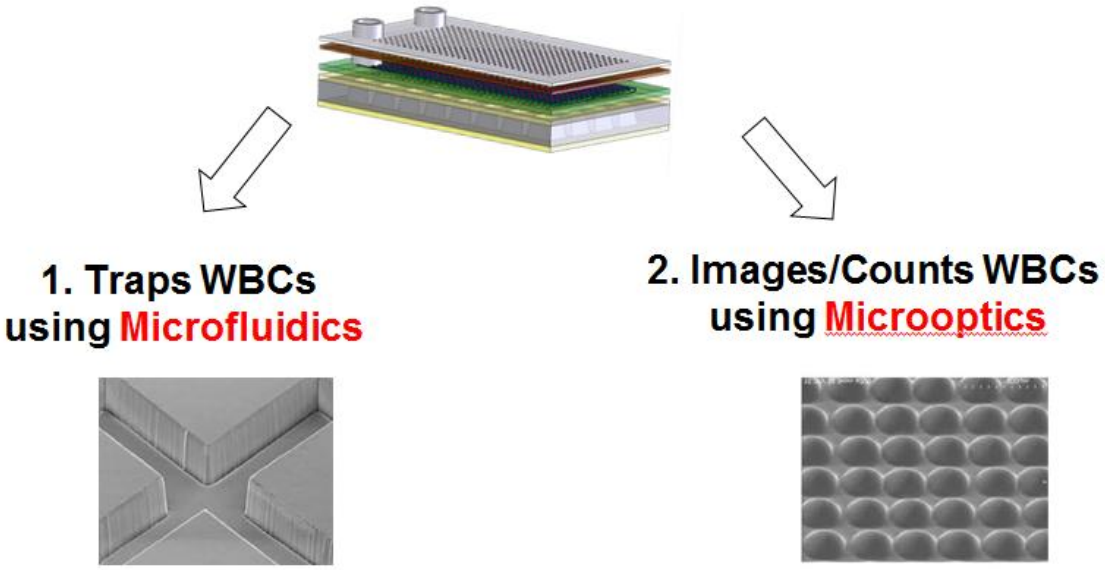

Figure 1.5: Disposable WBC capturing biochip obtained by the integration of microfluidic (cell capturing) and microoptics (cell imaging) components.

The biochip's cell trapping and imaging components have been presented in a cross sectional view (**Figure 1.6**). The first (microfluidic) module of the biochip is responsible for the capture of WBCs from the blood sample and the optical excitation of fluorescent molecules attached to the cell surfaces. The second (microoptics) module of

the biochip is responsible for collecting the light emitted by the captured WBCs and forming their image on an imaging sensor. The data analysis module would analyze this image and the number of captured WBCs will be obtained.

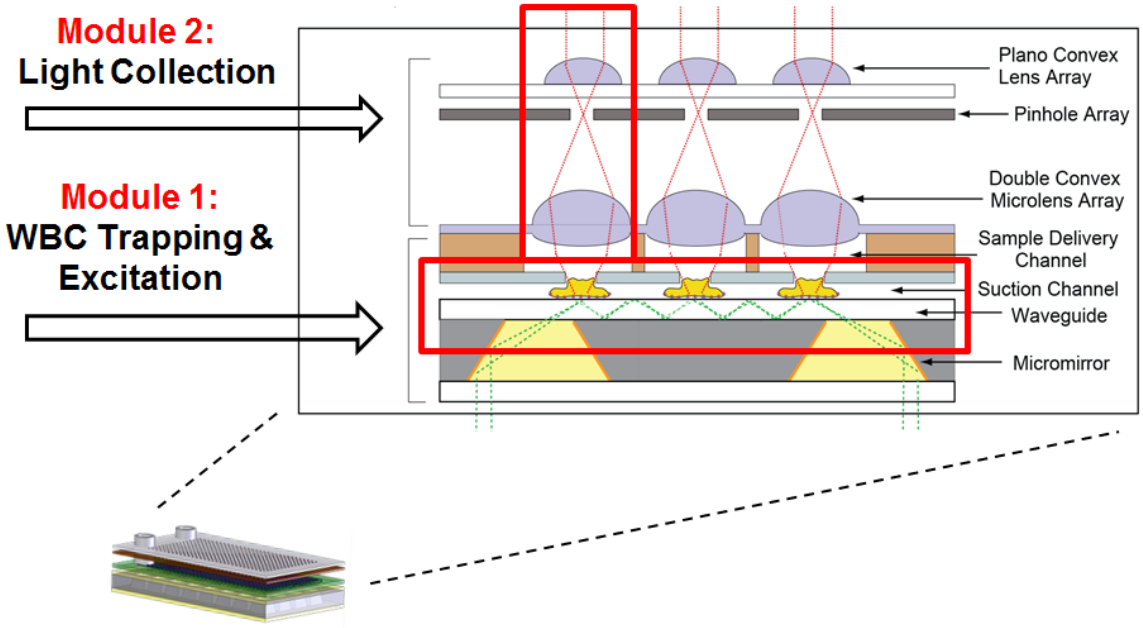

Figure 1.6: Cross-sectional schematic of the WBC counting biochip.

The biochip would be simple to operate, inexpensive to fabricate and will have low sample and reagent requirements (in the order of µl). In this thesis, we employ lab-on-chip technology for developing microfluidic and microoptical modules to fabricate the proposed WBC counting biochip.

1.3.1 Microfluidics for lab-on-a-chip systems

Microfluidics is a relatively recent branch of science and engineering which deals with the control and manipulation of fluids in flow channels with sub-mm dimensions [15]. Typically, such flow channels have at least one dimension (mostly the height) in the order of a few to a hundred microns. Microfluidics has favored greatly from the

advancements in the planar microfabrication technologies used for producing integrated semiconductor devices and microelectomechanical systems (MEMS) based sensors and actuators [16]. Over the past two decades, there have been pioneering developments in the field of microfluidics which enabled the integration of flow control modules like pumps, valves, mixers etc. on the microfluidic devices, hence making these systems compact and inexpensive by eliminating the need for external equipment to perform these functions [17].

Lab-on-a-chip devices refer to a class of devices which enable performing a set of laboratory operations (chemical and biological) on a small scale [18]. These devices are compact, easy to use, have lesser sample and reagent consumption as well as a smaller process time, enable precise control of the biological and/or chemical interactions and are very cost effective. Microfluidic devices possess all the characteristics mentioned above and hence the development of lab-on-a-chip systems has been concurrent with the advancement in microfluidic technology. Microfluidic systems have emerged with wide range of applications like individual molecule investigation [19], optofluidic systems integrating microfluidics with optics [20], chemical reaction on chips [21], cell manipulation on chips [22] and point-of-care diagnostic systems [23].

1.3.2 Research goals

With the characteristics mentioned above, lab-on-a-chip technology presents itself as a promising alternative for the miniaturization of conventional state-of-the-art flow cytometers. These microdevices will meet the demand for point-of-care disease

diagnostic and monitoring systems. Using microfluidic technology as the enabling tool, this thesis aims towards developing components for the point-of-care WBC capture and counting biochip. The thesis aims at achieving the following objectives:

1. *To develop a cell trapping microfluidic biochip for capturing and counting white blood cells from human blood.*

Since the white blood cells constitute a very small fraction of total cellular composition of the blood, separation of WBCs from the other cells (RBCs and platelets) is the first step in the process to count the WBCs and their subtypes. The conventional flow cytometry systems used for counting WBCs employ a serial process in which the fluorescently marked WBCs (in a human whole blood sample) are passed in a focused stream through a detection region and are counted and separated based on their light scattering characteristics. Miniaturizing these systems into portable setups however, entails expensive optical components (lasers, detectors etc) which need to be precisely aligned to perform a serial counting of the WBCs. Here, we aim to develop a microfluidic cell trapping biochip which will perform a size based separation of the WBCs from human whole blood. This approach will entail a parallel cell counting process in which thousands of WBCs will be simultaneously captured on the surface of the biochip and counted. This biochip should be simple to use, perform an efficient capture of the WBCs, integrable with other optical components and provide a generic platform for size based capture and counting of cell types other than blood cells for diagnosis and monitoring of several other diseases.

2. To develop a micro-optical module for simultaneously imaging a large number of cells.

Optical imaging is the most commonly used technique for analysis of biological samples (cells, tissues etc). A conventional microscopy setup uses a high magnification objective lens with a high light collection capability (indicated by its numerical aperture NA) to obtain a high-resolution image of the micron-sized cells. However these objective lenses are not only expensive, they also have a small field of view (FOV) (a 20x magnification objective has a FOV of ~ 1mm), which prevents them from simultaneously imaging cells spread over a larger area. Since our aim is to develop a system that can simultaneously count thousands of WBCs captured on the biochip surface (Aim 1), we work towards development of optical systems that can provide a high FOV imaging capability while retaining the optical performance (resolution, magnification etc) of the microscope objective lenses. Here, we aim to develop two types of inexpensive microlens arrays which enable simultaneous counting of a large number of microobjects spread over a large field of view (in the order of cm). The first types of microlenses are polymer-based microlenses that can be fabricated easily and reproducibly from a patterned mold and have an equivalent optical performance as the microscope objective typically used for imaging cells and tissues. The second type of microlenses are doublet microlenses which have a higher light collecting performance (NA) than the planar microlenses and are capable of forming brightfield as well as fluorescent images of biological microobjects directly on an imaging sensor surface. These microlens arrays can be integrated with the cell trapping biochip described above and could possibly enable

development of inexpensive systems for on-chip counting of cells, precluding the need for bulky external microscopes.

1.4 Thesis Organization

The research work presented in this thesis has been organized in the form of the following five chapters:

Chapter 2 – Literature Review

This chapter reviews the microfluidic lab-on-chip devices for capturing and counting white blood cells (WBCs) and their subtypes. A review of various microlens arrays with an emphasis on their microfabrication processes and optical performance has also been discussed in this chapter.

Chapter 3 – A 3D Microfluidic Cell Trapping Biochip For Counting White Blood Cells

This chapter presents a novel 3D cell trapping biochip which enables size based confinement and capture of WBCs. The biochip is a significant improvement over the membrane based captures approaches in that it confines WBCs in the 3 dimensions resulting into higher WBC trapping efficiency. The design of the biochip has been optimized to ensure equal WBC trapping in all regions of the biochip without any dependence upon the relative distance from the biochip inlet or outlet. A high (>87%) WBC trapping efficiency has been demonstrated using the biochip.

Chapter 4 – A Polymer-based, Planar Microlens Array For Imaging Micron-Sized Objects

This chapter presents a soft lithography based approach to fabricate an array of planar, polymer-based microlenses. UV-assisted curing of a pressurized polymer under deformable, elastomeric membranes is utilized to obtain fixed focal length microlenses. Sub-100 μm diameter microlenses with numerical aperture (NA) in the range 0.05-0.30 have been fabricated using this approach. We utilized the microlenses to image the micron-size resolution features patterned on a chrome mask.

Chapter 5 – A High Numerical Aperture Doublet Microlens Array

This chapter demonstrates a novel doublet microlens array fabrication technique. The doublet microlenses are formed using glass microspheres assembled on silicon microholes and planarized using a polymer layer. The fabrication process was combination of silicon microfabrication and a novel fluidic assembly technique. The fabricated microlenses had a numerical aperture of 0.5 which was a significant improvement over the NA (0.3) of microlenses reported in Chapter 4. These microlenses could also perform brightfield as well as fluorescent image formation of micron-size objects directly on an imaging sensor without the use of intermediate lenses.

Chapter 6 – Conclusions and Future work

This chapter summarizes the work demonstrated in this thesis and presents the potential future directions.

CHAPTER 2

Literature Review

This chapter presents a review of the microfluidic biochips that have been designed for capturing and counting white blood cells (WBCs) from human blood. A review of various microlens arrays, which can be utilized for on-chip optical imaging of microobjects, has also been presented in this chapter.

2.1 Introduction

Microfluidic lab-on-chip technology has found extensive applications in the global healthcare sector for the past two decades [23, 24]. With their advantages of low sample requirements and reagent consumption, inexpensiveness and ease of operation, these devices have emerged as viable replacements to the macroscale flow cytometry (FC) techniques particularly for the point-of-care (POC) diagnostic applications. Since WBC count is an important biomarker for the diagnosis and monitoring of a number of immunological diseases and disorders, significant research emphasis has been given towards the development of microfluidic devices for WBC capture and counting. The WBC capture microdevices employ various principles like size based capture, immunoaffinity based capture etc. In the first section of this chapter, various microfluidic approaches for WBC capture from human blood are discussed.

Since this thesis also presents microlens arrays for high-resolution optical imaging of micron-sized objects, we review the fabrication and optical performance of various microlens arrays.

2.2 Microfluidic biochips for WBC capture and enumeration

WBCs and their subtypes count is an important diagnostic and monitoring indicator for a number of immunological diseases (e.g. AIDS). For most of these diseases, a specific WBC subtype count is required to make a disease assessment (e.g. CD4+ T-lymphocyte count to monitor HIV/AIDS proliferation). A strategy to count these WBC subtypes can entail capture of all the WBCs and then identifying and counting the targeted WBC subtype by performing an additional step. A large number of microfluidic biochips have been proposed for separation and capture of WBCs (and their subtypes) from human blood [25]. Since one of the aims of this thesis is to develop a WBC capturing microdevice, we are going to review these microfluidic approached to capture WBCs. Even though some of these microdevices were designed to capture a specific WBC subtype (rather than all the WBCs), their operating principle can be used for capturing all the WBCs.

2.2.1 Size-based capture of WBCs

Since WBCs are bigger in size than other blood cells (RBCs and platelets), they can be separated from these cells by passing human blood through filter structures which allow RBCs, platelets and blood plasma to pass through while capturing larger WBCs. In one such approach, a commercial polycarbonate track-etch membrane filter (with ~ 3 μm

in diameter pores) is used to separate and capture WBCs from human whole blood (**Figure 2.1**) [26]. The smaller and less stiff RBCs and platelets squeeze through the holes while the larger WBCs are captured. This device was designed to count the CD4+ T-cells (a type of WBCs) for ascertaining the proliferation of HIV infection in infected patients. The T-cells were stained with fluorescent antibodies before the whole blood was injected into the device and the captured T-cells were enumerated with the help of epifluorescence microscopy. This is an extremely simple approach for WBC capture requiring no sample preparation and a process time of less than 10 minutes. However it can be seen that some of the membrane holes are fused leading to the escape of WBCs along with the RBCs and platelets and resulting into a low efficiency of capture of WBCs.

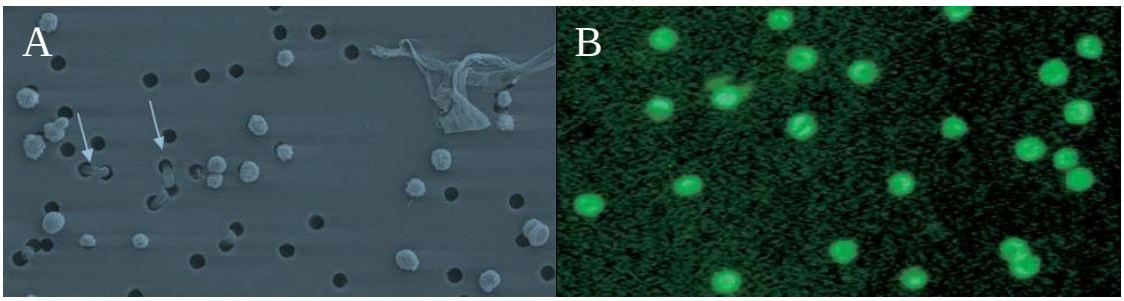

Figure 2.1: The membrane flow cell device for counting CD4+ T-lymphocytes from human blood [adapted from [26]]. **(A)** Upon processing the whole blood through the flow cell, the white blood cells are captured on the micro holes and the red blood cells and platelets filter through. The arrows indicate the red blood cells filtering through the microholes. **(B)** Fluorescence image showing T-lymphocytes (stained with fluorescent antibodies) captured on the membrane.

A WBC capture approach similar to that employed in the membrane filtration device used different patterns of microfilters etched on a silicon substrate (**Figure 2.2**) [27]. The various designs used were a) weir, b) pillar, c) crossflow and d) membrane. While the RBCs squeezed through the 3.5 μm filter patterns, the WBCs were captured. These devices demonstrated varying levels of WBC trapping and RBC passing

efficiencies. While the weir pattern device obtained a WBC trapping efficiency and RBC passing efficiency of 70% and 28-42% respectively, the crossflow device was the most efficient pattern with the WBC trapping efficiency and RBC passing efficiency of 72-95% and 60-95% respectively. Since the RBCs are almost two to three orders of magnitude more in number than the WBCs, even a small percentage (5%) of non-passing RBCs will clog the device. These filtration based WBC capture approaches suffer from the drawback that they trap WBCs in 2 dimensions and the cells being flexible, are free to squeeze out in the 3rd dimension resulting into a lower WBC trapping efficiency.

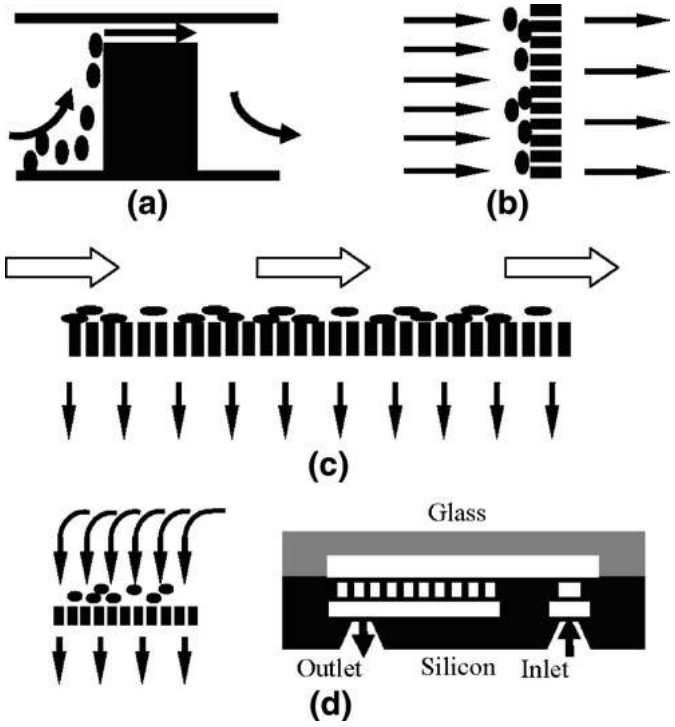

Figure 2.2: Schematic representation of the silicon microfilter designs used for WBC capture [adapted from [27]]. The designs are a) weir filter (side view), b) pillar filter (top view), c) crossflow filter (top view) and d) membrane filter (side view).

2.2.2 Immunoaffinity based capture of WBCs

Many human cells express unique receptors on their cell surface (antigens) which bind to specific proteins (known as antibodies extracted from blood serum of humans, mouse etc.). All WBC subtypes have a common cell surface receptor CD45, which can be used for isolating WBCs from other blood cells (RBCs and platelets) by using a monoclonal antibody against this receptor (anti-CD45 monoclonal antibody). Also different subtypes of WBCs possess a unique combination of different cell surface receptors like CD3, CD4, CD8, CD18 etc. By using antibodies specific to a particular receptor, it is possible to capture and separate a WBC subtype from other WBCs. Capturing WBCs by passing blood over a surface functionalized with antibodies is a very useful WBC isolation approach. This immunocapture approach becomes more powerful in a microfluidic device which with its high surface area to volume ratio enables greater cell-antibody interactions resulting into a higher WBC trapping efficiency.

Immunoaffinity based microfluidic devices have been used to capture WBCs from human blood using two different approaches. These approaches are: a) WBC adhesion on antibody functionalized structures (pillars) in a microfluidic device and b) Optimization of shear stress for WBC adhesion on antibody immobilized planar surfaces. The first approach mimics a physiological process in which the blood vessels express specific adhesion proteins on their surface to selectively capture WBCs, hence separating them from RBCs and platelets [28, 29]. In this phenomenon, the cells are not permanently immobilized on the binding site instead they roll on the surface. Microfluidic devices with different pillar geometries and configurations, functionalized

with a WBC specific adhesion protein (human E-selectin IgG) were used to capture different WBC cell lines and the influence of pillar geometry and configuration on the speed and efficiency of WBC capture was evaluated (**Figure 2.3**). Using this device, a hundred fold enrichment of the WBCs was obtained as compared to their original concentration. However, since these experiments were done with leukocyte cell lines rather than human blood sample, the capability of this approach to separate and capture WBCs from other blood cells in the sample is still unknown.

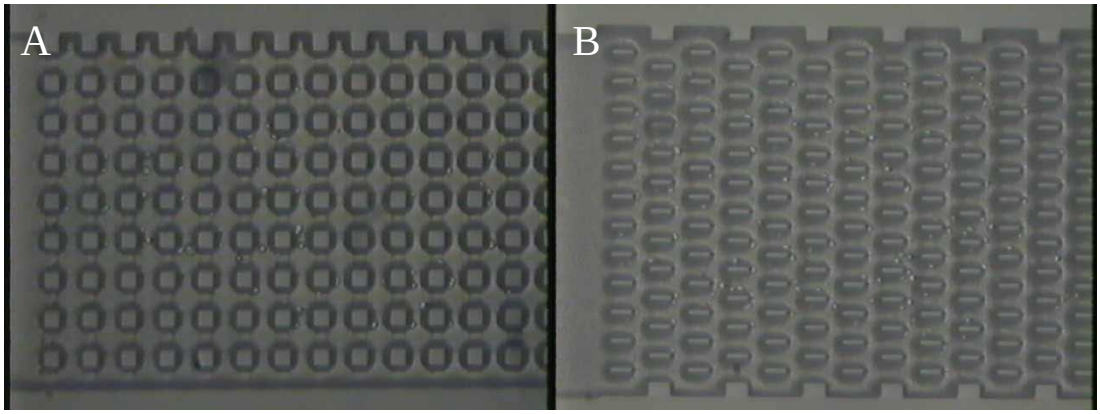

Figure 2.3: Microfluidic device with protein (E-selectin) functionalized pillars for capturing leukocyte cell lines [adapted from [28]]. **(A)** Square array of 25x25 μm square posts spaced 25 μm apart. **(B)** Alternating arrays of thin posts with 30 μm longitudinal post to post spacing and the adjacent rows offset by 15 μm in the flow direction.

The second immunoaffinity based capture approach relies upon the change in the cell-antibody adhesion mechanics with the shear stress in the flow. Different WBC subtypes have different optimal shear stress values for the most efficient capture. To ascertain the optimal shear stress for the adhesion of human lymphocytes, cells were flown in a device (with antibody functionalized surface) with linearly varying shear stress [30]. Once optimized, devices with parallel flow design (constant optimal shear stress throughout the device length) were used for enrichment of lymphocyte cell lines [31].

100% and 75% pure suspensions of T-lymphocytes and B-lymphocytes were obtained in ~ 3 min.

Using the above immunoaffinity based capture approach, a microfluidic device was fabricated for capturing and counting of CD4+ T-cells from 10 μl of HIV infected whole blood (**Figure 2.4**) [32]. A T-cell capture efficiency of 70-80% and a capture specificity of 60-90% were obtained using this device. A low value of capture specificity was attributed to the binding of monocytes on the antibody-immobilized surfaces.

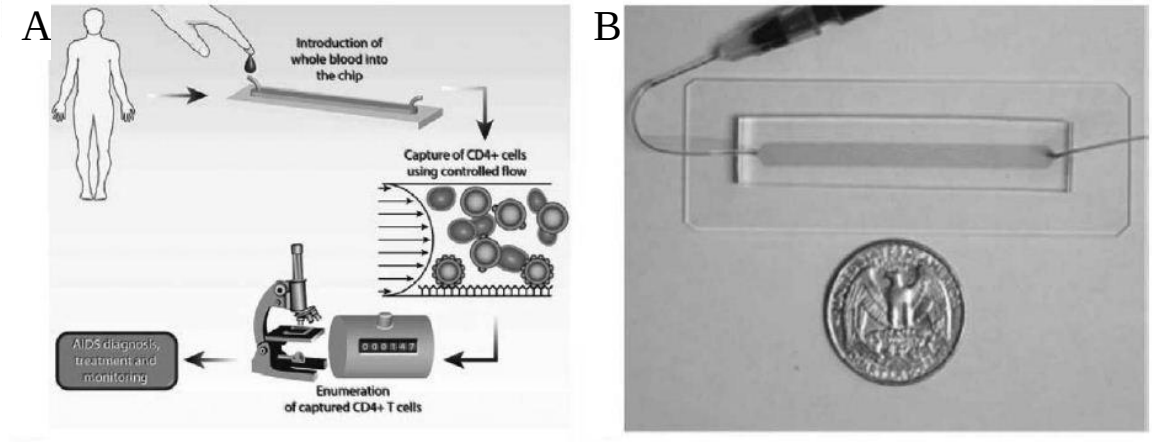

Figure 2.4: Microfluidic device used for capturing and counting CD4+ T-cells from human whole blood [adapted from [32]]. **(A**) Schematic of the steps of operation of the CD4+ T-cells counting microdevice. **(B)** Microfabricated device with optimal channel dimensions (4 mm x 51 mm x 50 μm for optimal shear stress) to capture T-lymphocytes.

A modified version of the above microfluidic device was designed to minimize the monocyte contamination to improve the CD4+ T-cell capture purity [33]. In this design, a monocyte depletion chamber was incorporated upstream of the CD4+ T-cell capture chamber (**Figure 2.5**). The monocytes with a higher optimal shear stress value (1.5 dyn/cm^2) were captured in the depletion chamber whereas the CD4+ T-cells with a lower optimal shear stress value (0.3 dyn/cm^2) were captured in the downstream

chamber. Using these devices, the T-cell capture purity increased to 80-90%. Although these devices were designed specifically for the capture of CD4+ T-cells, they can be functionalized with a suitable antibody to capture any leukocyte of interest. However, these devices have a drawback that their functionalization comprises of a number of steps and non specific binding of other blood cells significantly brings down the captured cell purity.

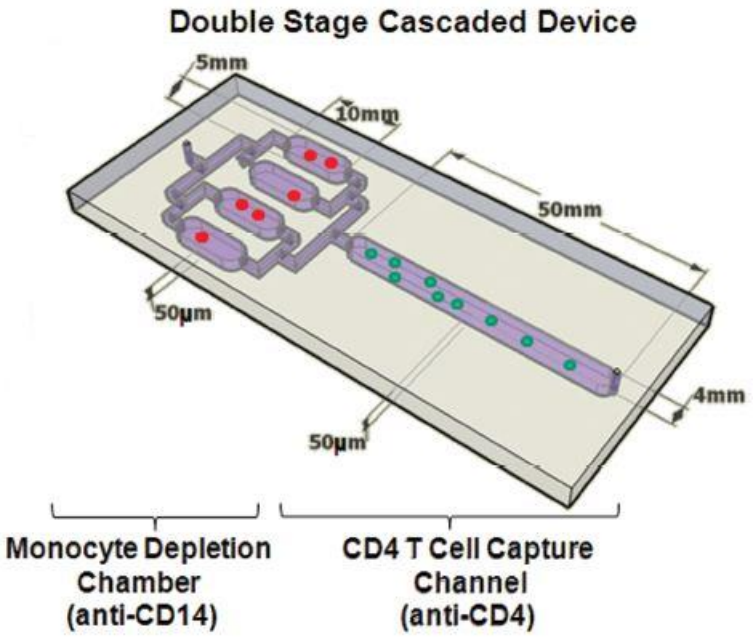

Figure 2.5: Schematic representation of a two stage cascaded device for CD4+ T-cell capture [adapted from [33]]. Reduced monocyte contamination results into an increased T-cell capture purity.

2.3 Microlens arrays for imaging micron-sized biological objects

Optical imaging based approaches have conventionally been used for detecting and visualizing micron-scale biological objects like cells and tissues. An optical microscope is the instrument most commonly used for cellular imaging. Various variants of the optical microscopy techniques like fluorescence microscopy, confocal microscopy

and multiphoton microscopy are used for cellular imaging depending upon the optical performance desired like the resolution, magnification, selectivity etc. These microscopes provide high resolution cellular imaging enabled by the high light collecting capability of their objective lenses (indicated by their numerical aperture NA). However, these high NA objective lenses have a small field of view (FOV) (in the order of 100-1000 μm) that prevents simultaneous imaging of cells and tissues spread over a larger area (in the order of mm). Also, the large size and huge cost of these objective lenses make them unsuitable for point-of-care imaging applications.

Advancements in the microfabrication technology over the past two decades has enabled researchers to develop micron scale lenses also known as ‘microlenses’ which aim to mimic the optical performance of conventional objective lenses. These microlenes are often obtained using a batch fabrication process from a photolithographically patterned mold. This enables simultaneous fabrication of thousands of microlenses reproducibly at a very low cost. Also, arrays of these microlenses enable simultaneous imaging of micro-objects spread over a large area, providing large FOV imaging capability. In the next section, we will review these microlens facbrication techniques with emphasis on the optical performance as well as the ease of fabrication of these microlenses.

2.3.1 Microlens fabrication methods

The microlenses can be divided broadly into two categories, i) fixed focal length microlenses and ii) variable focal length (tunable) microlenses. The tunable microlenses

primarily comprise of micro-optofluidic lenses that use a liquid as the lens medium and use a microfluidic scheme for actuating the fluid to vary the microlens focal length. Tuning using pneumatic pressure, dielectrophoresis, stimuli responsive hydrogels, electrowetting and hydrodynamic forces respectively are some of the actuation techniques used for varying the microlens focal length [34]. Although these techniques enable microlenses with focal lengths in a wide range, they require an external actuation source and hence they are not suitable for point of care applications with infrastructure constraints. Thus in this review, we will focus on the fabrication techniques for fixed focal length microlenses.

2.3.1.1 Fixed focal length microlenses

One of the earliest methods for fabrication of the fixed focal length microlenses involved melting and reflow of photoresist microstructures on a glass substrate. In order to obtain these microlenses, the photoresist microstructures were melted by heating them to a temperature of 150ºC. The surface tension caused the melted photoresist to obtain a curved microlens profile (**Figure 2.6A**) [35]. This fabrication approach provides high fill factor for the microlenses, with the microlens pitch (center-to-center distance) being as small as the microlens diameter (**Figure 2.6B**) [36]. The surface profile of these microlenses varies with the surface tension at the photoresist-air-glass interfaces.

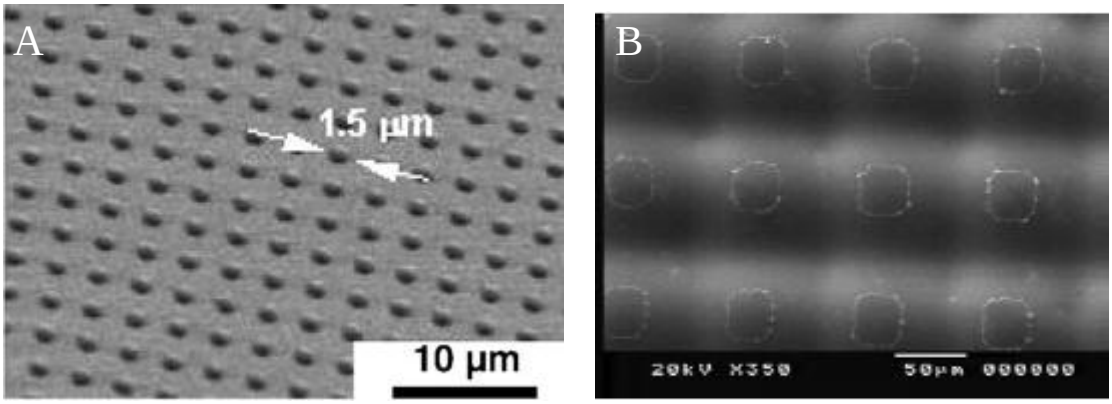

Figure 2.6: Scanning electron micrographs of the microlenses fabricated using photoresist melting and reflow methods. **(A)** 1.5 µm in diameter microlenses can be fabricated using this approach [adapted from [35]]. **(B)** High fill factor square microlens array fabricated using photoresist melt and reflow method [adapted from [36]].

Ink-jet printing of ultraviolet (UV) curable polymers has also been employed to obtain refractive microlenses. This process utilizes a drop-on-demand ink-jet printer to dispense the polymer on a hydrophobic substrate (**Figure 2.7A**) [37]. The polymer droplets are subsequently polymerized into plano-convex microlenses using UV light irradiation (**Figure 2.7B**) [38]. Like the photoresist reflow based fabrication approach, this process too enables fabrication of microlens arrays with a high fill factor. However this process requires the use of a very expensive setup for dispensing polymer on the substrate. Also the surface profile of the microlens depends greatly upon the surface tension at the interfaces as well as the wettability of the substrate.

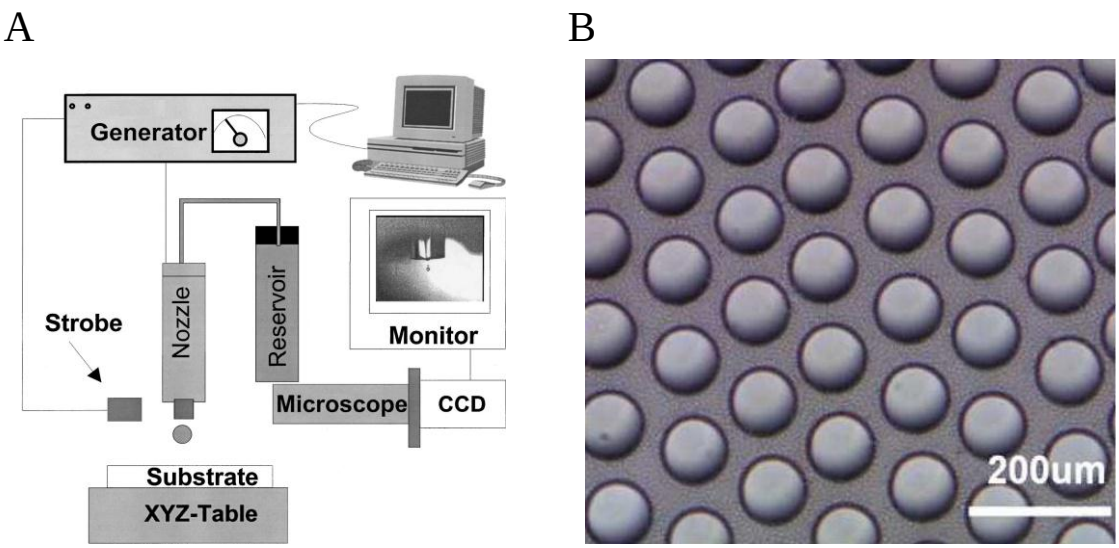

Figure 2.7: Ink-jet printing process for fabricating microlenses. **(A)** Schematic of the ink-jet printing setup for dispensing UV curable polymer [adapted from [37]]. (**B)** Microscopic image of an array of ink-jet printed microlenses [adapted from [38]].

Focused ion beam milling and femtosecond laser direct writing techniques have been proposed for fabrication of high NA microlenses [39, 40]. While the focused ion beam milled microlenses achieved NA of 0.64, microlens fabricated using femtosecond laser direct writing technique achieved high NA of 0.46 for a 100% fill factor (**Figure 2.8**). Like ink-jet printing technique, these processes are serial processes and require expensive equipments.

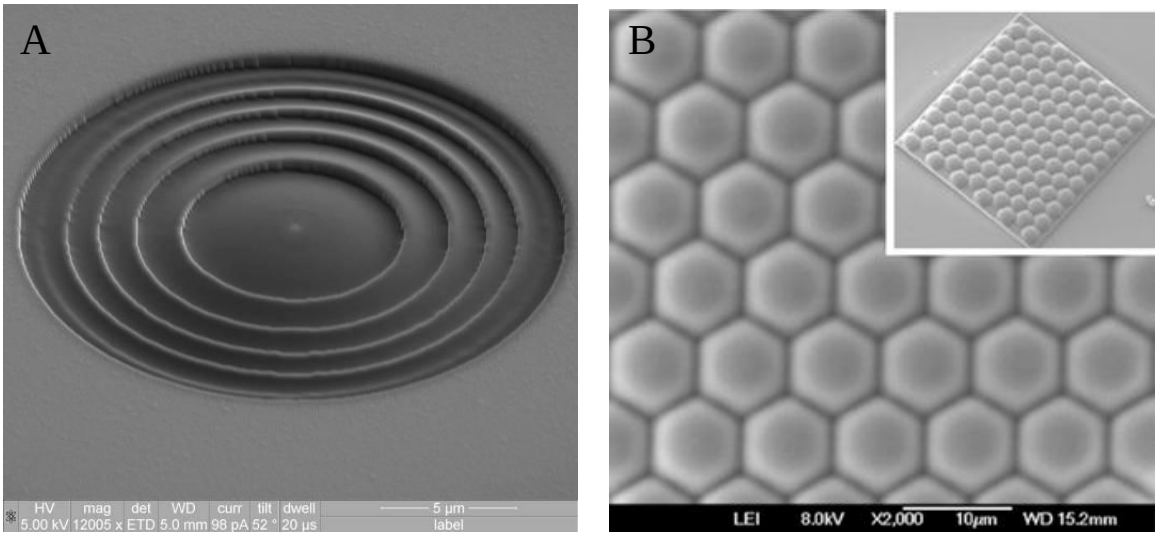

Figure 2.8: (A) Scanning electron microscope (SEM) image of the microlens fabricated using focused ion beam milling [adapted from [39]]. **(B)** SEM image of hexagonal microlens array fabricated using femtosecond laser direct writing. A 100% microlens fill factor is obtained using this technique [adapted from [40]].

A simple microlens fabrication approach involves molding various materials against rigid and elastomeric molds [41-44] (**Figure 2.9**). The patterns on a mold form the negative replica of the microlens profile resulting into microlenses when a thermally or UV curable polymer is cast on the mold. This microlens fabrication approach is a parallel approach which results into an array of 100s and 1000s of microlenses at the end of one molding step. This microlens fabrication process is simple to implement, however the quality of the mold deteriorates with its greater usage resulting into poor microlens surface profile.

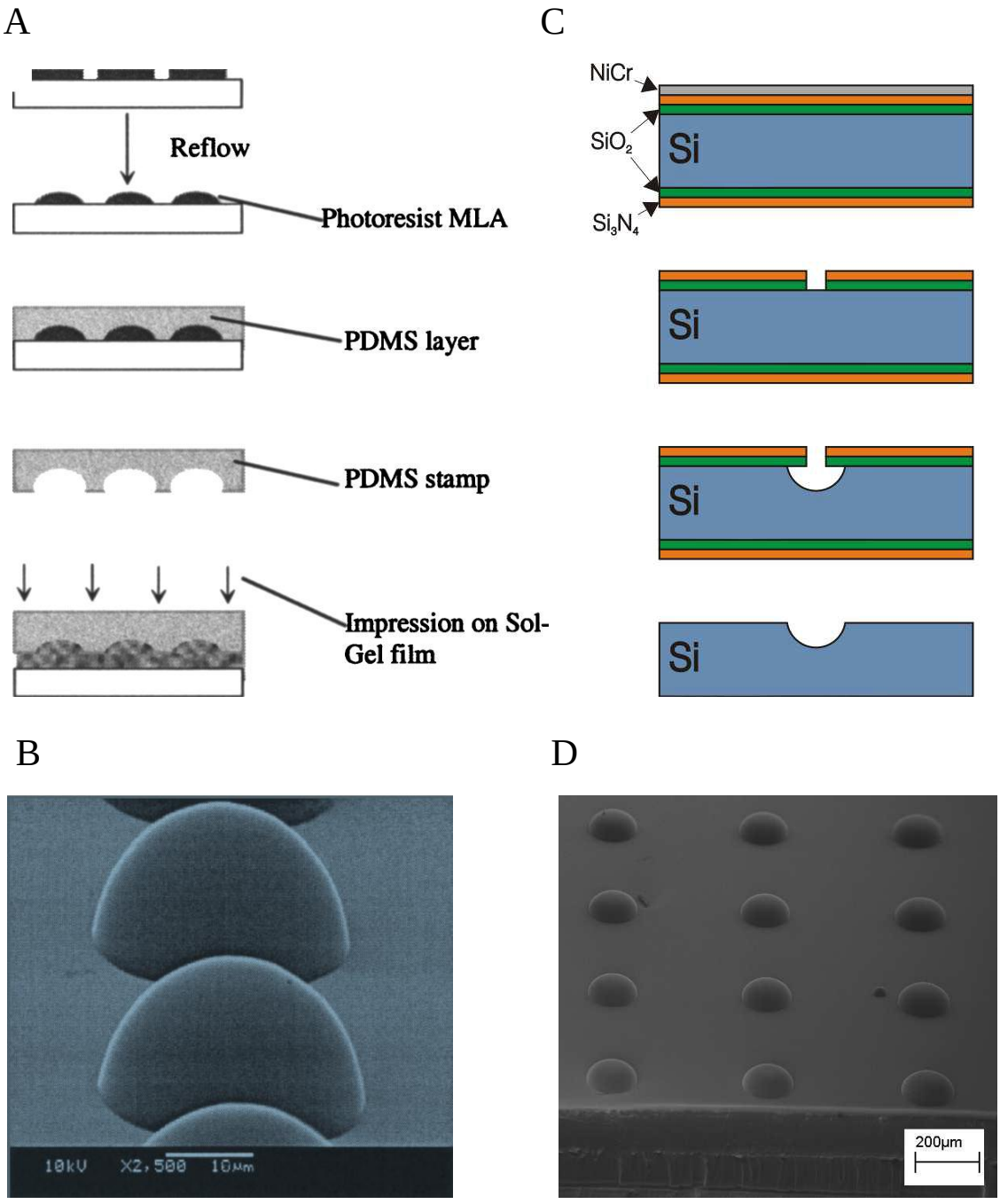

Figure 2.9: Microlens fabricated by molding various materials against the elastomer (polydimethylsiloxane PDMS) and silicon molds respectively. **(A)** Schematic of the fabrication of sol-gel glass microlens arrays by molding them against the PDMS mold [adapted from [42]]. (**B**) SEM image of sol-gel glass microlenses [adapted from [42]]. (**C)** Microlens mold obtained by the isotropic wet etching of silicon in an acid solution [adapted from [44]]. (**D**) SEM image of an array of microlenses obtained by molding a UV curable polymer against the isotropically etched silicon mold [adapted from [44]].

2.4 Conclusions

This chapter reviewed various microfluidic devices for separating and capturing WBCs and their subtypes. Various microfabrication techniques for obtaining high performance fixed focal length microlens arrays were also reviewed in this chapter. The advancements in the fields of microfabrication and microfluidics technology has led to the miniaturization of macroscale cell separation and imaging processes. An integration of these two technologies can enable the development of compact and cheap point-of-care WBC counting systems.

CHAPTER 3

A 3D Microfluidic Cell Trapping Biochip For Counting White Blood Cells

In this chapter, we present a microfluidic biochip for trapping and counting human white blood cells on a microfabricated hole array. A novel 3D cell trapping architecture has been proposed for performing size based capture of the white blood cells. White blood cells suspended in the buffer solution were injected under pressure into the biochip and optimal pressure for the highest cell trapping efficiency was ascertained. 3 psi was measured as the optimal injection pressure at which a high (>87%) efficiency of trapping of the white blood cells was achieved. We aim to develop this device as a point-of-care diagnostic and monitoring platform that can perform size based separation and counting of white blood cells and other disease indicators like the circulating tumor cells from human whole blood.

3.1 Introduction

White blood cells (WBCs) and their subtypes are important constituents of the human immune system [45]. Their concentration, quantified by a WBC count test, indicates the state of body's defense against potentially harmful pathogens such as bacteria, viruses, and fungi [46]. In addition, an abnormal WBC count (which corresponds to a WBC concentration of >10,000 cells/μl or <4,000 cells/μl of whole blood), may be associated with certain hematologic malignancies [47, 48], autoimmune

disorders [49, 50] or even drug toxicities [51-53]. WBC counts test are therefore important diagnostic tools for a number of human diseases and disorders, as well as for monitoring the progression and treatment of such pathological conditions.

Flow cytometry (FC) is the current gold standard for counting WBCs [54]. Although FC instruments have high throughput capacity and accuracy, they are expensive (tens of thousands of dollars), non-portable, consume large volumes (typically in the milliliter range) of blood samples and reagents and require considerable technical expertise for their operation and maintenance. Their use is therefore limited to hospitals and specialized clinics in big cities and renders them unsuitable in the field, at the doctor's office or in small communities that lack both the infrastructure as well as the trained health personnel.

To overcome those issues, microfluidic technology has recently emerged as an alternative approach for replacing the bulky and expensive FC instruments. Due to the unique advantages of small volume sample and reagent consumption, low cost and ease of operation, various microfluidic devices have been developed to address the challenge of WBC (or their subtypes) count on-chip. Such microfluidic devices can be divided into two categories: continuous flow microdevices [55-60] and cell-capturing microdevices [25]. The former ones can be considered as miniaturized FC systems as cells are counted as they flow through the detection region. However, these devices have to be precisely interfaced and aligned with elaborate and bulky fluidic, optical and electrical setups for registering the cells of interest.

In cell-capturing microdevices, cells are mechanically or chemically immobilized on-chip and imaged/counted using a microscope and a CCD camera. Mechanical immobilization approaches typically employ a commercial membrane filter with micron-sized holes for capturing WBCs from whole blood [26]. The membrane filter also functions as a cell separator: WBCs, being larger in size than the red blood cells (RBCs), are captured in the holes while the RBCs squeeze through the holes. However, the holes do not have a consistent shape and size, as a result some holes are fused together leading to the escape of WBCs and low WBC trapping efficiency. Microfabricated silicon-based microfilters have also been proposed for isolating WBCs from human whole blood [27]. These microfilter based devices essentially have a 2D architecture and they capture WBCs through their confinement in a plane. However the cells have the freedom to move in the third dimension leading to their escape and a reduced (72-85%) trapping efficiency.

Chemical immobilization through immunoaffinity-based selection has also been used for capturing WBCs and their subtypes (e.g. $CD4^+$ T-cells). The working principle is straightforward: blood samples flow through a microfluidic device that has previously been functionalized with antibodies against the desired cell surface receptors. In this approach, enumeration of the captured cells is done optically using a microscope [32, 33, 61] or electrically by measuring the impedance change upon cell lysis using on-chip electrodes [62]. Functionalization of those microdevices requires a number of incubation and washing steps while non-specific antibody binding reduces the purity of the functionalized cell population.

HemoCue WBC is a benchtop WBC counting system that does not use microfluidic technology [63]. The system counts WBC concentration in human whole blood by imaging of the stained nuclei of WBCs. This system, although simple to use, is not accurate (accuracy <90%) and is not able to distinguish nucleated RBCs from WBCs while it measures the average light intensity from the bulk of the lysed blood sample.

In this work, we describe a cell-capturing microfluidic chip that mechanically traps human WBCs. The microdevice incorporates a novel 3D architecture in which an array of microholes (termed 'microhole array') is microfabricated on a suspended, thin film that is sandwiched between a two-layer microfluidic network. The proposed device differs from previous membrane-type cell-capturing approaches as it confines WBCs in all the 3 dimensions (a simple membrane confines cells only in 2 dimensions) leading to a high WBC trapping efficiency (>87%). Similar to other cell-capturing devices, the 3D architecture also provides an advantage over flow cytometry approaches as thousands of on-chip trapped WBCs can be imaged/counted simultaneously using standard fluorescent microscopy This precludes the need for precise alignment of optical elements with the microfluidic chip. Although we report results from lysed human blood samples, our microfluidic chip due to its unique two-layer architecture can potentially perform size-based separation of RBCs and platelets from WBCs. We envision the integration of this microdevice with on-chip optical modules and its subsequent development into a generic platform for size-based separation and imaging/counting of different types of cells for various point-of-care applications.

3.2 Materials and methods

3.2.1 Materials

SU-8 photoresist was purchased from MicroChem (Newton, MA) and the polydimethylsiloxane (PDMS) elastomer was obtained from Dow Corning (Midland, MI). Chlorotrimethylsilane was purchased from Sigma Aldrich (St. Louis, MO). Phosphate buffered saline (PBS) was obtained from Mediatech, Inc (Manassas, VA). RBC lysis buffer was obtained from eBioscience (San Diego, CA). Alexa Fluor® 488-conjugated mouse antibody to human CD45 (AF488-anti-CD45) was purchased from Invitrogen (Frederick, MD).

3.2.2 Biochip design

Our 3D cell-capturing chip (**Figure 3.1**) consists of a membrane of ~10,700 microholes, ~4 μm in diameter that are patterned on a 1 μm thick silicon nitride film. The microholes are arranged in a 17x17 array of clusters (289 clusters in total). Each cluster contains 37 microholes and it is separated from its neighboring ones by a distance of 120 μm. The entire microhole array is ~2 mm x 2 mm and it is sandwiched between two microfluidic networks. The top microfluidic network includes: (i) an inlet region that branches into 17 microfluidic channels (termed ‘inlet fluidic arms’) and (ii) 18 microfluidic channels (termed ‘outlet fluidic arms’) that merge into the outlet region. Each inlet fluidic arm is a 60 μm wide, 20 μm deep, dead-end microchannel that delivers WBCs to a single row of clusters (each row contains 17 clusters). The outlet fluidic arms are 26 μm wide, 20 μm thick, dead-end microchannels that are connected to the inlet fluidic arms through the bottom microfluidic network. The bottom microfluidic network

consists of 30 µm long, 1.28 µm thick microchannels (termed ‘microfluidic connectors’) that connect the clusters from a single inlet fluidic arm to two outlet fluidic arms through a set of 4 µm in diameter microholes (termed ‘exit microholes’).

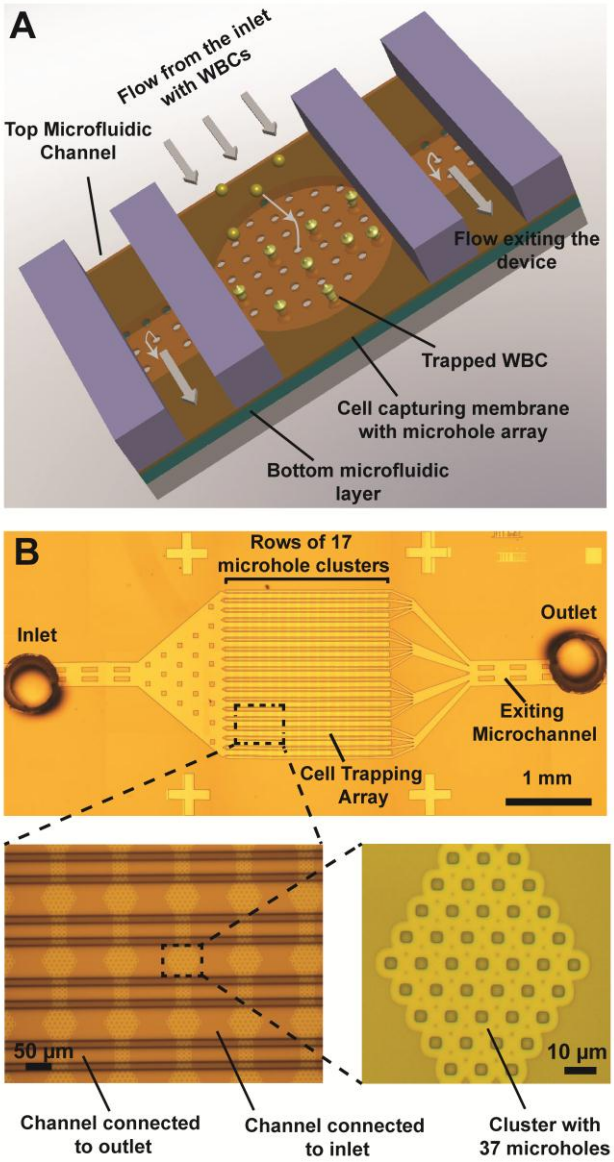

Figure 3.1: (A) 3D illustration of a WBC trapping microhole cluster of the biochip. The cell trapping layer is sandwiched between the top and the bottom microfluidic channels (Top cover is not shown for clarity). **(B)** A snapshot of the microfluidic biochip (12 images were obtained with a 5x microscope objective and stitched together). Enlarged view of the trapping holes with the top microfluidic channels was obtained using a 20x microscope objective. A magnified view of an individual microhole cluster (obtained with a 50x microscope objective) has also been presented.

The working principle of the biochip is purely based on mechanical confinement (**Figure 3.2**): WBCs, due to their large size (7-15 µm in diameter), are spatially restricted and therefore immobilized in the 3 dimensional space that is created by the microhole array and the thin (~1.28 µm thick) bottom microfluidic network. While WBCs are being trapped in the microhole array, the remaining blood continues to flow through the microholes, the bottom microfluidic network and the outlet microchannel of the top microfluidic network. After the entire blood sample is processed, the number of trapped WBCs is counted by examining the microhole array under a fluorescent microscope.

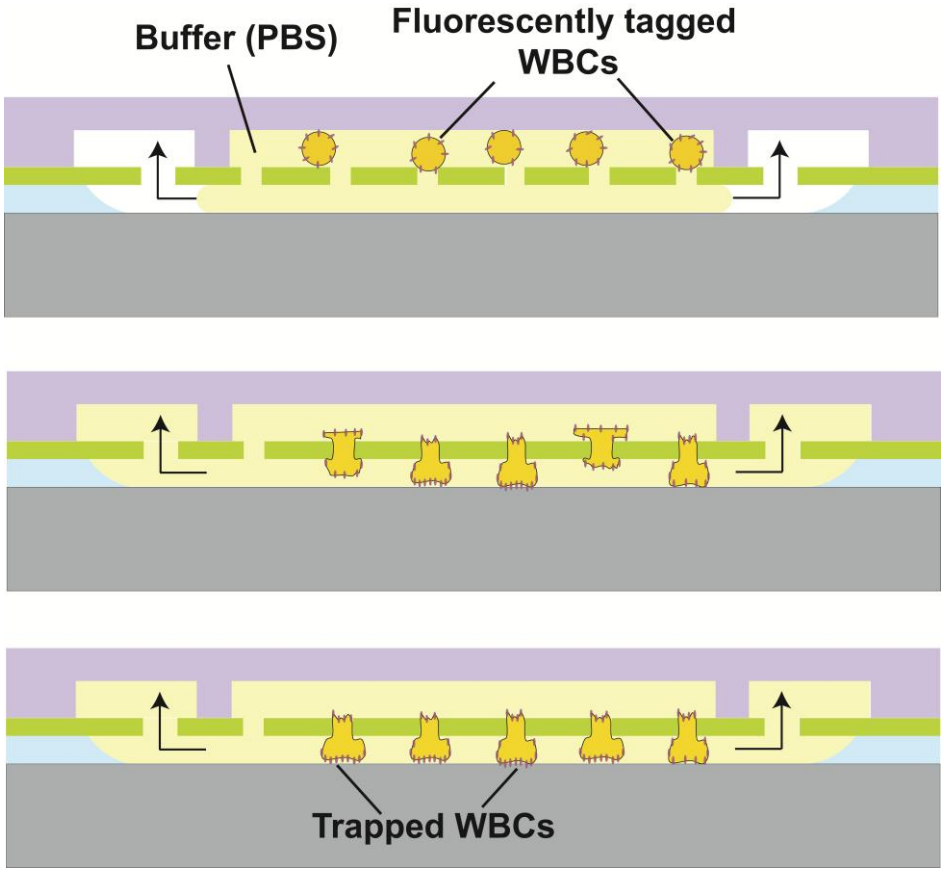

Figure 3.2: Schematic of the trapping of WBCs in the microhole array. Fluorescently tagged WBCs suspended in the buffer solution are injected into the biochip under pressure. While the buffer flows through the microhole array, the WBCs are confined and trapped in the microhole array and their squeezing out is prevented by the bottom microfluidic layer.

3.2.3 Biochip microfabrication

The biochip consists of two microfabricated modules: the cell trapping module and the sample delivery module (**Figure 3.3**). The microfabrication of the trapping module starts with a low pressure chemical vapor deposition (LPCVD) of a silicon dioxide and a low stress silicon nitride layer (1.28 μm and 1 μm thick respectively) on a silicon substrate. The microhole array is then patterned on the silicon nitride layer using photolithography and reactive ion etching (RIE). An isotropic, HF time-etch step of the underlying silicon oxide layer is finally performed to obtain the microhole array and the bottom microfluidic network. The sample delivery module consists of a network of PDMS microfluidic channels fabricated using soft lithography. A 20 μm thick layer of SU-8 photoresist is spun and photolithographically patterned on a silicon wafer to obtain the microfluidic mold. PDMS is then cast on the SU-8 mold, cured at 65ºC for 2h and peeled off to obtain the sample delivery module. Silanization of the SU-8 mold prior to PDMS casting minimizes stiction of the cured PDMS. Holes are punched into the PDMS mold with a sharpened 19-gauge needle to obtain the inlet and outlet ports. Finally the silicon nitride and the PDMS surfaces of the two modules are exposed to air plasma (120 mTorr, 30 W, 15 s) [64], aligned manually under a light microscope and bonded together.

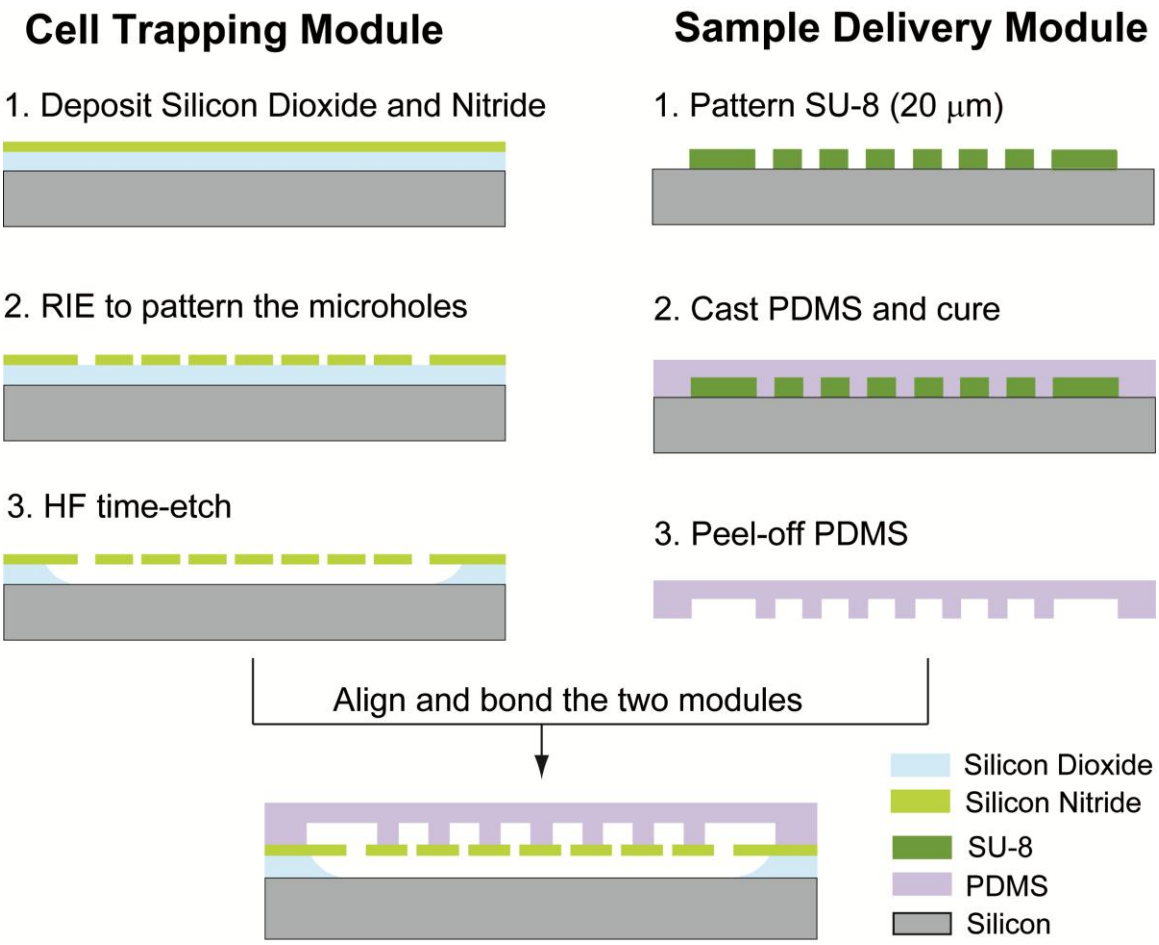

Figure 3.3: The microfabrication process of the cell trapping biochip. The cell trapping and the sample delivery modules are fabricated separately and subsequently aligned and bonded under an upright microscope using a 5x microscope objective.

3.2.4 Fluid flow simulations and modeling

Parameters of the fluid flow through the biochip (pressure, volumetric flow rate and microfluidic resistance) were obtained using a combination of numerical (computational fluid dynamics (CFD)) and resistive electrical circuit modeling [65]. The top and bottom microfluidic networks were modeled using electrical circuit elements while the clusters were modeled using COMSOL. All microchannels in the two networks were represented as ohmic resistors with zero capacitance. The simulations were

performed in LT Spice IV software assuming that there are no WBCs present in the microhole array. Assuming rectangular geometry, the resistance (R) for each microfluidic segment (inlet and outlet fluidic arms, microfluidic connectors) was estimated by [66]:

$$R = \frac{12\eta l}{1 - 0.63(\frac{h}{w})} \frac{1}{wh^3}$$

where *l*, *w* and *h* are the length, width and height of the rectangular microfluidic segment respectively and η is the viscosity of the fluid (we used the viscosity of water (η = 10^{-3} Pa-s) in our calculations).

The microfluidic resistance of a single cluster ($R_{cluster}$) was estimated in COMSOL using the laminar flow module. In those simulations, the fluidic resistance of a single microhole ($R_{microhole}$) was calculated by dividing the pressure drop across it by the volumetric flow rate through it. Subsequently, the microfluidic resistance of an entire cluster ($R_{cluster}$) was obtained by considering that all 37 microholes in the cluster are ohmic resistors connected in parallel ($R_{cluster} = R_{microhole} / 37$).

3.2.5 Blood sample preparation and biochip operation

All experiments were performed with lysed human blood samples. 20 µl of finger-prick human whole blood samples were initially tagged with monoclonal CD45 fluorescent antibodies (Alexa Fluor® 488-anti-CD45, excitation 495 nm, emission 519 nm, Invitrogen Inc.) in the ratio 10:3 (to label all the WBCs). Subsequently, the red blood cells (RBCs) were removed by incubating the blood sample with a lysis buffer (eBioscience, San Diego, CA) for 10-15 min. The WBCs were then collected via

centrifugation and finally diluted in PBS buffer (1x Dulbecco's Phosphate Buffered Saline) to a total volume of 20 µl. 1 µl aliquots of this buffer solution (containing WBCs) were subsequently used for experiments.

At the beginning of every experiment and before loading the blood sample**,** a purging step with PBS buffer was performed to remove air bubbles from the biochip and to ensure uniform flow conditions. All experiments were performed under constant pressure in order to eliminate WBC escape and/or rupture due to pressure buildup during the WBC trapping process. That was achieved by connecting the inlet of the biochip to a compressed air supply through a digital pressure controller (model number PC-30PSIG-D/5P, Alicat Scientific, Inc.). The outlet of the biochip was exposed to the atmospheric pressure.

3.2.6 WBC counting

Fluorescently tagged WBCs were counted in the inlet region, the cell trapping array and the outlet region of the biochip using an upright epi-fluorescent microscope equipped with a low-light CCD camera (QuantEM: 512SC, Photometrics Inc.). The WBC number in the inlet region and the cell trapping array was obtained by analyzing images from those regions at the end of each experiment (e.g. when 1 µl of lysed blood sample was processed through the biochip). The fluorescent images were analyzed using commercial imaging software (MetaMorph, Molecular Devices Inc.). Fluorescent impurities (e.g. residuals formed during lysing, dust particles, etc) that could alter the WBC count, were eliminated by comparing their size and fluorescence intensity with the

average size and fluorescent intensity of manually-identified WBCs. WBCs that exited the cell trapping array were manually counted on the fly by continuously monitoring the flow through the outlet region of the biochip.

3.3 Results

3.3.1 Uniform pressure and flow rate distribution in the biochip

We performed CFD simulations using COMSOL software to obtain the maximum pressure difference across the 37 microholes of a single cluster for different trapping scenarios. The maximum pressure difference across the microholes determines the tendency of an incoming cell to remain trapped or squeeze out. It is therefore an important parameter that affects the trapping efficiency. We varied the number of WBC-filled microholes (we assumed that there is no flow through a microhole when a WBC is trapped) and obtained the resulting maximum pressure difference across the remaining open microholes in the cluster. A 3 psi pressure difference between the inlet and outlet of the simulated fluidic domain was used. Our results (**Figure 3.4**) suggest that the maximum pressure difference (ΔP_{max}) across the open (unfilled) microholes in a cluster remains relatively stable for up to ~70% microhole occupancy (occupancy = number of WBC-filled microholes in the cluster / total number of microholes in the cluster). However beyond 70% microhole occupancy, ΔP_{max} rises considerably which can lead to cell escape and reduced trapping efficiency. Considering the 70% occupancy limit and the fact that our microfluidic chip has a total of 10,700 microholes, it is expected that the chip can efficiently trap up to ~7,500 WBCs (70% occupancy) before there is a significant pressure drop across the remaining open microholes. That number of WBCs is

compatible with finger-prick point-of-care devices that typically process ~0.5 µl of whole blood [67] (0.5 µl of blood contains an average of 3,000-5,000 WBCs in healthy individuals).

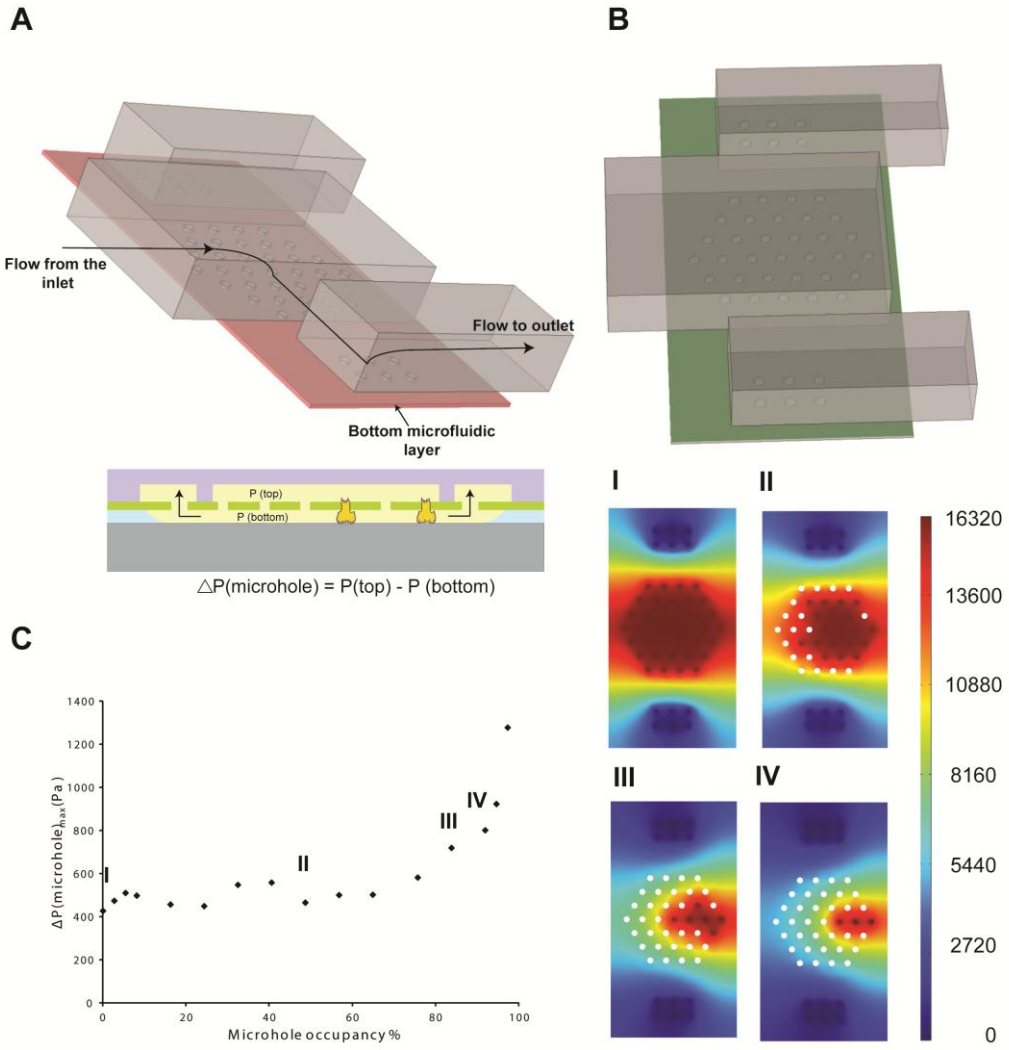

Figure 3.4: (A) COMSOL geometrical model used to simulate the pressure profile through an individual microhole cluster. The arrows signify the direction of flow into the device, passing through the microhole cluster and the bottom microfluidic layer and subsequently exiting through the outlet channel. The cross section schematic shows the pressure difference across an unoccupied microhole. **(B)** Pressure profile (in Pa) has been presented for the top plane of the bottom microfluidic layer (indicated in green). The white and the dark circles indicate the occupied and the unoccupied microholes respectively. (I), (II), (III) and (IV) correspond to 0, 18, 31 and 34 microholes occupied in the cluster (out of 37 holes). **(C)** Maximum pressure difference across a microhole cluster as a function of the % of the microholes (in the cluster) occupied by the cells.

Furthermore, using the duel modeling approach described above and assuming pressure driven flow, we obtained the flow rate through each of the 17 clusters in a single inlet fluidic arm (**Figure 3.5**). We observed that the maximum and minimum relative flow rates (the relative flow rate is the ratio of the flow rate through a cluster divided by the total flow rate entering the inlet fluidic arm) were 6.3% and 5.7% respectively, indicating that the flow is divided almost equally among all clusters in a single inlet fluidic arm. This small variation can be attributed to the high microfluidic resistance of each of the microfluidic connectors ($R \sim 9.1 \times 10^{15}$ Pa-s/m^3) which exceeds the resistance of the inlet fluidic arm ($R \sim 10^{13}$ Pa-s/m^3) and of a cluster ($R \sim 3.5 \times 10^{13}$ Pa-s/m^3) by three and two orders of magnitude respectively. Maintaining a uniform flow distribution among all clusters in an inlet fluidic arm ensures an equal probability of trapping WBCs in the array. We avoid modeling the entire biochip, as all fluidic arms are connected in parallel to the inlet and outlet regions and therefore they experience identical flow conditions.

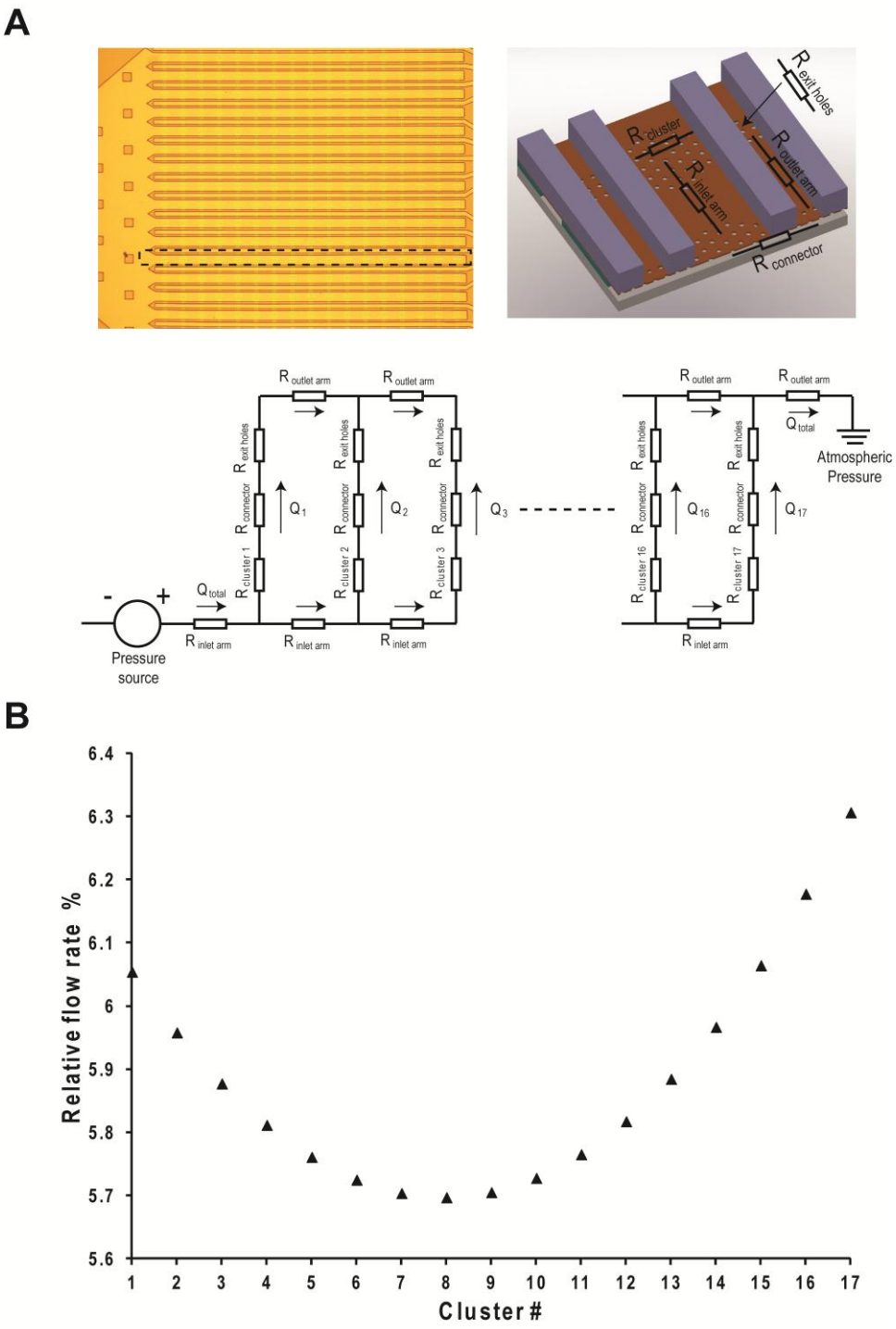

Figure 3.5: (A) Resistive electrical circuit to analyze the distribution of flow through different trapping microhole clusters (1-17) along the length of one of the 17 microfluidic inlet arms. $R_{cluster\ 1\text{-}17}$ indicate the fluidic resistances of the microhole clusters 1-17 respectively. All the resistances used for the resistive electrical circuit modeling have been illustrated using a 3D cross section. $R_{connector}$ exceeds any other resistance in the network by at least two orders of magnitude. This resistive circuit was analyzed using LT

Spice IV software to obtain the flow rates through each of the 17 microfluidic arms. **(B)** % of the total flow passing through each of the microhole clusters in the beginning of the flow (no cell trapped). Flow distributes almost equally among all the 17 clusters.

3.3.2 Maximum WBC trapping efficiency

In order to obtain the optimum pressure that resulted in the highest trapping efficiency (E_{Trap}), we conducted experiments at a pressure range of 1-7 psi with blood 1 μl blood samples containing at least 200-500 WBCs (**Figure 3.6**). We defined E_{Trap} at a given pressure as the percentage ratio of WBCs captured in the cell trapping array over the total number of WBCs processed through the biochip:

$$E_{Trap} = \frac{Number\ of\ captured\ WBCs}{Total\ number\ of\ WBCs}$$

The total number of WBCs was calculated by adding the number of WBCs that remained in the inlet region (N_{in}), the ones that trapped in the array (N_{array}) and the ones that escaped in the outlet region of the biochip (N_{out}). We also calculated the WBC escape yield (Y_{escape}) that is the percentage ratio of N_{out} over the sum of N_{array} and N_{out}. The Y_{escape} does not consider the N_{in} and hence it is a more realistic indicator of the ability of the microhole array to capture WBCs.

Our results indicate that the E_{Trap} reaches a maximum value of ~90% (average from 4 measurements) at 3 psi. At lower pressures, E_{Trap} decreases by approximately 10%. This decrease can be attributed to the higher number of WBCs remaining in the inlet region due to the low flow rate/WBC speed. Beyond 3 psi, E_{Trap} decreases linearly with pressure as a larger number of WBCs squeeze through the microholes and escape

the biochip. It was also observed that a slightly higher percentage of WBCs escape the array at 1-2 psi when compared to the optimum pressure of 3 psi (**Figure 3.6**, % WBC escape curve). This counterintuitive observation can be attributed to the longer time that is required for the 1 μl of blood sample to flow through the biochip at low pressures. A prolonged processing time causes initially trapped WBCs to squeeze out of the array and finally exit the biochip. Beyond 3 psi, as anticipated, the Y_{escape} increases with pressure reaching a value of 24-30% at 7 psi. For pressures 7 psi and above, the high flow rate resulted in an inaccurate count of the number of WBCs exiting the biochip using the imaging modality described earlier. At pressures 1 psi and below, the flow was extremely slow, leading to an aggregation of a high number of WBCs in the inlet region.

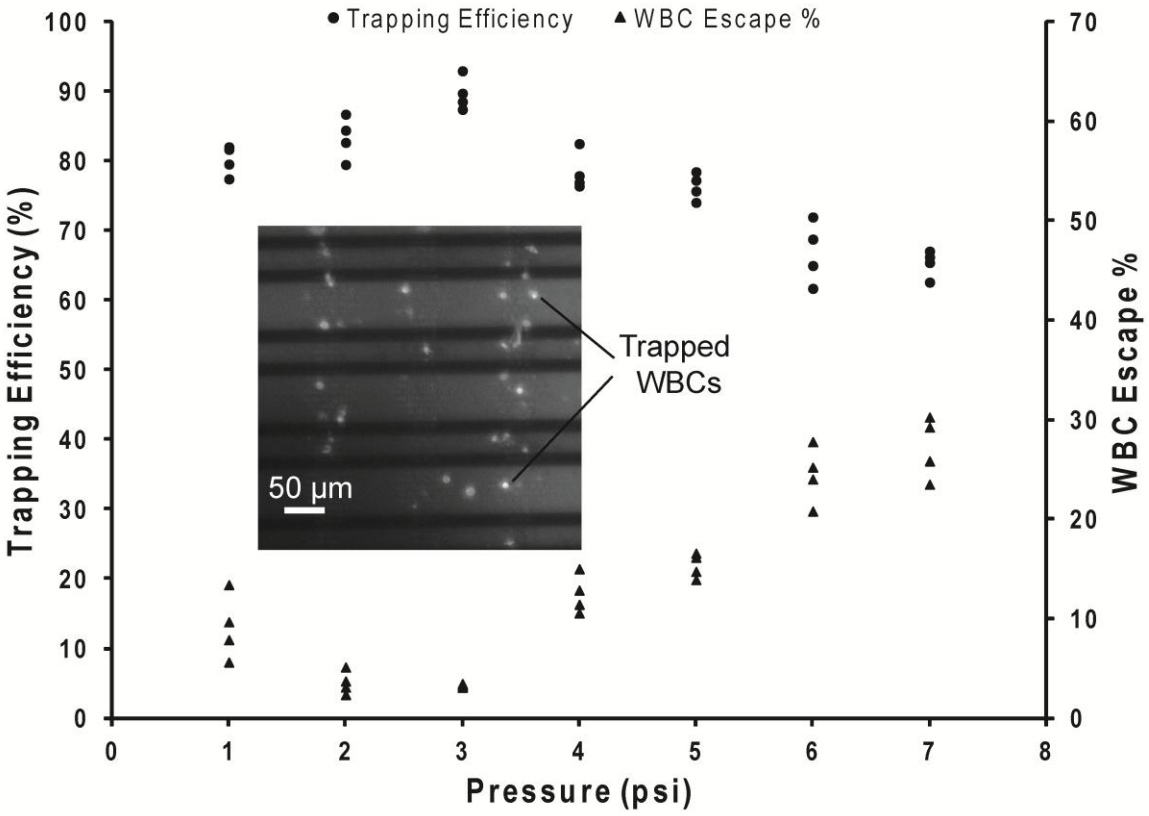

Figure 3.6: Biochip trapping efficiency and WBC escape % versus pressure. Each data point represents result from a single WBC trapping experiment using a new biochip for every experiment. Four devices were used for each pressure value. For all these

experiments, the number of input cells was in the range 180-500. Maximum trapping efficiency was obtained for 3 psi pressure. Snapshot depicts the fluorescently tagged white blood cells trapped in the microholes.

3.3.3 WBC trapping efficiency versus number of processed WBCs

We furthermore measured the trapping efficiency for different WBC concentrations (100–1000 WBCs/μl) at the optimum pressure of 3 psi (**Figure 3.7A**). We chose ~100 WBCs per μl to be the lower limit as this represents the extremely low number of WBCs present in patients with a weak immune system (e.g. end-stage AIDS patients). To achieve low WBC concentration values, blood samples were diluted by 5-6 fold after the lysis step. In the above range of input WBC concentrations, E_{Trap} exhibited small variations, ranging between 87-95%. The WBC escape percentage (**Figure 3.7B**) varied between 1.8 - 3.6%, indicating that a very low number of processed WBCs was able to squeeze out of the array.

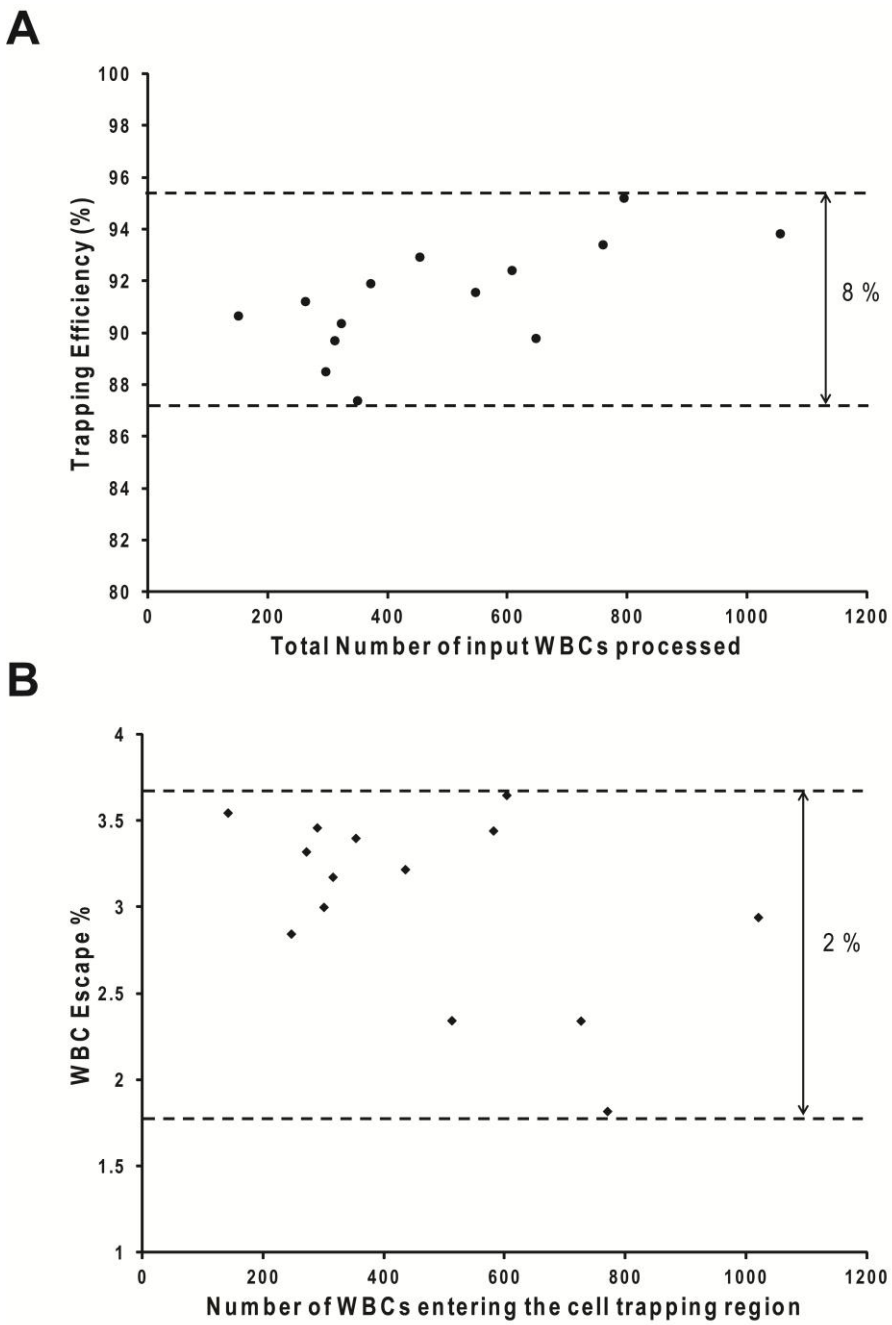

Figure 3.7: (A) Biochip trapping efficiency versus number of input WBCs. **(B)** WBC escape % versus number of WBCs entering the cell trapping region (i.e. total number of input WBCs – number of WBCs stuck in the inlet region). Each data point represents result from a single WBC trapping experiment using a new biochip for every experiment. For all these experiments, 3 psi pressure was used. The trapping efficiency has an 8% range (max value – min value). Maximum escape % value of 3.65 was obtained from these experiments.

3.4 Discussion

We presented a novel 3D microfluidic architecture for capturing WBCs. Although the trapping efficiency of our biochip is higher than other size-based cell trapping approach by 5-15% [27], the ultimate limit of trapping all WBCs was not achieved for two reasons: (i) a small number of WBCs – probably the ones with the smallest diameter (e.g. lymphocytes) - were able to escape the array and (ii) some WBCs adhered at the inlet of the biochip. The latter reason had a dominant effect on reducing the trapping efficiency as the number of WBCs adhered at the inlet region was 2-3 times higher than the number of WBCs that escaped the microhole array. We anticipate that the functionalization of the microfluidic walls with a blocker against non-specific protein binding (e.g. bovine serum albumin (BSA) solution) [68] would minimize cell adherence and therefore significantly increase the trapping efficiency. Moreover, reducing the diameter of the microholes could further increase the trapping efficiency as the smallest WBCs will not be able to escape. An alternative strategy for capturing the smallest WBCs would be to decrease the thickness of the bottom microfluidic network. Such an approach is not recommended though as it can dramatically increase the fluidic resistance and therefore the time needed to process the blood sample.

Our simulation results indicate that the E_{Trap} of the proposed design is not affected by the total number of WBCs trapped as long as that number does not exceed ~7,500 WBCs (70% occupancy of the array). That number is larger than the number of WBCs expected in most patients with compromised immune system (3,500-5000 WBCs/ μl). In

any case, the size of the microhole array can be easily scaled up if a large number of WBC needs to be processed.

Finally, we should emphasize that all our experiments were performed with lysed human whole blood samples. The removal of RBCs from whole blood was necessitated due to their overwhelming number (~6 million RBCs in 1 μl) over the number of WBCs. Experiments were also performed with whole blood samples, but they were not successful: RBCs tend to stick to the microhole array, clogging the biochip. The clogging was not that severe when highly diluted whole blood samples (1:100 blood/buffer) were used; however the time required for processing the large volume of the diluted sample increased considerably (15-20 min at 3 psi). This resulted in a decrease in the trapping efficiency as many trapped WBCs eventually squeezed out of the microhole array. Future biochip designs can incorporate an on-chip RBC lysis chamber [69] and/or a metering chamber [70, 71] upstream of the microhole array. Such an integration scheme would eliminate the various off-chip lysis/dilution steps and potentially improve WBC viability as well as the overall performance of the biochip.

3.5 Conclusions

Monitoring of diseases that compromise the immune system (e.g. HIV/AIDS, aplastic anemia) is performed by counting WBCs and/or their subtypes. In this chapter, we presented a novel microfluidic chip for trapping and counting WBCs in minute volumes of lysed, diluted blood samples. The biochip incorporates an array of ~10,700 microholes that is sandwiched between two microfluidic networks. This unique

architecture enables the three-dimensional confinement/trapping of WBCs in the array, resulting in a high trapping efficiency (>87%). Although, the current design requires the use of a fluorescent microscope for counting the number of WBCs, we envision the development of an integrated optofluidic system that will report the WBC count automatically. The use of such a system can be extended to other types of cells including specific sub-populations of WBCs (e.g. CD4+T cells) or even circulating tumor cells (CTCs) for point-of-care monitoring at home, at the physician's office or at a resource-limited setting.

CHAPTER 4

A Polymer-based, Planar Microlens Array For Imaging Micron-sized Objects

In this chapter, we present a novel microfabrication approach for obtaining arrays of planar, polymer-based microlenses. The proposed microlenses arrays consist of deformable, elastomeric membranes that are supported by polymer-filled microchambers. Each membrane/microchamber assembly is converted into a solid microlens when the supporting UV–curable polymer is pressurized and cured. By modifying the microlens diameter (40-60 μm) and curing pressure (7.5-30 psi), we demonstrated that it is possible to fabricate microlenses with a wide range of effective focal lengths (100–400 μm) and numerical apertures (0.05-0.3). We obtained a maximum numerical aperture of 0.3 and transverse resolution of 2.8 μm for 60 μm diameter microlenses cured at 30 psi. These values were found to be in agreement with values obtained from opto-mechanical simulations. We envision the integration of these microlenses arrays with cell capturing microfluidic biochips (presented in chapter 3) for point-of-care cell counting applications.

4.1 Introduction

Microlenses are used in optical communication [72, 73], displays [74, 75], optical sensors [76, 77], photolithographic systems [78, 79] as well as in biomedical imaging applications [80-82]. Recent advances in micromachining technology led to the development of a variety of microlens microfabrication approaches including photoresist-

reflow and transfer methods [35, 83], ink jet processes of UV curable polymers [37], hot embossing techniques [84], micromolding using silicon substrates [44, 85], soft lithography-based replication processes by molding various materials against rigid or elastomeric molds [41, 42, 86]. Photoresist-reflow methods rely on the surface tension of the photoresist to form a smooth microlens surface. These methods require accurate control of the microfabrication parameters (photoresist thickness, hydrophobicity) and produce microlenses with small numerical aperture (NA) due to the small aspect ratio (thickness vs diameter) of the patterned photoresist. Ink-jet methods are serial processes that require an elaborate experimental setup for accurately dispensing small drops of the optical material onto a rigid substrate. The properties of ink-jet processed microlenses depend on the rheological properties of the dispensing material (viscosity, surface tension), making the fabrication of microlenses with small diameters (<100 μm) and large aspect ratio (to achieve high NA), a challenging task. Hot embossing techniques produce microlenses with rough surfaces and suffer from post-embossing shrinkage. Fabrication of silicon molds requires isotropic wet etching of silicon and deposition of silicon oxide/nitride as the etchant mask. These fabrication steps are extremely time consuming and expensive. Soft lithography-based replication processes provide low-cost microlens arrays whose properties depend on the quality of the master mold. These processes take advantage of the excellent optical [87] and mechanical [88, 89] properties of the polydimethylsiloxane (PDMS) elastomer. PDMS has low elastic modulus, minimum light absorption in the visible spectrum and extremely low autofluorescence, it is therefore an ideal optical material for microlens molding and replication processes [90, 91].

In this work, we describe a novel array of polymer-based, solid microlenses with a numerical aperture (NA) of ~0.3. Key element is the microfabrication of an 'inflatable', polymer-filled PDMS mold that consists of an array of circular microchambers enclosed by flexible membranes. When the mold is inflated, the microchamber/membrane array is converted into a microlens array. Using a UV-curable polymer as a filling medium, the microlens arrays can be subsequently solidified when the desired focal length is obtained. The proposed approach has three major advantages: a) the microlens focal length can be adjusted by regulating the pressure applied to the filling polymer during curing, b) the use of PDMS as the mold material enables large membrane deflections that result in microlenses with high NA, and c) the optical properties (e.g. index of refraction) of the microlenses can be varied as there is a large collection of commercially available curable materials. We envision such microlens arrays to play a key role in various lab-on-chip detection systems for imaging micron-size objects (cells, viruses, etc.) [33, 92]. In particular, they can be integrated with the WBC capturing biochip (discussed in chapter 3) for the development of a point-of-care WBC counting system.

4.2 Design and Microfabrication of the Microlens Array

The inflatable PDMS mold has a two-layer architecture (**Figure 4.1**): (i) the first layer (the 'microlens' layer) contains the circular microchamber/membrane array, and (ii) the second layer (the 'support' layer) contains an array of thick (~200 μm thick) square microwells aligned on top of the microchamber/membrane array. The main purpose of the second layer is to facilitate the handling of the thin first layer during the microfabrication process (see next paragraph for details). A microfluidic network

patterned on the first layer is used to deliver the UV-curable polymer into the microchambers. The increase in pressure within the microfluidic network induces a uniform deflection of the PDMS membranes across the array. That results in the formation of an array of plano-convex microlenses with a pressure-dependent focal length and NA. When the pressure is stabilized within the network (typically in few seconds), the polymer is ready to be UV-cured to obtain the solid microlens array.

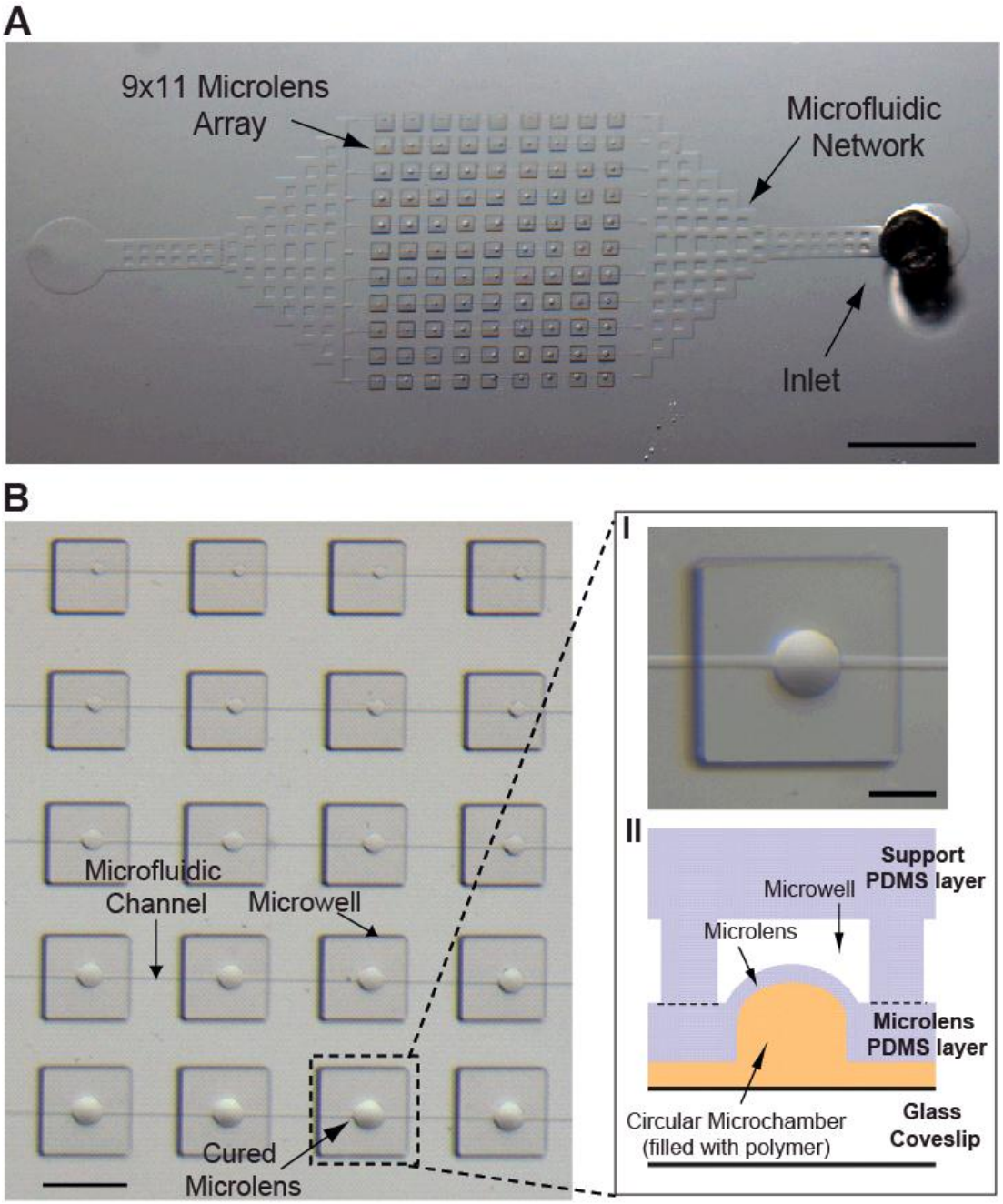

Figure 4.1: (A) A picture of a 9x11 PDMS-based, planar microlens array. The right inlet is used to fill up the microfluidic network with the UV curable polymer (the left inlet is not used in the depicted design). Scale bar, 1.5 mm. **(B)** A close-up view of 16 cured microlenses of different diameters. Each microlens sits beneath a square microwell. Scale bar, 200 µm. A magnified top view of a 60 µm in diameter microlens cured at 30 psi and a schematic diagram of its cross section are shown on the right (I and II respectively). Scale bar, 50 µm.

The microfabrication process of the microlens array involves (**Figure 4.2**): i) the fabrication of two SU-8 master molds (for each of the two PDMS layers) using standard photolithographic processes, ii) the fabrication of the inflatable PDMS mold from the two SU-8 master molds using soft-lithography, and iii) the injection and curing of the UV-curable polymer into the inflatable PDMS mold.

The fabrication of the first SU-8 master mold (corresponding to the microlens PDMS layer) is performed in a two-step photolithographic process [90]. A 13 μm thick film of SU-8 photoresist is patterned on a silicon wafer to define the microfluidic network, followed by the patterning of a second, 40 μm thick, SU-8 film to form the circular microchambers. A 20:1 PDMS mixture is then spun at 1750 rpm and cured on the two-step SU-8 mold to obtain a ~52 μm thick PDMS layer. Such a PDMS composition results in a layer of low elastic modulus (<1MPa [93]), which is necessary to achieve large membrane deflections, and therefore high NA microlenses. By accurately measuring the thickness of SU-8 circular microchambers and the PDMS microlens layer, we estimated the PDMS membrane thickness to be 12.1 ± 1.4 μm (16 measurements were taken from different runs using a profilometer).

The second SU-8 mold (corresponding to the support PDMS layer) is fabricated by patterning a 50 μm thick SU-8 film. The design incorporates an array of 200 μm x 200 μm square microwells, each one sitting on top of a single microlens. A thick (~1 mm) PDMS layer (the support layer) is subsequently cured, peeled off and air-plasma bonded (90 W, 35 sec) to the PDMS microlens layer. Finally, the two-layer PDMS assembly is

detached from the first SU-8 mold and bonded to a 175 µm thick glass slide to create the sealed inflatable PDMS mold. The use of the support PDMS layer is critical for peeling off the thin microlens layer as it provides structural integrity and eliminates the microlens membranes from tearing apart. The inflatable PDMS mold is then filled with a UV curable polymer, pressurized and cured.

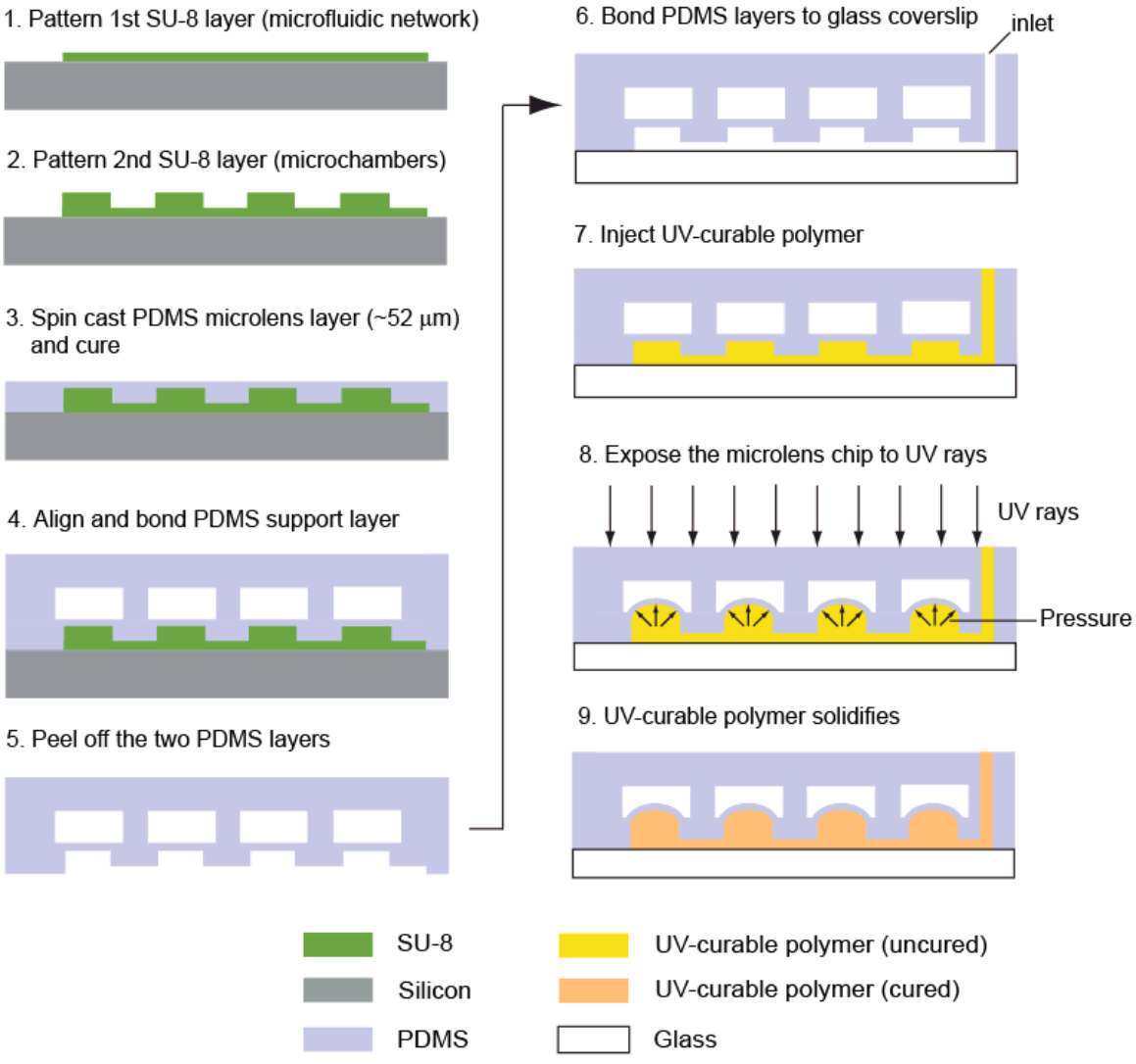

Figure 4.2: The microfabrication process of the microlens device.

4.3 Results

To obtain the optical properties of the proposed high NA, solid microlenses, we characterized an array of 40 μm and 60 μm diameter microlenses following the microfabrication process described above. A high index of refraction UV-curable polymer (Norland 60, index of refraction n = 1.56) was injected into the inflatable PDMS mold and cured (10 min, at 365 nm (Entela UV lamp)) under constant pressure to ensure uniform deflection across the membrane array. The effective focal length (EFL) of the cured microlens device was measured for a range of curing pressures (7.5-30 psi) using a custom-made optical setup (**Figure 4.3**). The EFL corresponds to the distance between the top surface of a microlens and the best-focused image formed when passing a laser beam (532 nm) through the microlens. We followed a 2-step sequence to determine the EFL: i) the top surface of a microlens was visually identified and set as the reference plane (plane I), and ii) the plane containing the image of the focused laser beam was brought into the imaging plane of the microscope objective (plane II) by vertically moving the microlens. The distance between these two planes corresponded to the EFL of the microlens. Plane II was identified by extracting the plane of the maximum light intensity through image analysis software (Metamorph®).

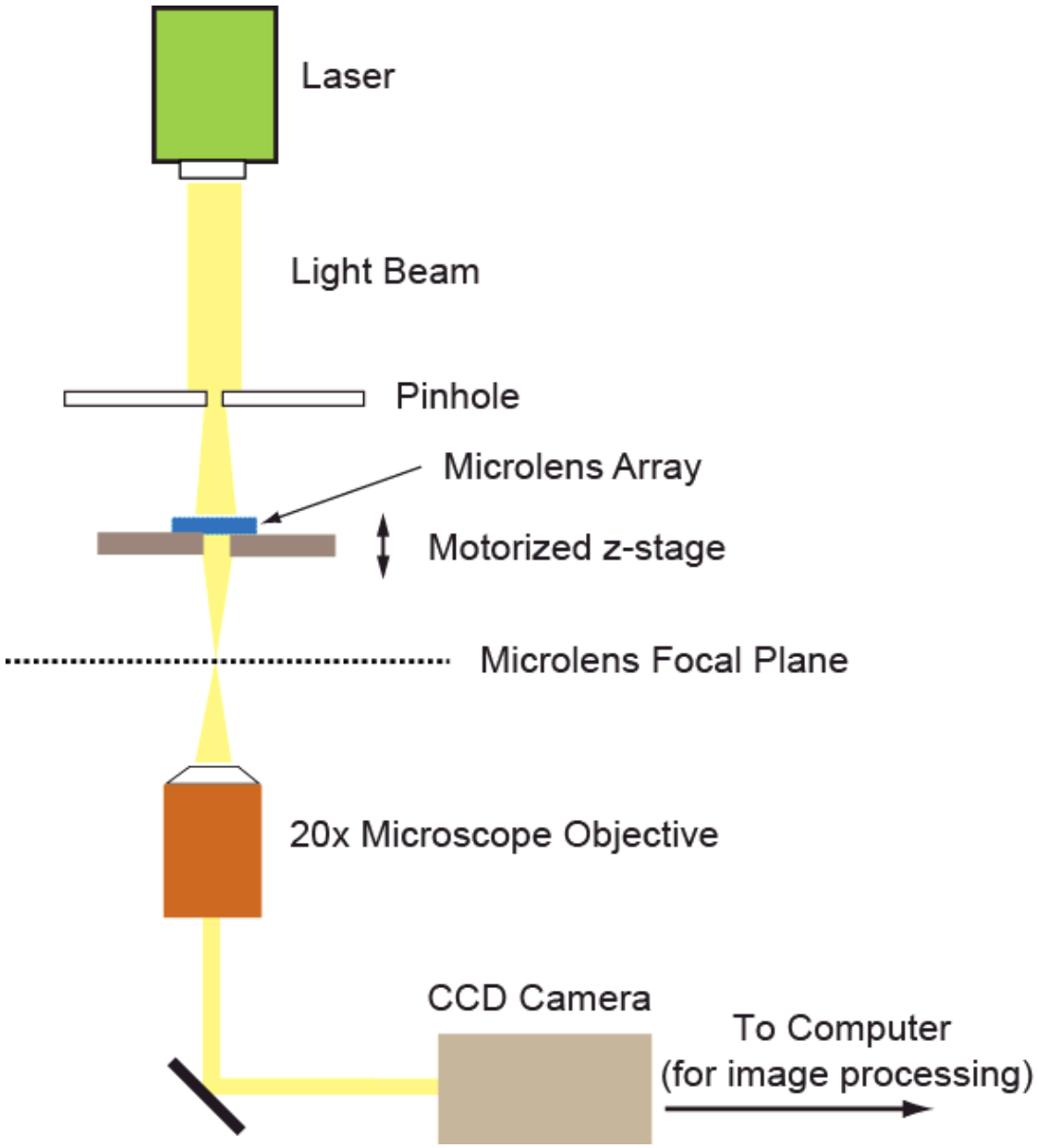

Figure 4.3: Schematic of the experimental setup for characterizing the optical properties (effective focal length (EFL), point spread function (PSF)) of the microlens device. A laser (532 nm) was used to obtain the EFL while a white light source was used to obtain the PSF.

The EFL of both the 40 µm and 60 µm diameter microlenses exhibited a strong dependence on the curing pressure (**Figure 4.4**). EFL changes up to ~200 % were measured over the entire pressure range. For low pressures (< 7.5 psi), the circular membranes undergo small (sub-µm) deflection. These microlenses weakly focus the laser beam resulting in a large depth of focus (several mm's) that makes it difficult to assign a single value to the focal length. High pressures (>30 psi) resulted in breakage of the microlens membranes. Experimental EFL data were also compared with opto-mechanical simulation values. The pressure-dependent microlens profiles were simulated using commercially available finite element analysis software (ANSYS). The deflected membrane profiles were imported into an optical design software (OSLO LT) to determine the corresponding EFLs. Simulations were performed for a membrane thickness of 10.7 µm and 13.5 µm to capture the upper and lower limit of the corresponding measured values. The elastic modulus and Poisson ratio of the PDMS membrane was set to 3 MPa [89] and 0.49 respectively. A refractive index of 1.41, 1.56 and 1.51 was used for the PDMS, the UV-curable polymer and the glass slide respectively. The experimental EFL values for both the 40 µm and 60 µm diameter microlenses were within the simulated upper and lower EFL bounds.

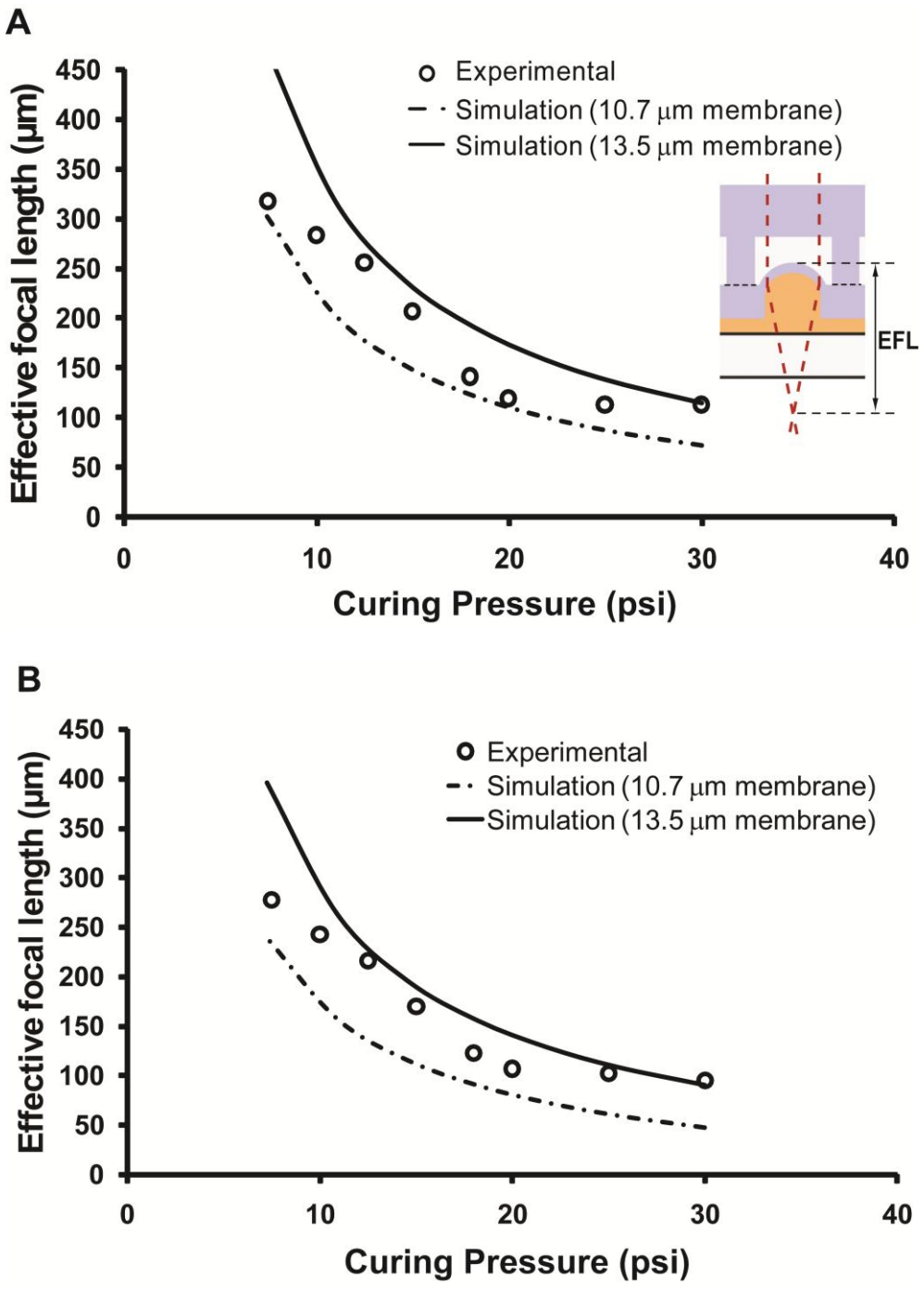

Figure 4.4: Effective Focal Length (EFL) versus curing pressure for **(A)** 40 μm and **(B)** 60 μm diameter microlenses. Experimental and opto-mechanically simulated EFL values are obtained for a pressure range of 7.5-30 psi. Each data point is the average of 16 measurements from 2 microlens devices (8 microlenses/device). The measured EFL values have standard deviation of 4.31% and 4.10% for 40 μm and 60 μm diameter microlenses respectively.

The numerical aperture (NA) of the microlenses (for use in air) was estimated from [94] where *a* and *F* represent the microlens radius and EFL respectively.

$$\mathrm{NA} = \sin\left[\tan^{-1}\left(\frac{a}{F}\right)\right] \quad (1)$$

Based on the EFL values reported above, a maximum NA of ~0.17 and ~0.3 was obtained for 40 µm and 60 µm diameter microlenses cured at 30 psi respectively (**Figure 4.5**). The light loss through a single microlens was obtained by measuring the decrease in the light intensity of white light passing through the microlens device. For microlenses cured at 30 psi, the light loss was found to be 0.86 dB (18 %).

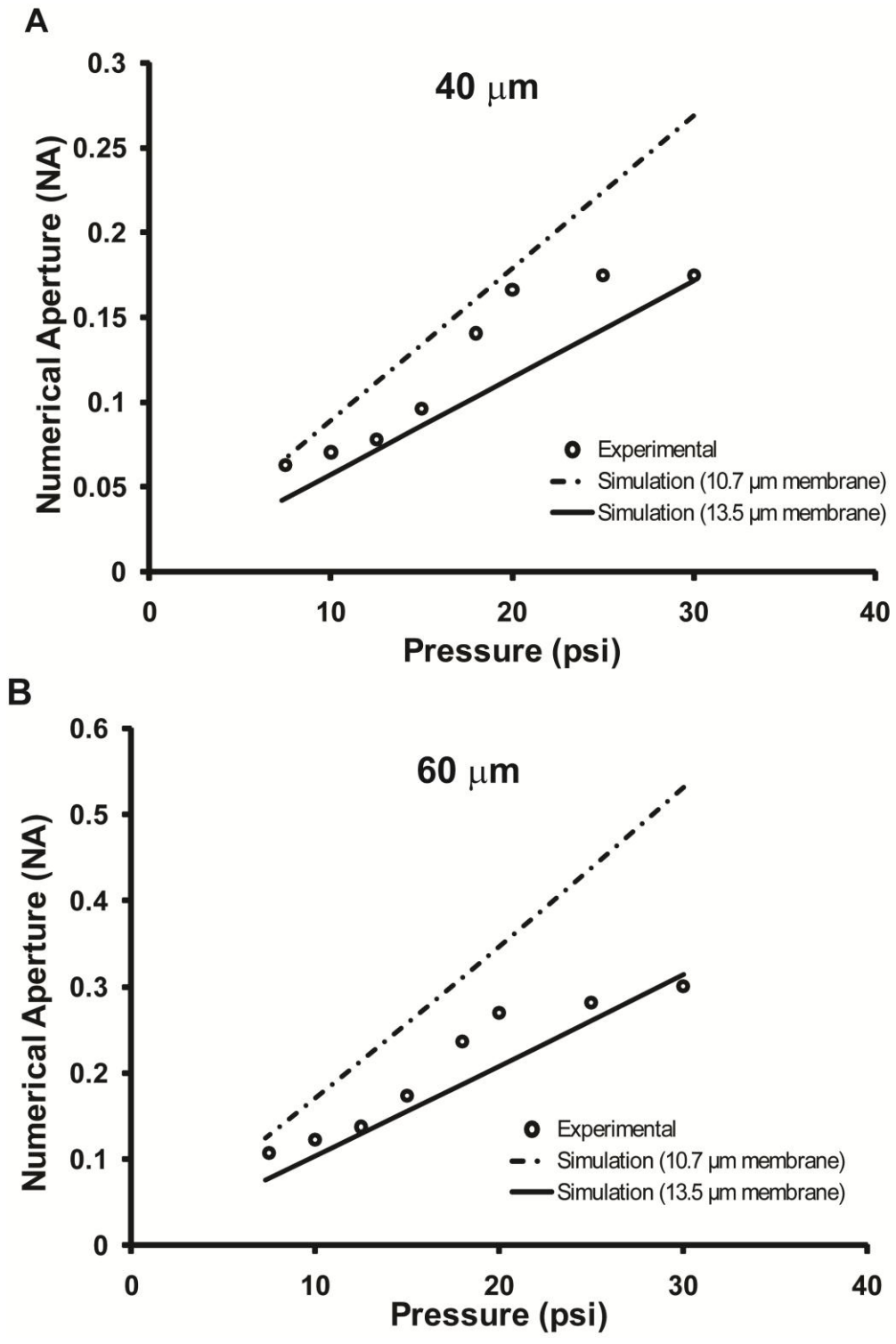

Figure 4.5: Numerical Aperture (NA) versus curing pressure for **(A)** 40 μm and **(B)** 60 μm diameter microlenses. NA values are calculated using the EFL values presented in Figure 4.4. 60 μm diameter microlenses (with lower EFL) have higher NA than 40 μm diameter microlenses (with higher EFL).

To characterize the surface profile of a single microlens from the array (**Figure 4.6A**) we used a white-light interferometer (Veeco NT9100). We obtain direct optical access to the array by immersing the microlens device in acetone for 10 minutes and manually detaching the support layer. A 25 nm thick, gold layer was subsequently evaporated on the microlens surface to acquire a clean interferometric image. The PDMS membrane profile of a 60 μm diameter solid microlens showed a maximum deflection of ~6 μm when cured at 30 psi, corresponding to a microlens with an aspect ratio of 10:1 (**Figure 4.6B**). The microlens profile (**Figure 4.6**) allows us to determine the minimum microlens pitch (microlens center-to-center distance). For 60 μm microlenses cured at 30 psi, the membrane deformation extends up to ~40 μm from the center of the microlens, and therefore they can be placed as close as 80 μm apart. Microlenses of smaller diameter or cured at lower pressures will have smaller pitch.

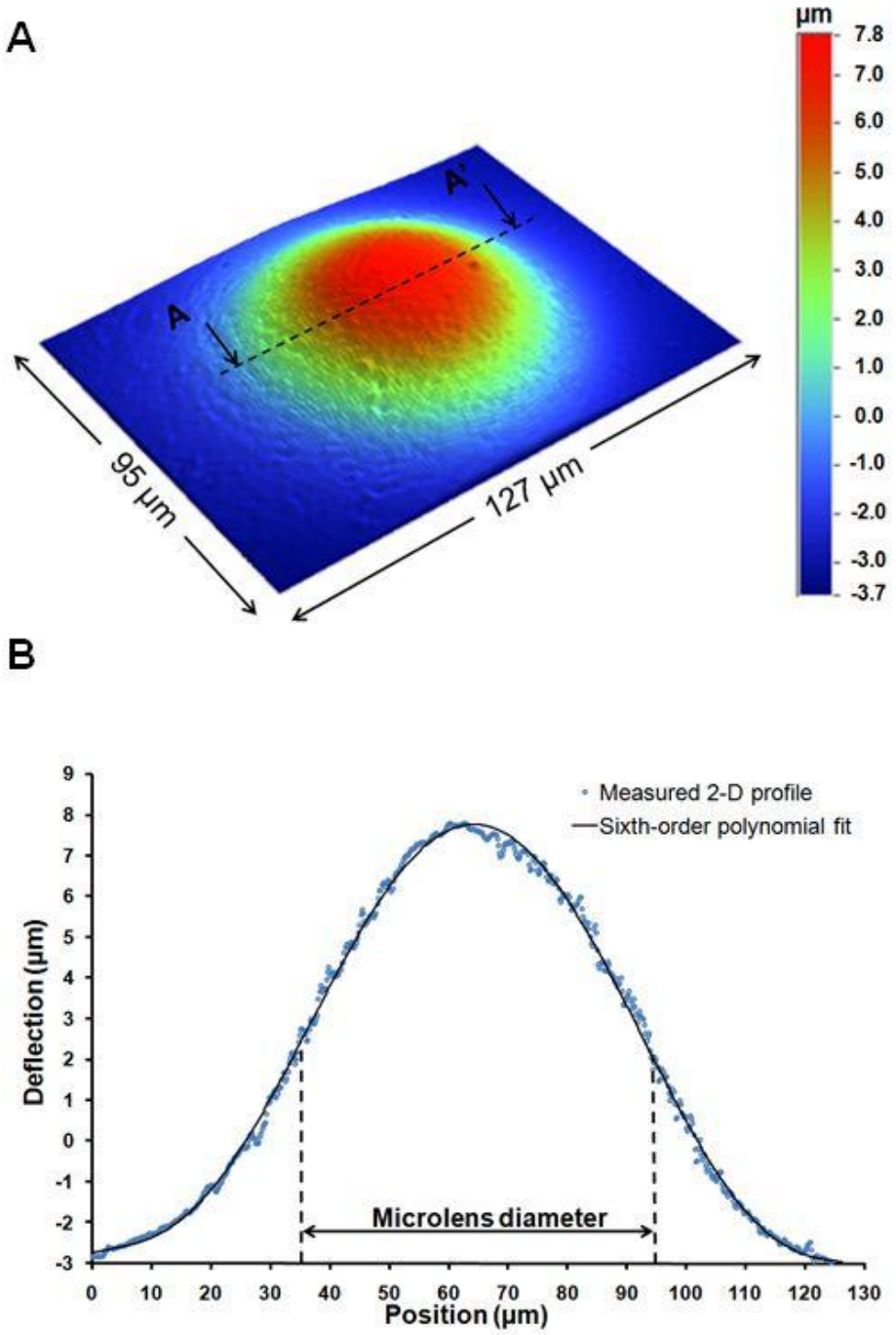

Figure 4.6: (A) Surface profile of a 60 μm diameter microlens (cured at 30 psi) obtained using a white light interferometer. **(B)** A 2D microlens profile measured along its midline (cross section A-A' in A). The profile has been curve fitted with a sixth order polynomial.

The depth of focus and the transverse resolution of such a microlens (60 μm diameter solid microlens, cured at 30 psi) were calculated by measuring its axial intensity profile and point spread function (PSF) respectively (**Figure 4.7**). To obtain the axial intensity profile, we extracted the maximum intensity from imaging planes above and below the best focused plane in an optical setup similar to the one used for obtaining the EFL. The theoretical value of the depth of focus (DOF) was estimated to be ~6 μm [95]. Within that distance, the maximum intensity dropped by 5%. To obtain the PSF of the microlens, we measured the background-corrected in-plane intensity distribution ($I[x,y]-I_0$) at the best-focused plane and normalized that value by the background intensity (I_0). The transverse resolution of the microlens, defined as the full width at half maximum (FWHM) of the PSF [96], was found to be 2.8 μm.

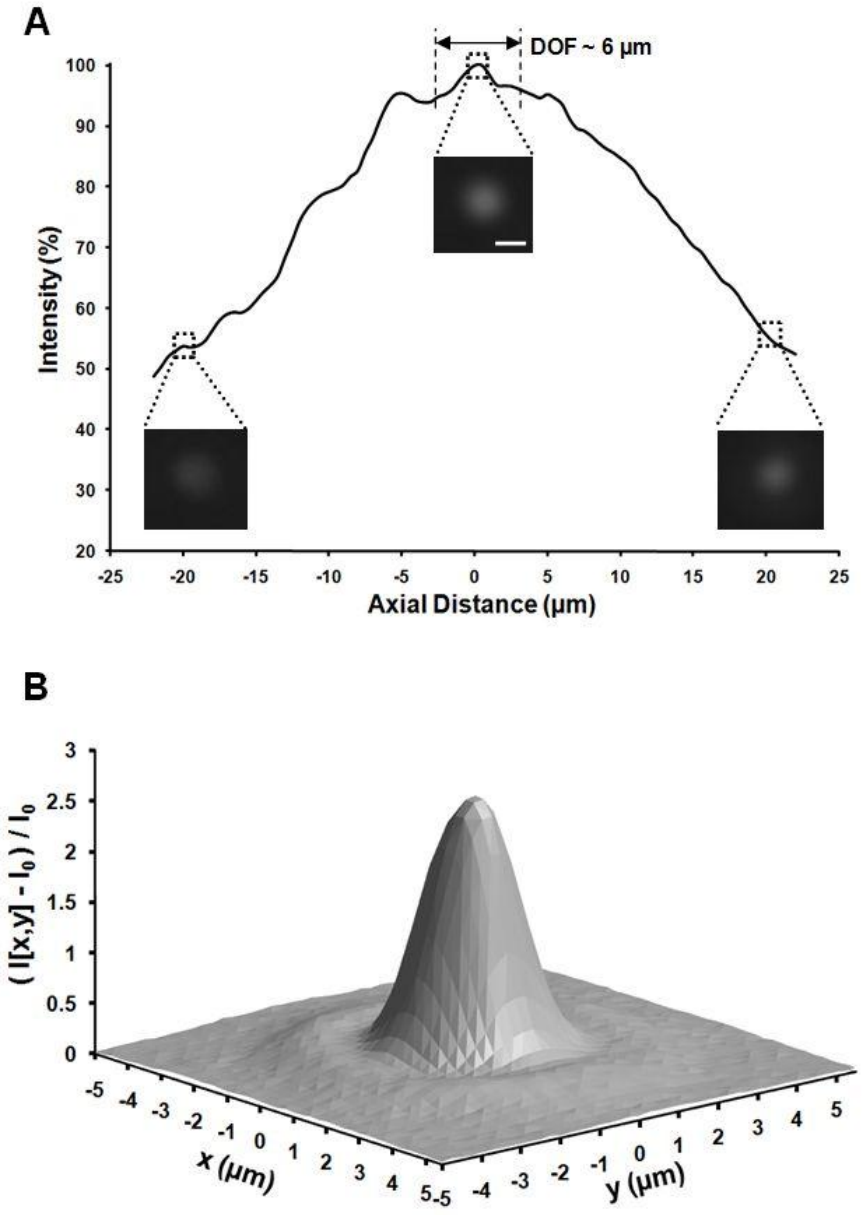

Figure 4.7: (A) Relative intensity (maximum intensity for a given axial plane normalized with the maximum intensity measured at the best focused plane) along the optical axis of a 60 µm diameter microlens as a function of the distance from the best-focused plane. The pictures depict the focused laser beam as imaged at the focal plane and at two out-of focus planes. Scale bar, 10 µm. **(B)** The PSF of the same microlens represented as the in-plane intensity distribution ($I[x,y] - I_0$) at the best-focused plane, normalized with respect to the background intensity I_0.

Finally, we demonstrated that it is possible to use the fabricated microlenses to magnify and image micron-size resolution features patterned on a chrome mask (**Figure 4.8**). 3 µm wide line features were clearly visible after placing the microlens device between the chrome mask and a 1x microscope objective (we used Olympus SZX16 stereo microscope). Minimum distortion was observed at the center region of the microlens.

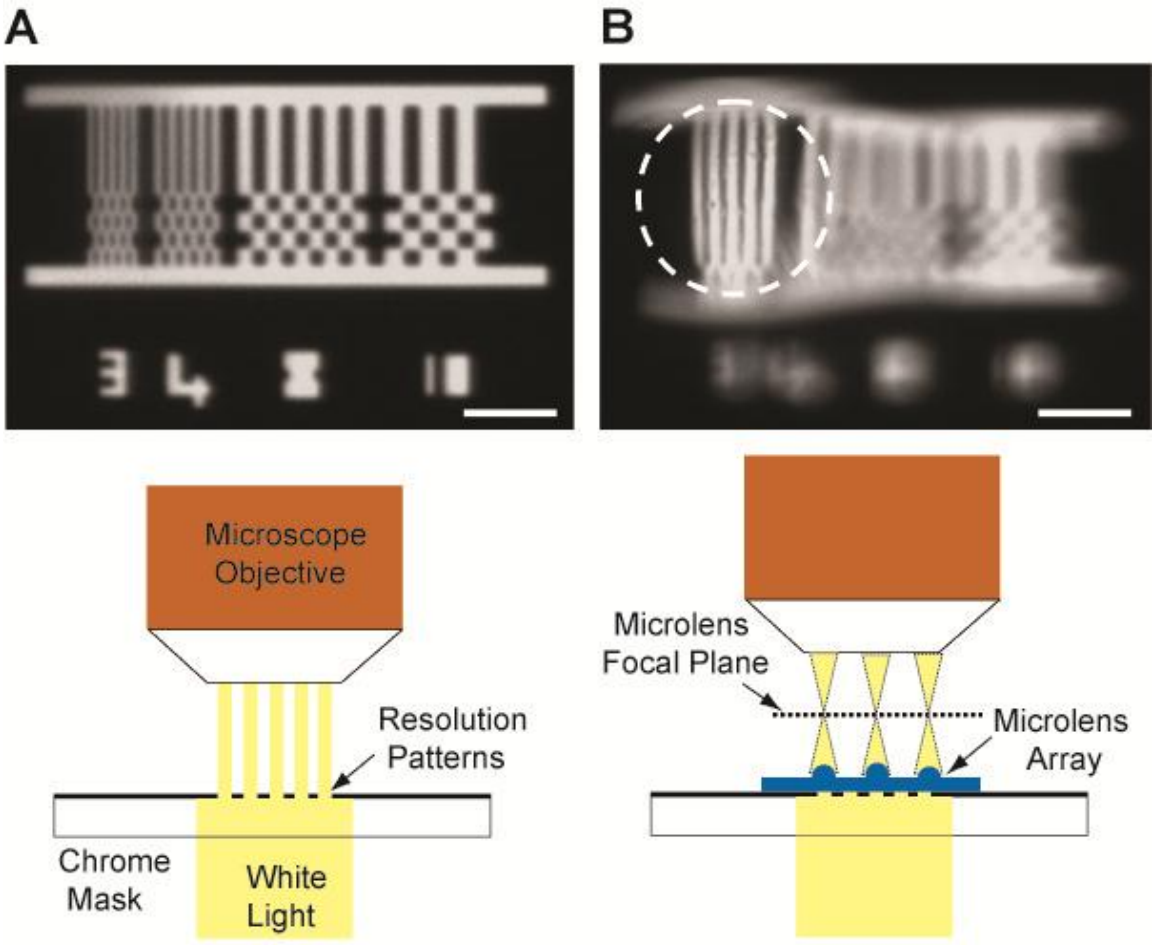

Figure 4.8: Micron-size resolution patterns imaged: **(A)** without using a microlens, and **(B)** through a 60 µm diameter microlens (NA ~ 0.3). Equally-spaced, 3 µm wide lines are magnified by a factor of ~2 and are clearly visible. Scale bar, 50 µm (A) and 25 µm (B).

4.4 Conclusions

In this chapter, we demonstrate a novel microfabrication process for obtaining polymer-based, planar microlens arrays. The microlens array comprises of polymer-filled circular microchambers enclosed by deformable, elastomeric membranes. Each microchamber is transformed into a solid microlens when the UV-curable polymer is pressurized and cured. By varying the curing pressure (7.5-30 psi), microlenses with a wide range of EFL (100-400 μm) and NA (0.05-0.3) have been fabricated from 40 μm and 60 μm diameter membranes. We have obtained a NA of 0.3 and transverse resolution of 2.8 μm for 60 μm diameter microlenses (cured at 30 psi). Smaller diameter (40 μm) microlenses have lower NA than larger diameter (60 μm) microlenses for similar curing conditions. The proposed microlens design is compatible with a wide variety of curable polymers and therefore it can be used to obtain microlenses with different optical properties. We envision the use of these planar microlenses in lab-on-chip detection systems for imaging micron-sized biological specimens. These microlenses can be integrated with the cell trapping biochips (such as the one in chapter 3) for obtaining compact and portable cell imaging and counting systems.

CHAPTER 5

A High Numerical Aperture Doublet Microlens Array

This chapter presents a high numerical aperture, doublet microlens array for imaging micron-sized objects. The proposed doublet architecture consists of glass microspheres trapped on a predefined array of silicon microholes and covered with a thin polymer layer. A standard silicon microfabrication process and a novel fluidic assembly technique were combined to obtain an array of 56 μm in diameter microlenses with a numerical aperture (NA) of ~0.5. This NA value was a significant improvement over the 0.3 NA polymer-based microlenses presented in chapter 4 and hence these microlenses are better suited for high resolution imaging of cells and tissues. Using the doublet microlens array, we demonstrated brightfield and fluorescent image formation of microobjects directly on a CCD sensor without the use of intermediate lenses. The proposed microlens fabrication technology is a significant advancement towards the unmet need of inexpensive, miniaturized optical modules, which can be further integrated with lab-on-chip microfluidic devices and photonic chips for a variety of high-end imaging/detection applications. In particular, these microlenses arrays can be integrated with the WBC capture biochip presented in chapter 3 for fluorescence based imaging and counting of WBCs.

5.1 Introduction

Modern optical imaging-based research and industrial systems rely on the use of bulky and expensive objectives lenses. Despite their superior performance in resolving submicron features under low-light conditions, these lenses can detect only one sample at a time (that lies within their field of view (FOV)), while manufacturing limitations do not allow miniaturization and integration with emerging micromachined devices, including miniature CCD sensors [97], photonic chips [98] and microfluidic biochips [99]. The development of on-chip lens-based optical modules entails the miniaturization of these lenses while maintaining superb imaging quality. Such miniaturized, typically microfabricated lenses (also known as 'microlenses') can be used in displays [75, 100, 101], for optical coupling [102-104] and surface microstructuring [105] as well as in various biomedical imaging applications [106-108].

A number of microlens microfabrication approaches have been proposed over the past three decades. Photoresist reflow and transfer methods are the earliest methods for fabricating microlenses [35, 83, 109]. These microlenses have a low light collecting capability (indicated by a low numerical aperture (NA)) and are unable to form a resolved image of weakly light-emitting micron-sized objects. A modified approach called the 'boundary confined method' has been proposed to obtain high NA (NA~0.54) microlenses [110]. Similar to other photoresist reflow approaches, this method requires accurate control of the surface tension of the photoresist-substrate interface. Ink-jet printing of UV-curable polymers has been another approach for fabricating microlens arrays [37, 38]. This method requires an expensive setup for accurately dispensing a

polymer on a rigid substrate. Recently, fabrication of high NA (NA~0.37) microlens arrays using ink-jet printing of UV-curable polymers on hydrophobic glass substrates has been reported [111]. These processes require an elaborate control of the material properties (viscosity, surface tension) of the polymer as well as of the hydrophobicity of the substrate surface. Microfabrication of high NA microlenses has also been proposed using focused ion beam milling and femtosecond laser direct writing technologies [39, 40]. These microfabrication processes are serial processes and require expensive equipments and experienced personnel. Soft lithography-based approaches in which optical materials are molded against rigid and elastomeric molds to obtain microlenses have also been demonstrated [41, 42]. These methods are simple to implement but the microlens quality is strongly dependent on the surface finish of the mold. Alternatively, planar, polymer-based arrays of microlenses can be microfabricated by UV-assisted curing of microfluidic networks [112]. These planar microlenses have a relatively high NA (NA~0.3) when compared to other planar microlenses but are not amenable to an easy integration with other optical and microfluidic devices.

High NA (NA~0.64) spherical microlenses have also been microfabricated by injecting SU-8 photoresist through microfabricated nozzles and utilizing surface tension to form micro-balls [113]. These microlenses largely vary in size due to fluctuations in the injection pressure and the contact angle between the photoresist and the substrate. Another process for spherical microlens fabrication involves polymer molding against isotropically etched silicon master molds [44]. The surface quality of the mold is highly dependent upon the precise balance of reagents used to etch the master mold. Finally, a

number of high NA, spherical microlens fabrication approaches employing the use of glass or polystyrene microspheres have been proposed [114, 115]. However, none of these microlenses have been shown to form the image on their own on an imaging sensor without the aid of additional optical elements. Several microlenses have been proposed for amplifying the light signal on the imaging sensor, hence increasing the effective numerical aperture of the imaging system [116-121]. However, all these approaches involve the use of macroscopic lenses in addition to the microlens arrays for image formation on the imaging sensor.

We propose a novel microfabrication approach for obtaining low-cost, high-NA arrays of doublet microlenses for imaging micron-sized objects without the need of any additional lenses. These microlenses are made out of glass microspheres with a transparent polymer spun on them. Planarizing one side of the microlenses with a transparent polymer layer enables an easy integration of the microlens array with microfluidic lab-on-chip devices and other photonic chips. The microlenses array is microfabricated using a combination of silicon micromachining, soft lithography and fluidic assembly. To our knowledge, this is the first demonstration of magnified image formation on a CCD sensor using a microlens array without use of intermediate lenses. An array of these doublet microlenses has the following advantages: i) equivalent optical performance (resolution, NA) to a conventional microscope objective, ii) simultaneous imaging of a large number of objects, iii) easy integration with other micromachined modules, including microfluidic and optical chips, iv) direct image formation on an imaging sensor without any extra lenses and v) low microfabrication cost. This microlens

fabrication approach not only provides higher NA (0.5) microlenses as compared to the 0.3 NA planar polymer-based microlenses presented in chapter 4 but also enables direct image formation on an imaging sensor (not possible with the planar microlenses owing to a thick PDMS support layer). With these advantages, we believe that the doublet microlens arrays can be readily integrated with the WBC capture biochip presented in chapter 3 to develop a point-of-care WBC counting biochip.

5.2 Design and Microfabrication of the Doublet Microlens Array

The proposed doublet microlens array consists of glass microspheres, fluidically assembled on top of an array of wafer-through microholes (**Figure 5.1**). The microhole array captures/places the microspheres in a predefined pattern, while it creates a clear optical path for the collected light to reach the imaging sensor. The microlens array collects light originating from micron-sized objects and forms an image of these objects on the imaging sensor. It is intended to function as a magnifying lens: objects placed at a plane slightly below the focal plane of the microlens array, appear magnified at the imaging sensor. To ensure that the magnified image is in focus on the plane of the sensor the sensor's spatial position has to be adjusted in the vertical direction using a translational manipulator.

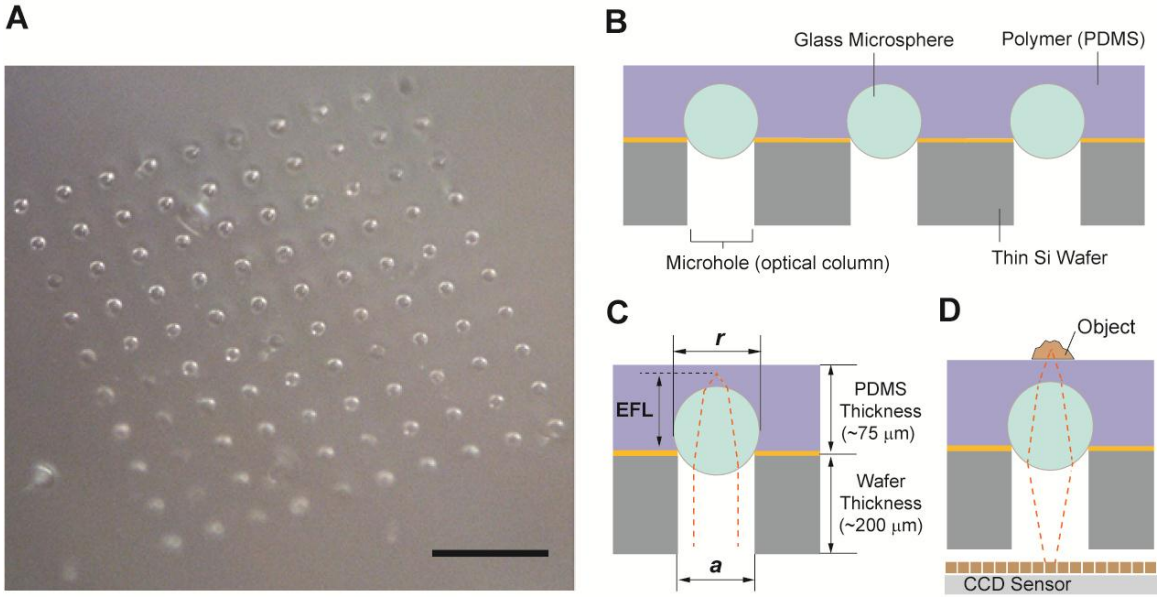

Figure 5.1: (A) A 10x10 array of 56 μm in diameter doublet microlenses. Scale bar, 500 μm. **(B)** A schematic of the cross section of the microlenses array. The microlens diameter is defined by the diameter of the microhole. **(C)** A collimated light beam is focused at a point (focal point) right below the top surface of the PDMS layer. The distance between the focal point and the silicon dioxide surface is the microlens effective focal length (EFL). *a* is the microhole (microlens) diameter and *r* is the microsphere diameter. **(D)** Mechanism of image formation using the doublet microlens array. The object is placed on the surface of the microlens. A magnified image is formed directly on a CCD sensor.

The microfabrication of the doublet microlens array involves three steps (**Figure 5.2**): i) microfabrication of the microhole array, ii) assembly of glass microspheres on the array, and iii) spinning of a polymer layer on the captured microspheres to form the doublet microlenses. Specifically, a 2 μm thick PECVD silicon dioxide is initially deposited on a ~500 μm thick silicon substrate. An array of 56 μm diameter microholes is then patterned and etched on the oxide layer using standard photolithography and reactive ion etching (RIE). Deep reactive ion etching (DRIE) is further employed to fabricate wafer-through circular microholes in the silicon substrate. Subsequently, the silicon substrate is thinned down to 200 μm using a combination of lapping and chemical-

mechanical polishing (CMP). An aqueous solution containing glass microspheres (60 μm nominal diameter, refractive index 1.51 at a wavelength of 589 nm; catalog no. 02718-AB, Structure Probe, Inc.) is then dispensed on the oxide-coated silicon surface. A suction force is subsequently applied from the other side of the substrate to assemble and trap the glass microspheres atop of the microhole array. Doublet microlenses are finally obtained by spinning and curing (65ºC, 1 hour on a hot plate) a ~75 μm thick (spun at 1600 rpm) layer of polydimethylsiloxane (PDMS) elastomer on top of the array.

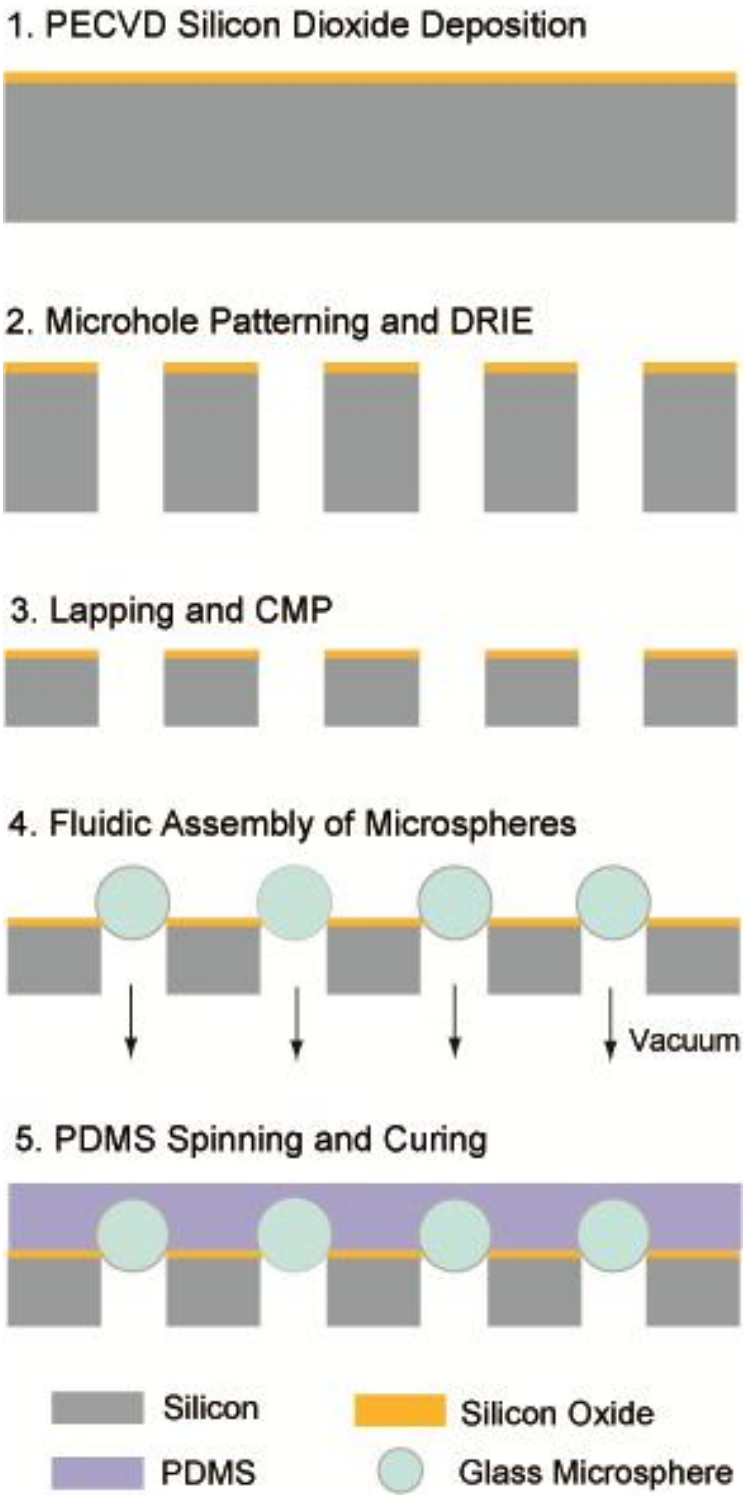

Figure 5.2: Microfabrication process of the doublet microlens array. Key concept is the fluidic assembly of glass microspheres (step 4).

5.3 Results and Discussion

We performed optical simulations using OSLO software to ascertain the effective focal length (EFL) of the fabricated microlenses (for all simulations, we assumed a wavelength of 580 nm). We defined the microlens EFL as the distance between the best focused plane of a collimated light beam passing through a doublet microlens and the silicon dioxide-coated wafer surface (Figure 5.1C). A refractive index of 1.41 and 1.51 was used for the PDMS and the glass microspheres respectively. EFL values of 65-75 μm were obtained for glass microspheres ranging 57-63 μm in diameter. Experimental EFL values were obtained for individual microlenses in the array using a collimated white light (see [112] for details on the experimental setup used to measure the EFL). The EFL measurement process involved obtaining the best focused plane by capturing a stack of images along the microlens axis and finding the plane with the maximum light intensity. A 40X (0.6NA) microscope objective was used to image the best focused plane. EFL values measured for 20 microlenses in the microlens array varied from 63 to 71 μm. These values correlated strongly with the EFL range obtained from optical simulations. Such a variation on the measured EFL between microlenses can be attributed to variations of the microsphere diameter (5%, given by the manufacturer). We also performed optical simulations to assess the dependence of the EFL on the PDMS curing conditions (temperature, time) as those are known to affect the PDMS refractive index [122]. For two extreme curing cases (48 hours at 25ºC and 1 hour at 150ºC), the EFL was found to change by less than 1 μm (assuming a change in the PDMS refractive index from 1.416 to 1.472 [122]). These results show that the EFL of our microlenses is not significantly affected by the PDMS curing conditions.

Furthermore, we used optical simulations to estimate the NA of the doublet microlenses as a function of microhole diameter (*a*) to microsphere diameter (*r*) ratio (figure 3). For our fabricated microlenses (*a* = 56 μm, *r* = 60 μm, *a/r* = 0.93), a NA of 0.495 was obtained. This NA value is very close to the maximum theoretical NA value (0.53, *a/r* = 1.0) achievable using this microfabrication method. It should be emphasized that objectives with a NA of 0.35-0.4 are commonly used in microscopy for imaging cells and tissues [123].

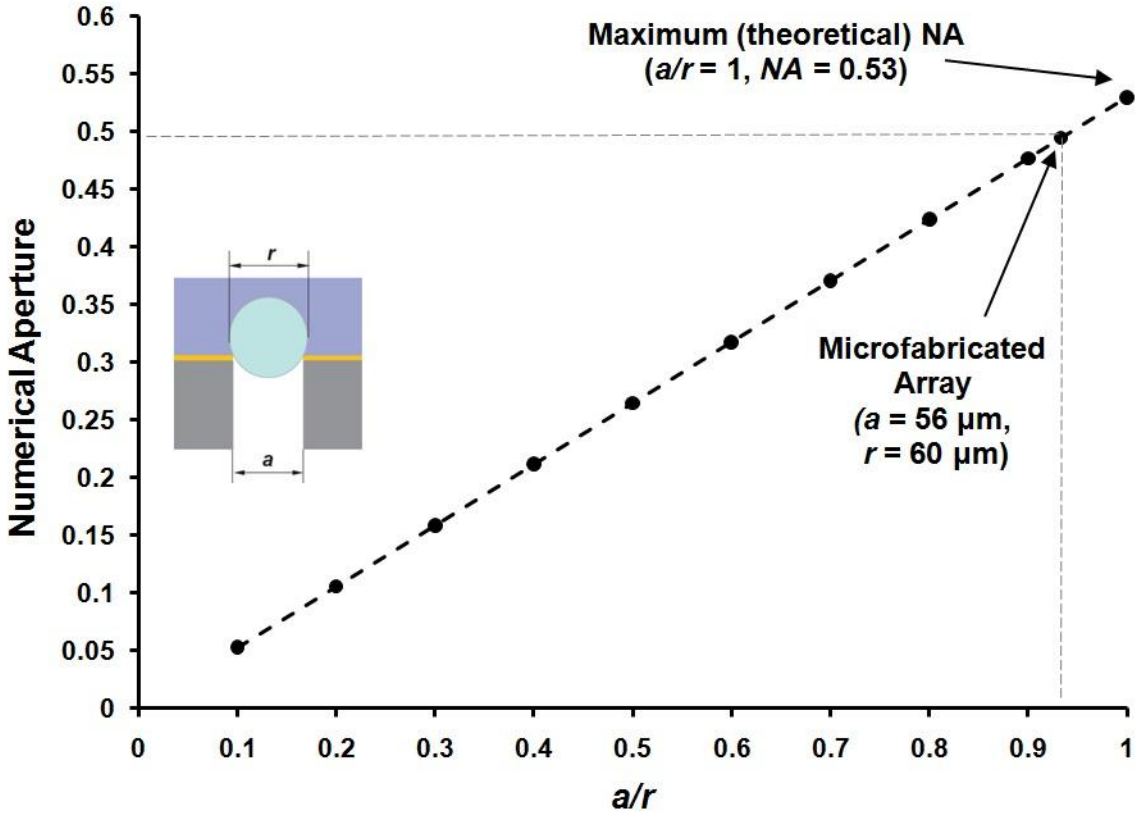

Figure 5.3: Simulation results depicting the dependence of the numerical aperture (NA) on the microhole to microsphere diameter ratio (*a/r*). A NA value of 0.495 was estimated for our microfabricated microlenses.

To measure the depth of focus (DOF) of the doublet microlenses, we obtained the axial light intensity profile of a collimated light beam that was focused through the microlens array (**Figure 5.4**). The collimated light beam was generated by placing a point source of light (a halogen lamp) 25-30 cm away from the microlens array. The average light intensity was obtained for imaging planes above and below the best focused plane (the focal plane) and normalized with respect to the average light intensity at the best focused plane (that corresponded to the maximum average intensity). Intensity values for all imaging planes were background-corrected. The DOF of the fabricated doublet microlenses (a/r = 0.93, NA~0.495) was estimated to be ~3.6 μm [95]. Within this distance, the average light intensity decreased by 2% from its maximum value (at the best focused plane).

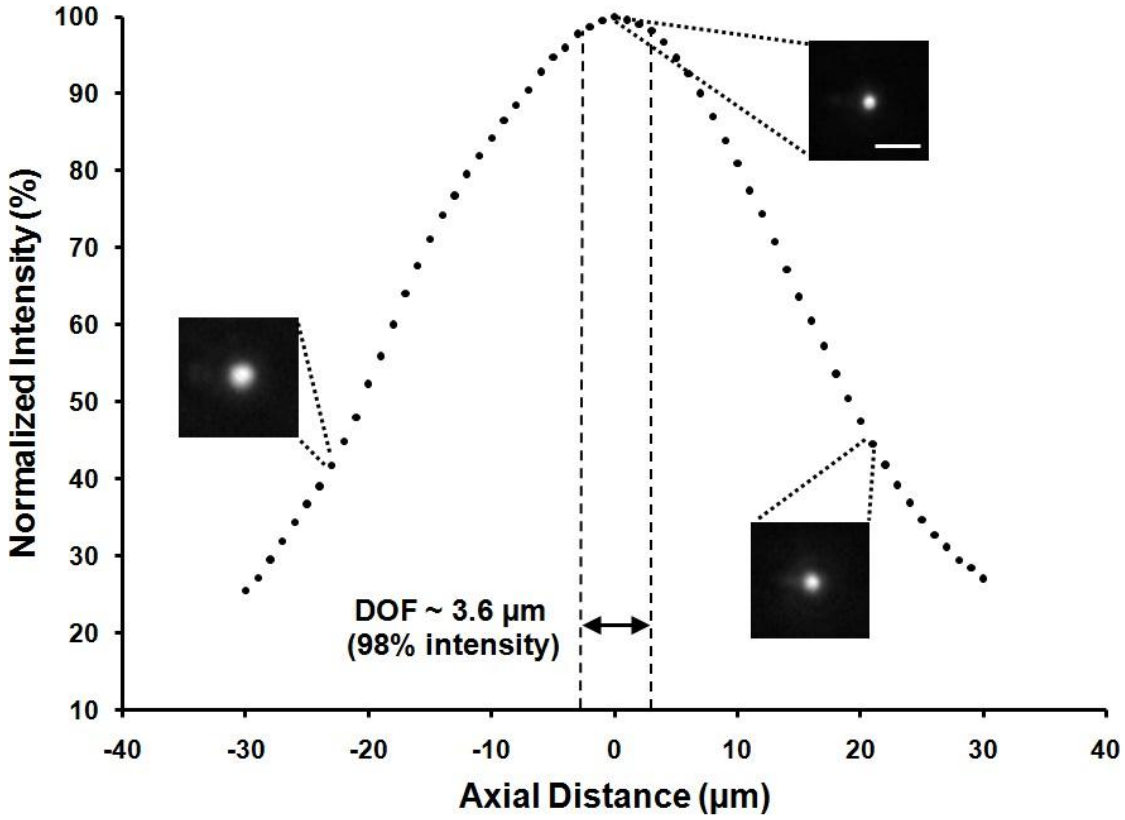

Figure 5.4: Normalized intensity (with respect to the background corrected average intensity at the best focused plane) of a doublet microlens as a function of the axial distance from the best focused plane. The images depict a focused light beam at different axial planes. Scale bar, 10μm.

Low (4X) and high (40X) magnification measurements were taken from a 4x4 microlens array and from a single microlens respectively to obtain the point spread function (PSF) (**Figure 5.5**). The 4x4 array had 16 spatially distinguishable intensity peaks (**Figure 5.5A**), observed at the center of each microlens. The average value of the normalized intensity from those 16 peaks was 82.3% (standard deviation 19.6%), ranging from 44% to 100% between individual microlenses. This non-uniformity in the peak values can be attributed to the EFL variation discussed earlier in this section.

A

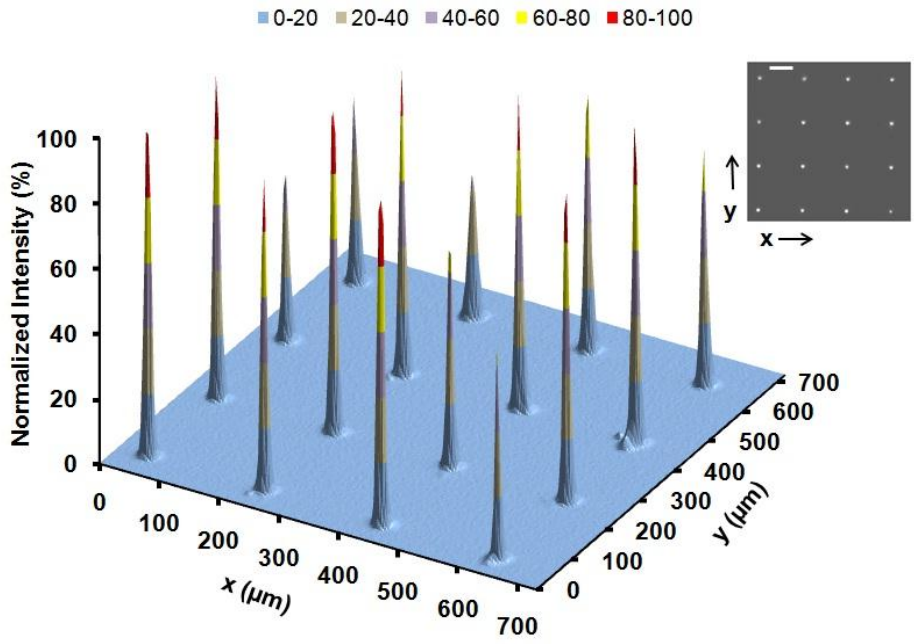

B

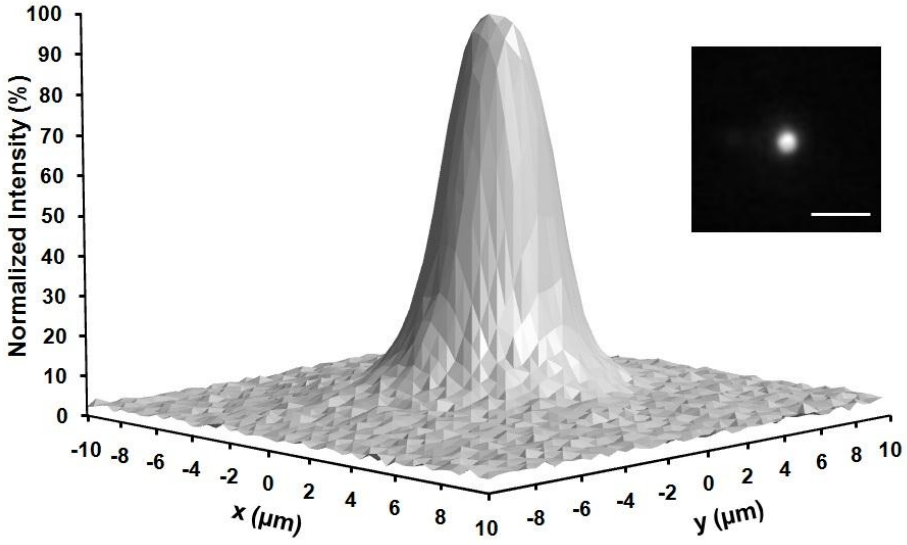

Figure 5.5: (A) PSF of a 4x4 microlens array. Scale bar of the image: 100 μm. **(B)** PSF of an individual microlens. Scale bar of the image: 10 μm. (A) and (B) plots were obtained using a 4X (NA=0.15) and a 40X (NA=0.6) microscope objective respectively. In both (A) and (B), normalized intensity values at a particular xy point were obtained by normalizing the background-corrected light intensity at that point with the maximum value in the entire image.

As described above, a major advantage of the proposed microlens array is their capability to form an image directly on an imaging sensor without intermediate lenses. To demonstrate the image formation capability and magnification achieved using these microlenses, we used a microlens array to image resolution patterns etched on a chrome layer, deposited on a glass substrate (**Figure 5.6**). A 640x480 CCD sensor chip (5.6 μm pixel size), dismantled from a web camera (Logitech QuickCam 3000) and a custom experimental setup utilizing x-, y- and z-axis manipulators, were used to acquire images and to align the patterns-microlens assembly with the imaging sensor chip (**Figure 5.6A**). A white light source was used to illuminate the resolution patterns. In this brightfield, transmission imaging mode, the microlens array was able to resolve various 1 μm and 2 μm resolution patterns (**Figure 5.6B(I)-(III)**). The theoretical resolution was calculated to be 0.45 – 0.71 μm (for a 450-700 nm wavelength) [95].

We also demonstrated the use of these microlenses for fluorescent imaging of micron-size objects. We obtained a magnified, fluorescent image of 4 μm in diameter polystyrene bead (excitation peak 505 nm, emission peak 515 nm, catalog no. F-8859, Invitrogen, Inc.) using a slightly modified setup for fluorescence imaging (**Figure 5.6B(IV)**). The fluorescent beads were illuminated with a blue light obtained after passing white light (originated by a halogen lamp) through an optical band-pass filter (XF1073 475AF40; Omega Optical). A thin (~100 μm) long-pass emission filter (Yellow 12 Kodak Wratten colour filter) was inserted between the microlens array and the CCD sensor to block the excitation light. The fluorescent image obtained for the bead was magnified by a factor of ~6. At this 6X magnification, a 56 μm diameter microlens (with

a 60 μm microsphere) is estimated to have a field of view (FOV) of ~9.3 μm (FOV = microhole diameter/magnification). The dimensions of the objects used for brightfield and fluorescence imaging correspond to an average cell diameter (e.g. blood cell) and hence the above imaging results validate the potential use of these microlenses for imaging biological micron-size objects (cells, tissues etc.) directly on a CCD sensor.

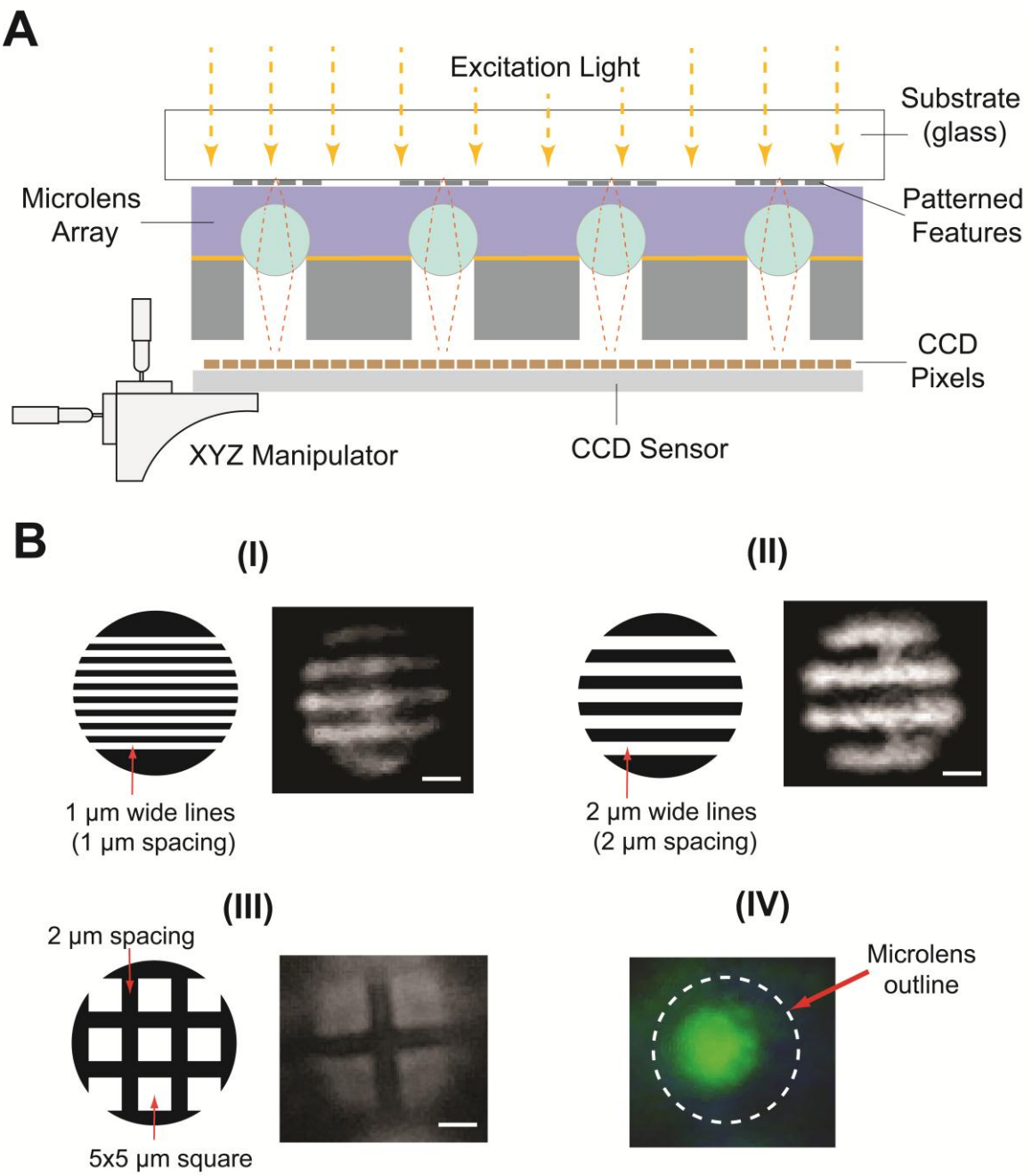

Figure 5.6: (A) Schematic of the setup for imaging micron-size resolution patterns using the doublet microlenses array. **(B)** (I) & (II) Brightfield, transmission images of 1 and 2 µm line resolution patterns respectively using a 56 µm diameter microlens (NA~0.495). Equally spaced, 1 µm wide lines are clearly resolved by the doublet microlens. Scale bar, 20 µm. (III) Brightfield, transmission image of a 5 µm square grid. Scale bar, 20 µm. (IV) Fluorescence image of a polystyrene bead (4 µm in diameter).

5.4 Conclusions

In this chapter, we have presented a novel doublet microlens array microfabrication approach for the direct visualization of micron-sized objects. Using these microlenses, we have demonstrated direct image formation on a CCD sensor without additional optical elements. These microlenses resolved 1 μm resolution patterns and had a numerical aperture of ~0.495. As a result, they can be considered as miniaturized microscope objectives and they provide a cheaper alternative for bulky and expensive microscope optics. They can readily find biomedical applications in imaging of cellular and subcellular components. Owing to their superior optical performance and ease of fabrication over the planar polymer-based microlens arrays, these microlenses provide a better option for integration with the WBC capture biochip. The integrated biochip will enable on-chip fluorescence imaging and counting of WBCs.

CHAPTER 6

Conclusions and Future Work

6.1 Conclusions

White blood cells (WBCs) and their subtypes are indicators of the state of the human immune system. WBC count (total as well as differential) in human blood is, therefore, an important metric for diagnosis of a number of immunological diseases. Flow cytometry based instruments which have been used conventionally for WBC counting are bulky, resource intensive and not amenable for use at the point-of-care. Microfluidic lab-on-chip technology with its unique features can be employed for developing miniaturized WBC counting systems. These features include: i) low sample and reagent requirements, ii) less power requirements, iii) precise and controlled delivery of sample and reagent volumes, iv) small size of the devices which are inexpensive and disposable, v) ease of operation and maintenance, vi) possible integration of the individual modules for cell capture, imaging and counting respectively, on a single platform and vii) fast and sensitive results owing to small sample volumes. Taking advantages of these features of the microfluidic lab-on-chip technology, we have envisioned a WBC counting system which will capture WBCs from human blood and simultaneously image and count them. In this thesis, we have developed individual modules which i) can capture WBCs and ii) can be used for imaging and counting WBCs. The important contributions of this thesis can be summed up as the following:

6.1.1 Microfluidic biochip with a 3D architecture for capturing WBCs

Size based capture of WBCs is a commonly employed method of isolating WBCs from other blood components (RBCs and platelets). This method relies upon the bigger size of WBCs as compared to RBCs and platelets. A number of microfluidic approaches utilize membrane filters (with microholes) for capturing WBCs in a flow while allowing the RBCs and platelets to squeeze through [26, 27]. Although simple to fabricate and operate, these microfluidic devices have low (< 80%) WBC trapping efficiency. This can be attributed to the 2 dimensional confinement of WBCs in the filter holes (no constraint in the third dimension), hence allowing them to squeeze through and resulting into a lower trapping efficiency. To overcome this drawback of membrane filter based microdevices, we have developed a microfluidic biochip with a novel 3D cell trapping architecture for capturing WBCs.

The biochip incorporates a membrane with an array of photolithographically patterned microholes, sandwiched between two microfluidic networks. The WBCs flowing through the biochip are confined in the 3D space created by the microholes and the bottom microfluidic network resulting into a more efficient trapping. A high (>87%) WBC trapping efficiency was obtained using the biochip when WBCs suspended in a buffer solution were flown through the device at 3 psi injection pressure. The biochip design has been optimized to ensure equal cell trapping probability in all the regions of the biochip. The biochip has the flexibility of operation in both push (pressure) as well as pull (suction) mode. We envision that the biochip with its novel cell trapping design can not only be used for separating WBCs from other blood components but also for the size

based separation of other cells (e.g. circulating tumor cells) from biological samples (blood, urine, saliva etc.).

6.1.2 High numerical aperture microlens arrays for imaging micro-objects

Microscope objective lenses with a high light collection capability (high numerical aperture NA) are usually employed for high resolution imaging of biological micro-objects (cells, tissues etc.). However these objective lenses are bulky, expensive, have a small field-of-view and hence are not suitable for integration with microdevices manipulating cell and tissue samples. This limitation of conventional objective lenses necessitates the development of inexpensive microlenses that have an equivalent optical performance (NA, magnification) as the macroscale lenses and which can be easily integrated with the lab-on-chip microfluidic devices. To meet this requirement, we have developed two microfabrication techniques for obtaining high NA microlens arrays.

- **Planar, polymer-based microlens array using soft lithography**

This microlens array fabrication approach involves deflection of an elastomeric membrane integrated on the top of polymer-filled circular microchambers. Upon the application of pressure to the UV-curable polymer in the microchambers which is simultaneously cured by exposure to UV radiations, each membrane/microchamber assembly transforms into fixed focal length microlens. Large membrane deflection achievable by the use of an elastomeric material results into microlens with a highly curved surface profile. These microlenses have a high light collecting ability reflected in their high NA (~0.3) values. This microfabrication technique enables fabrication of

microlenses with a wide range of focal lengths and numerical apertures by varying the elastomeric membrane thickness, lens filling polymer and the applied pneumatic pressure.

- **Doublet microlens array using fluidic assembly of microspheres**

This microlens fabrication approach involves assembling glass microspheres on an array of silicon microholes using a novel fluidic assembly technique. The fabrication is complete by spinning a thin layer of transparent polymer on one side of the microspheres to planarize the microlens surface. A planar microlens surface enables an easy integration with other lab-on-chip microdevices. High NA (0.5) microlenses were obtained using this microfabrication technique. Using microspheres with varying refractive indices, doublet microlenses with a wide range of numerical apertures can be obtained. The doublet microlenses have been demonstrated to be capable of imaging 1 μm resolution patterns directly on a CCD sensor without the any additional optical elements. Thus, they provide a cheaper alternative to more bulky and expensive microscope objective lenses and can be used for the development of new generation of miniaturized microscopes for biomedical applications.

The two microlens arrays discussed in this thesis have an inexpensive fabrication process which can be scaled up to obtain 100s and 1000s of microlenses on a single substrate. With their high NAs (0.3-0.5), these microlens arrays can enable large field-of-view high resolution imaging of micron-sized objects.

6.2 Future Work

We envision that the work presented in this thesis can be extended in the following research directions:

6.2.1 Cell trapping biochip with an integrated volume metering and RBC lysis chamber

The WBC capture performance of the biochip proposed in this thesis has been demonstrated using buffer suspended WBCs obtained after lysing RBCs from 1 μl of whole blood. In order to more accurately determine the WBC trapping efficiency of the biochip, we would essentially be required to count the WBCs in a given volume (e.g. 1 μl) of whole blood before the blood enters the cell trapping region of the biochip. To achieve this functionality, we envision a cell trapping biochip with an integrated volume metering chamber (**Figure 6.1**). The metering chamber will not only ensure the injection of a fixed volume of blood in the cell trapping region but will also provide a window for imaging the blood cells before their entry in the cell trapping region. Hydrophobic valves which have been employed for flow control in microfluidic devices will also be incorporated in this device design [124-126]. These valves will help to control the flow of blood and buffer during the biochip operation. A hydrophobic pad patterned in the connecting narrow channel between the metering chamber and the cell trapping region will help to stop the flow of blood unless a higher pressure is applied to overcome the pressure barrier across the hydrophobic pad. A similar hydrophobic pad patterned at the buffer inlet will prevent the blood from entering the buffer channel.

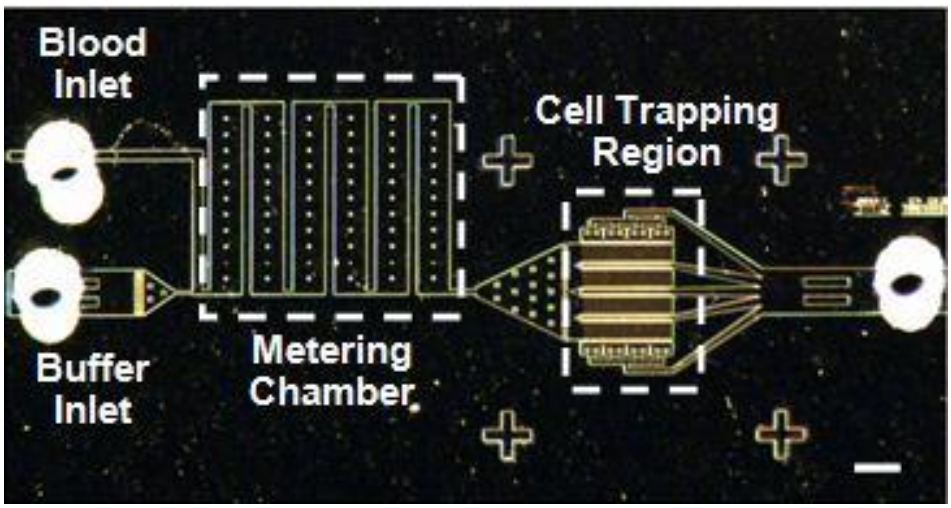

Figure 6.1: Snapshot of the first prototype of a cell trapping biochip with an integrated volume metering chamber. The metering chamber of this prototype has a total volume of 0.1 μl. Scale bar, 500 μm.

The integrated biochip will work in the following manner: The fluorescently tagged whole blood is injected into the biochip through one of the inlets and the flow stops at the hydrophobic pad (at the metering chamber-cell trapping region interface). A fixed volume of blood fills up the metering chamber. WBCs are then imaged and counted in the metering chamber. This is followed by the injection of PBS solution through another inlet under pneumatic pressure. This pressure overcomes the pressure barrier across the hydrophobic pad and pushes the blood cells into the trapping region where WBCs are trapped and imaged. The WBC trapping efficiency (η) of the biochip will be given by:

$$\eta = \frac{\#\text{ of trapped WBCs}}{\#\text{ of WBCs in the metering chamber}}$$

Off-chip lysis of RBCs from whole blood involves a number of mixing and centrifuging steps. A large number of WBCs also get destroyed during the lysis process.

To avoid this WBC loss, some on-chip RBC lysis techniques have been proposed which completely eliminate centrifuging and vigorous mixing steps resulting into negligible WBC loss [69, 127]. We envision a modified form of the above biochip in which the metering chamber will be pre-functionalized with a detergent (e.g. Tween 20) during the fabrication process. This detergent will serve the purpose of lysing RBCs from the whole blood. A passive mixer will also be incorporated in the design of the metering chamber to ensure that the entire blood volume comes in contact with the detergent resulting into the destruction of most of the RBCs [128]. We believe that this integrated design will enable a more accurate measurement of the biochip WBC trapping efficiency. With the optimization of this biochip design, this can develop into a device for obtaining an accurate WBC count from human whole blood.

6.2.2 Microfluidic-based oil immersion lens array

Oil-immersion objective lenses are employed for high resolution imaging applications. Immersion oil whose refractive index matches with that of the objective lens material increases the light collecting ability (and the NA) of the lens. With the aim to obtain high NA (~0.7-0.8) microlenses, we envision a variation of the doublet microlenses which incorporates high index of refraction oil-immersed ball lenses. High index of refraction microspheres will provide a higher NA than that obtained using the doublet microlenses (NA ~ 0.5) proposed in this thesis.

The proposed microlens array will consist of sapphire ball lenses (refractive index 1.77) integrated on the top of an array of immersion oil-filled microchambers (**Figure**

6.2). The oil/ball lens assembly will act as a high NA (~0.8) doublet lens and can be used for high resolution imaging of biological micro-objects.

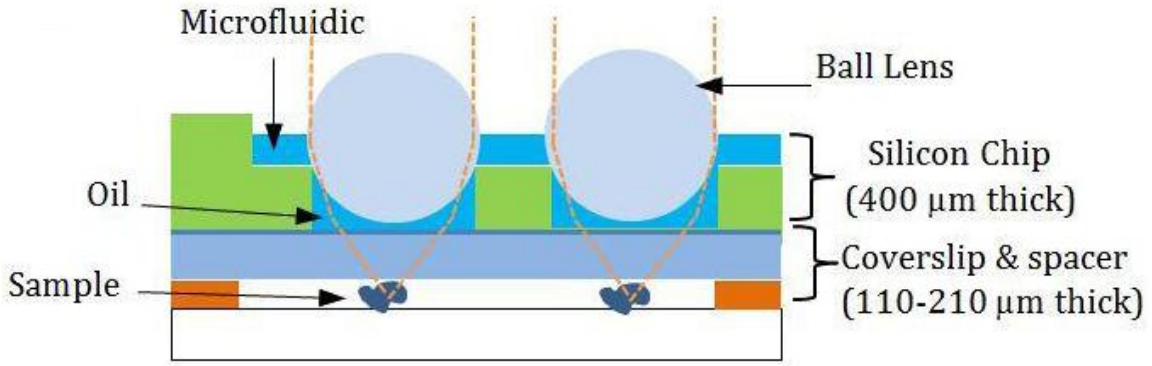

Figure 6.2: Cross sectional view of the proposed oil-immersion microlens array. A glass coverslip and a spacer will accurately define the distance between the lens and the sample object.

We envision that the oil-immersion lens array can be used as an add-on module on low cost stereoscopes to enable high resolution, wide field of view imaging of biological samples in the lab, in the doctor's office or in the field.

6.2.3 Integrated biochip for on-chip capture, imaging and counting of WBCs

In this thesis, we have presented microfabricated modules which can be used for capturing WBCs (cell trapping biochip) and imaging and counting micro-objects (microlens arrays). We envision an integrated WBC counting biochip which will incorporate the optimized cell trapping module as well as the high NA microlens arrays. The integrated biochip will enable simultaneous capture and imaging/counting of WBCs from human whole blood. In addition to the biochip, the WBC counting system would comprise of a portable reader for counting the number of WBCs captured in the biochip (**Figure 6.3**). While the biochip will constitute the disposable part of the system, the

reader will form the permanent part and will be battery operated. The reader will be equipped with a laser diode for exciting WBC fluorescence, an achromatic doublet lens for collecting cell fluorescence from the microlenses, an optical bandpass filter paper for filtering the incident laser light, a CCD sensor, a microprocessor for analyzing the image formed on the CCD sensor and an inexpensive LCD screen for displaying the final WBC count.

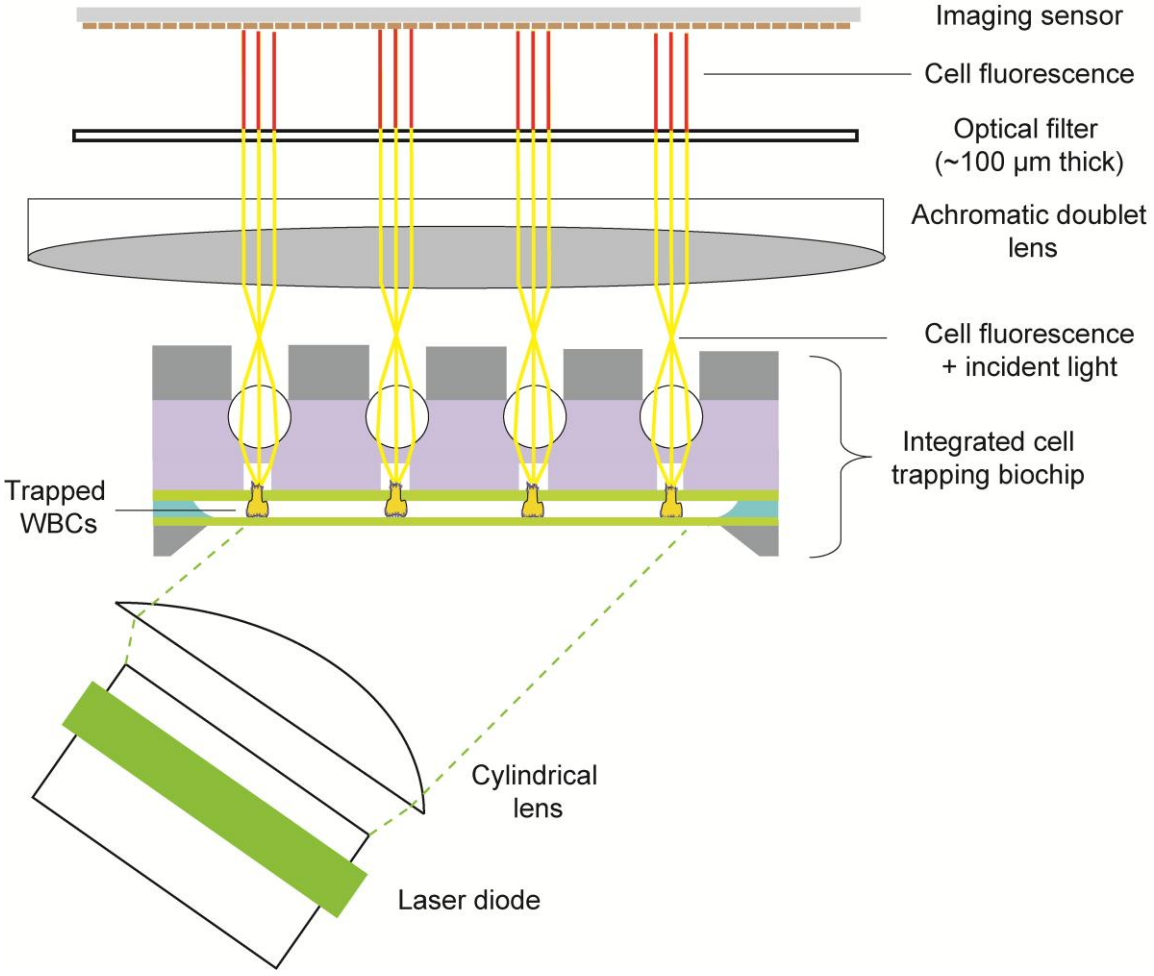

Figure 6.3: Schematic of the proposed benchtop WBC counting system. The integrated biochip (cell trapping module + microlens array) will constitute the disposable part of the system. The benchtop reading equipment will comprise of the optical components like the laser diode, cylindrical lens, achromatic doublet lens, bandpass filter and CCD sensor.

Though the proposed integrated system is targeted towards point-of-care WBC counting applications, we envision that this system can be used as a generic platform for on-chip cell sorting and imaging for various other biomedical research and diagnostic applications.

APPENDICES

Appendix A

Fabrication Process Flow Of The Microfluidic Devices

A.1 Fabrication process flow of the WBC trapping biochip

This device was used for the size based capture of WBCs. The fabrication process flow for this device involved fabrication and integration of two modules, a) the cell trapping module and b) the sample delivery module, as explained below.

a) **The cell trapping module -** The trapping module consists of an array of 4 μm in diameter microholes patterned on a silicon nitride layer.

Step 1: Wafer prefurnace clean

The silicon wafers were cleaned using standard prefurnace clean procedure to remove organic and ionic contaminants from the wafer surface. Wafers were dipped in a beaker containing 1 liter each of hydrogen peroxide (H_2O_2) and ammonium peroxide (NH_4OH) to remove organic contaminants like grease, dust particles and solvent residue. This was followed by immersing the wafers in a 1:100 hydrofluoric acid (HF) solution to remove the oxide layer. Subsequently, the wafers were dipped in a beaker containing 850 ml each of hydrogen peroxide (H_2O_2) and hydrochloric acid (HCl) to remove the ionic contaminants. The wafers were subsequently rinsed and dried using deionized (DI) water in a Vertec spin rinser drier.

Step 2: Low pressure chemical vapor deposition (LPCVD) of silicon oxide and low stress silicon nitride

The prefurnance cleaned wafers were loaded in a LPCVD furnace for deposition of 1.28 μm silicon oxide. This was followed by the deposition of a 1 μm thick layer of LPCVD low stress silicon nitride.

Step 3: Photolithographic patterning of the microhole array

The silicon wafer (with LPCVD silicon oxide and silicon nitride) was vapor primed with a photoresist adhesion promoter HMDS (Hexamethyldisilazane) in an oven. Subsequently, a 3 μm thick layer of SPR 220 3.0 photoresist was spun on the primed wafer at 3000 rpm followed by baking the spun photoresist in a 115 ºC oven for 45 seconds. The photoresist was exposed to ultraviolet (UV) rays through a photomask for 0.35 seconds using the GCA ACS 200 AutoStep exposure tool. The wafer was subsequently baked in a 115 ºC oven for 90 seconds followed by development of photoresist in AZ 300 MIF developer for 60 seconds. All the photolithographic patterning steps except the exposure step were performed using the ACS 200 cluster tool. An array of 4 μm in diameter microholes was obtained in the photoresist layer subsequent to this step. The wafer was hard baked on a 120 ºC hot plate for 10 minutes.

Step 4: Etching of the low stress silicon nitride

Using the patterned photoresist layer as the etch mask, the microhole array was etched on the silicon nitride layer using the reactive ion etching (RIE) technique. A nitride etching recipe (nitride etch rate 34 nm/min, photoresist etch rate 25 nm/min) on the Plasma-Therm 790 RIE tool was used for this step. Subsequently the photoresist layer was

stripped off by immersing the wafer in hot PRS 2000 (a positive photoresist stripper) for 10 minutes.

Step 5: Etching of silicon oxide

The wafer was immersed in a 1:10 solution of HF in DI water to perform an isotropic time etch of silicon oxide layer. An etch time of 8 minutes ensured the formation of microfluidic network in the silicon oxide layer. The wafer was rinsed in a bath of DI water for 10 minutes subsequent to the HF time etching step.

Step 6: Dicing of individual dies

The wafer with patterned microholes and silicon oxide microfluidic network was diced manually into individual dies using a silicon scribe. Since the individual dies were parallel to the wafer flat, they were easily obtained by cleaving the wafer in <110> direction.

b) The sample delivery module - It consisted of a network of microfluidic channels patterned in polydimethylsiloxane (PDMS) elastomer using soft lithography. The mold for casting the PDMS was made from SU-8 photoresist using standard photolithography technique.

Step 1: Wafer dehydration

A silicon wafer was dehydrated on a hotplate at 180° C for approximately 10 minutes.

Step 2: Spinning SU-8 photoresist

SU-8 2015 photoresist was used for mold fabrication as the desired microfluidic channel thickness was 20 μm. SU-8 2015 photoresist was spun on the silicon wafer for 5 sec @ 500 rpm and for 30 sec @ 2000 rpm to obtain a thickness of 20 μm.

Step 3: Soft baking the photoresist

The wafer was soft baked on a hot plate for 1 min @ 65 °C and for 4 min @ 95 °C.

Step 4: Exposure to UV rays

The wafer was exposed to UV through a photomask in 'soft contact' mode using a Karl Suss MA/BA-6 Mask Aligner tool (lamp power 20 mW/cm^2). An exposure time of 9 seconds was used for this step

Step 5: SU-8 Post-exposure bake

The wafer was baked on a hotplate for 1 min @ 65 °C and for 5 min @ 95 °C.

Step 6: Developing SU-8 photoresist

The baked SU-8 photoresist was developed using 'SU-8 Developer' for approximately 5 minutes. The wafer was rinsed with iso-propanol and dried using a N_2 gun.

Step 7: Hard baking the SU-8 mold

The wafer was baked on a hotplate for 10 min @ 180 °C.

Step 8: Silanization of the SU-8 mold

The SU-8 mold was placed in a vacuum chamber along with a small quantity of a silanizing agent such as Trimethylchlorosilane (TMCS) and silanized for approximately 30 minutes.

Step 9: Mixing PDMS prepolymer with curing agent

A 50 g PDMS prepolymer was mixed with the curing agent in the ratio 10:1.

Step 10: Pouring the prepolymer-curing agent mixture onto the SU-8 mold

The SU-8 mold was placed in a petri dish and fixed using a scotch tape. Subsequently, the PDMS-prepolymer mixture was poured onto the SU-8 mold.

Step 11: Degassing PDMS

The petri dish containing the mold was placed in a vacuum chamber until all the air bubbles were removed.

Step 12: Curing PDMS

The petri dish was placed in an oven at 65 °C for 2 hrs. The solidified PDMS was peeled off the mold and divided into individual sample delivery module using a sharp blade.

Step 13: Punching inlet and outlet holes in the sample delivery module

The inlet and the outlet holes were drilled using a 19 gauge stainless steel needle (0.031 inch inner diameter, 0.042 inch outer diameter; Kahnetics) (sharpened by electrolysis in a phosphoric acid solution).

Step 14: Cleaning the inlet and outlet holes

Drilling holes inside PDMS generates a significant amount of scrap that can easily clog the microfluidic channels. To clean this scrap, the inside surface of the hole was rubbed with a 25 gauge needle (1.5 inch, Becton-Dickinson) and the PDMS particles stuck on the inside surface were removed. This step completed the fabrication of the sample delivery module.

Bonding the cell trapping module to the PDMS sample delivery module

The cell trapping module is plasma bonded to the sample delivery module using air plasma (March Asher tool) at 30 W and 120 mTorr for 15 s. Alignment marks patterned on both the modules were used to align the microhole array (in the trapping module) with the microfluidic network (in the delivery module) before bonding. The bonded biochip was placed on a 65 °C hot plate for 10 minutes to increase the bond strength.

A.2 Fabrication process flow of the polymer-based microlens array

The planar polymer-based microlens array can be used for simultaneous imaging of a large number of micron-sized objetcs. The fabrication process flow for this device can be divided into three modules, a) fabricating two master molds from SU-8 photoresist using standard photolithography, b) fabricating the inflatable PDMS mold from the master molds using soft lithography and c) fabricating the microlens array from the inflatable mold, as explained below.

a) **Fabrication of SU-8 master molds –** Two master molds were fabricated using SU-8 photoresist using similar photolithography steps as explained in **A.1 (b)**.

Fabrication of the first SU-8 master mold

It involved successive patterning of two layers of SU-8 photoresist. Briefly, a silicon wafer was dehydrated and SU-8 2007 photoresist was spun at 1000 rpm for 30 sec to obtain a thickness of ~13 μm. This was followed by soft baking the wafer at 65 °C for 1 min and 95 °C for 3 min. The wafer was then exposed to UV through a photomask in 'soft contact' mode using the MA/BA-6 Mask Aligner Tool for 8 seconds. The wafer was baked post exposure at 65 °C for 1 min and 95 °C for 4 min and subsequently developed in the SU-8 developer for 3 min. The wafer was then hard baked at 180 °C for 10 min. This completed the fabrication of the 13 μm thick microfluidic network on the silicon wafer.

Subsequently a second layer of SU-8 was patterned on this microfluidic network. SU-8 2025 photoresist was spun at 2000 rpm for 30 sec to obtain a thickness of ~40 μm. This was followed by soft baking the wafer at 65 °C for 2 min and 95 °C for 6 min. The wafer

was then exposed to UV through a photomask in 'soft contact' mode using the MA/BA-6 Mask Aligner Tool for 10 seconds. Alignment marks were used to align the features in the first SU-8 layer with those in the 2nd photomask. The wafer was baked post exposure at 65 °C for 1 min and 95 °C for 6 min and subsequently developed in the SU-8 developer for 5 min. The wafer was then hard baked at 180 °C for 10 min. Subsequent to the lithography of second SU-8 layer, 40 μm thick circular SU-8 microchamber features were obtained on the top of 13 μm thick microfluidic channels.

Fabrication of the second SU-8 master mold

This SU-8 mold was fabricated to obtain the support PDMS layer. This mold consisted of an array of 200 μm x 200 μm microwells that aligned with the circular microchamber patterns fabricated in the previous step. For fabrication of this mold, a silicon wafer was dehydrated and SU-8 2050 photoresist was spun at 3000 rpm for 30 sec to obtain a thickness of ~50 μm. This was followed by soft baking the wafer at 65 °C for 3 min and 95 °C for 9 min. The wafer was then exposed to UV through a photomask in 'soft contact' mode using the MA/BA-6 Mask Aligner Tool for 14 seconds. The wafer was baked post exposure at 65 °C for 2 min and 95 °C for 7 min and subsequently developed in the SU-8 developer for 7 min. The wafer was then hard baked at 180 °C for 10 min. This completed the fabrication of the second SU-8 master mold.

b) Fabrication of the inflatable PDMS mold – This involved soft lithography technique of casting PDMS elastomer on the two SU-8 master molds followed by plasma assisted bonding of both PDMS parts.

Step 1: Spinning and curing PDMS membrane on the first SU-8 master mold

A 20:1 mixture of the PDMS prepolymer and curing agent was mixed and spun (WS-400 Lite Series Spin Processor; Laurell Technologies Corporation) on the silanized SU-8 mold at 1750 rpm to obtain a PDMS thickness of ~52 μm. A lesser proportion of curing agent to prepolymer (from the usual 1:10 ratio) ensured a softer PDMS membrane which was desired for higher deflections. The spun PDMS was then cured in a 65 °C oven for 30 min.

Step 2: Casting PDMS on the second SU-8 master mold

The process was similar to the one explained in **A.1 (b).** A mixture of PDMS prepolymer and curing agent in the ratio 10:1 was prepared and poured on the silanized SU-8 master mold to obtain ~1mm PDMS thickness. The SU-8 mold (with prepolymer-curing agent mixture) was placed in a vacuum chamber to remove all the air bubbles. Subsequently, the mold was placed in a 65 °C oven for 2 hrs to cure the PDMS. The solidified PDMS was peeled off the mold and divided into individual dies using a sharp blade.

Step 3: **Bonding the PDMS membrane to the PDMS support module**

The PDMS membrane (on the 1st SU-8 mold) and the PDMS support modules (obtained from the 2nd SU-8 mold) were exposed to air plasma (90W, 250 mTorr) for 35 sec. Subsequently, the microchamber structures underneath the PDMS membrane were aligned with the PDMS support module under a 5x microscope objective and the two parts were bonded by placing the assembly in the 65 °C oven for 10 min. This was followed by peeling off of the membrane-support layer assembly from the SU-8 master mold. Inlet holes (for injecting the UV-curable polymer) were punched in the PDMS assembly using a 19 gauge stainless steel needle.

Step 4: Bonding the PDMS assembly to the glass coverslip

The two layer PDMS assembly (obtained from the previous step) and a 175 μm thick glass coverslip (Fisherbrand Microscope Cover Glass, Catalog No. 12-544-C) were exposed to air plasma (90 W, 250 mTorr) for 35 sec and bonded to each other to obtain the sealed inflatable PDMS mold. A hollow steel pin (0.016 inch inner diameter, 0.025 inch outer diameter; Kahnetics) was attached to the inlet to facilitate chip-to-tube interface.

c) **Fabrication of the microlens array from the inflatable mold -** This involved filling a UV-curable polymer into the inflatable PDMS mold under pressure and curing it to obtain fixed focal length microlenses.

Pressure assisted injection of the UV-curable polymer and curing

A high index of refraction UV-curable polymer (Norland 60, index of refraction n = 1.56) was filled in a 3 ml syringe (Becton Dickinson 3 ml syringe, Catalog No. 309582) and injected into the inflatable mold under manually applied pressure. When all the air bubbles escaped from the PDMS mold (verified manually under a stereomicroscope), the inlet was connected to an air supply through a pressure controller (R-800-60 Sub miniature pressure regulator, output range 0-60 psi; AIRTROL Inc.). In order to solidify the UV-curable polymer at a particular pressure value, the inflatable mold (with pressurized polymer) was exposed to UV for 10 minutes under a UV lamp (365 nm wavelength; Entela). This resulted into curing of the polymer under the deflected PDMS membrane resulting into fixed focal length microlenses.

A.3 Fabrication process flow of the doublet microlens array

The high numerical aperture doublet microlens array can potentially be used for high resolution brightfield and fluorescence imaging of cells and tissues. Fabrication of the doublet microlens array can mainly be divided into three key processes, a) fabrication of the microhole array, b) assembly of glass microspheres on the array and c) spinning of a PDMS layer on the captured microspheres

a) Fabrication of the microhole array – Arrays of 56 μm in diameter through wafer microholes were etched in a silicon substrate.

Step 1: **Plasma enhanced chemical vapor deposition (PECVD) of silicon oxide**

A 2 μm thick PECVD silicon oxide was deposited on a silicon wafer using GSI PECVD tool.

Step 2: Photolithographic patterning of the microhole array

A 10 x 10 array of 56 μm in diameter microholes were patterned on the oxide layer using SPR 220 3.0 photoresist following same steps as **Step 3** of **A.1 (a)**.

Step 3: Etching of PECVD oxide

Using the patterned photoresist layer as the etch mask, the microhole array was etched on the silicon oxide layer using the deep reactive ion etching (DRIE) tool. An oxide etching recipe (oxide etch rate 0.2 μm /min, photoresist selectivity 1:1) on the STS DRIE tool was used for this step.

Step 4: Through wafer etch of the silicon wafer

Using the oxide layer and residual photoresist as etch mask, through wafer microholes were etched in the silicon wafer using the DRIE technique. A silicon etching recipe

(silicon etch rate 5 μm/min, photoresist selectivity 47:1, oxide selectivity 500:1) on the STS DRIE tool was used for this step. For the through wafer etch, the silicon wafer had to be mounted on a carrier wafer using a crystal bond and subsequent to the etching, the two wafers were separated by immersing them in a hot PRS bath which dissolves the crystal bond.

Step 5: Thinning of the silicon wafer

The silicon wafer was thinned down to 200 μm (from the non oxide side) using a lapping tool followed by the polishing of the etched surface using the chemical mechanical polishing (CMP) tool. This completed the fabrication process for the microhole array.

Step 6: Dicing of individual dies

The thinned silicon wafer with patterned microholes was diced manually into individual dies using a silicon scribe.

b) Assembly of glass microspheres on the array – Glass microspheres (60 μm nominal diameter, refractive index 1.51 at a wavelength of 589 nm; catalog no. 02718-AB, Structure Probe, Inc.) were assembled on the microhole array.

Step 1: Fabrication of a PDMS suction port

A 5 mm diameter hole was punched in a 1 cm thick PDMS piece, which was aligned and attached to the microhole array. The PDMS piece adhered to the silicon surface without any additional adhesion treatment. A tube connected to a 3 ml syringe was connected to the other end of the 5 mm hole to apply the suction force.

Step 2: Dispensing and assembly of glass microspheres

An aqueous solution of glass microspheres was then dispensed on the oxide-coated silicon surface. A suction force was subsequently applied manually from the other side of the substrate to assemble and trap the glass microspheres atop of the microhole array. A piece of double sided tape was attached on a glass coverslip and the tape was brought in contact with the wafer surface resulting into the removal of the extra microspheres. This resulted into the assembly of microspheres on the microhole array.

c) **Spinning of PDMS on the assembled microspheres –** This process completed the doublet microlens fabrication by spinning a PDMS layer on the microspheres.

A 10:1 PDMS prepolymer to curing agent mixture was prepared and spun (WS-400 Lite Series Spin Processor; Laurell Technologies Corporation) on the silicon microhole array (with assembled microspheres) at 1600 rpm for 1 min. In order to prevent the flying off of the microspheres during the spinning step, the lowest acceleration of 108 rpm per sec was used. This resulted into a PDMS thickness of ~75 µm. The PDMS was subsequently cured on a 65ºC hot plate for one hour. This completed the fabrication process of the doublet microlens array.

Appendix B

Opto-mechanical Simulations Of Planar Microlens' Focal Length And Numerical Aperture

In this section, we will describe the opto-mechanical simulations performed to characterize the pressure dependence of the effective focal length (EFL) and numerical aperture (NA) of the planar, polymer-based microlenses. Pressure dependent deflection of the PDMS membrane was obtained using a finite element analysis software ANSYS. The resulting microlens profile was imported into an optical design software (OSLO LT) to obtain the microlens EFL and NA.

B.1 Microlens profile using ANSYS

An ANSYS programming code was written to solve for the pressure dependent deflection of the PDMS membrane for given dimensions (thickness, diameter). This code creates the geometry of the membrane and imparts it the elastic properties (Young's Modulus, Poisson's Ratio). It meshes the entire structure for the simulation and applies constraints on different surfaces. Finally, load (pressure in Pa) is applied on the membrane and the resulting membrane deflection is computed. An example ANSYS code for solving the deflection of a 60 μm in diameter membrane under 3 psi (200 kPa) pressure has been presented below.

ANSYS code for computing the pressure induced PDMS membrane deflection:

```
/prep7

!creating the geometry of the membrane
CYLIND, 3e-5, 7e-5, 0, 5.2e-5
CYLIND, 0, 3e-5, 4e-5, 5.2e-5
alls
vadd, all

!meshing the struture
!et for defining the element type
et, 1, solid95

!defining material properties (Young's Modulus, Poisson's Ratio)
mp, ex, 1, 30e5
mp, prxy, 1, 0.49

!meshing
alls
mshkey, 0
smrtsize, 2
MSHAPE, 1, 3d
vmesh, all

!constraining surfaces
alls
da, 1, all, 0
da, 3, all, 0
da, 4, all, 0

!defining loads
sfa, 7, , pres, 200000

!solving for the membrane deflection
/sol
solve
```

Upon successful run of the program, the resulting membrane deflection can be visualized either graphically (**Figure B.1**) or the values can be imported into a text file.

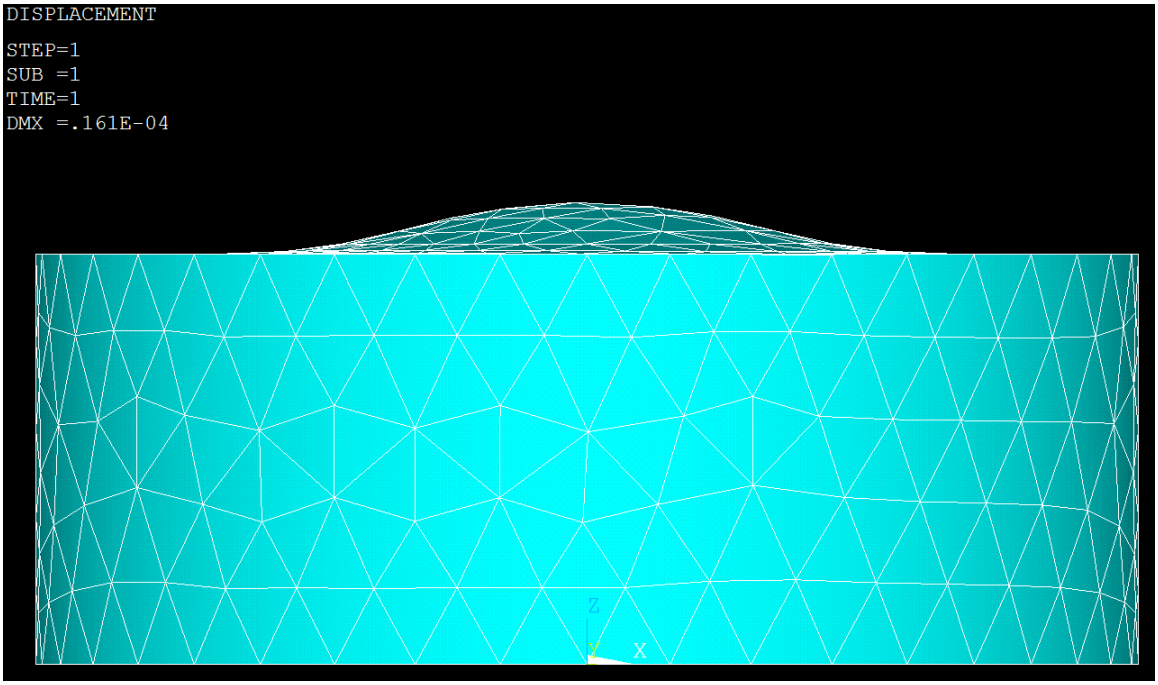

Figure B.1: A representative PDMS membrane deflection (microlens) profile obtained using ANSYS mechanical simulations.

There was a difference between the maximum deflection values of the outer and the inner surface of the membrane. The inner surface underwent a larger deflection resulting into a smaller radius of curvature. The radius of curvature of the inner surface was estimated by drawing a circle which passed through the center point (point of maximum deflection) and the two edges of the inner surface. Similar process was adopted to estimate the radius of curvature of the outer membrane surface. These radii of curvature values were used by the optical simulation software (OSLO LT) to compute the microlens effective focal length and numerical aperture (**Figure B.2**).

A

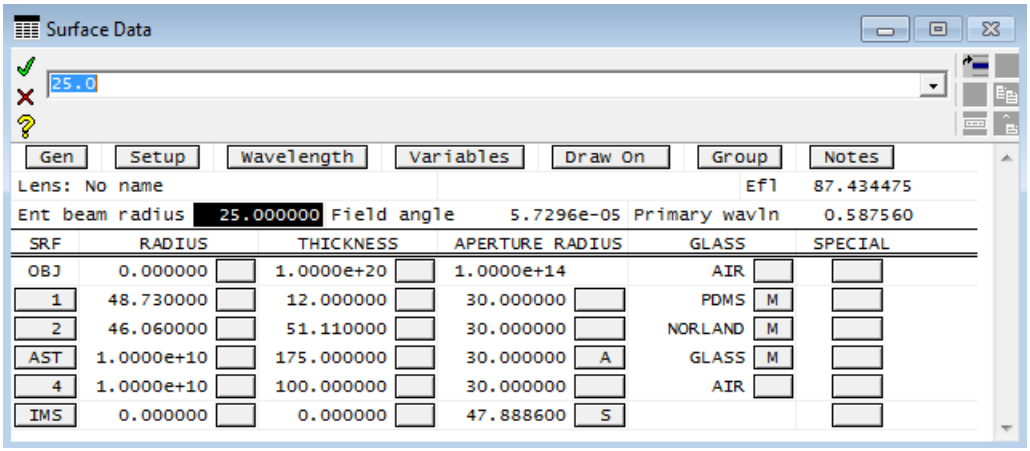

B

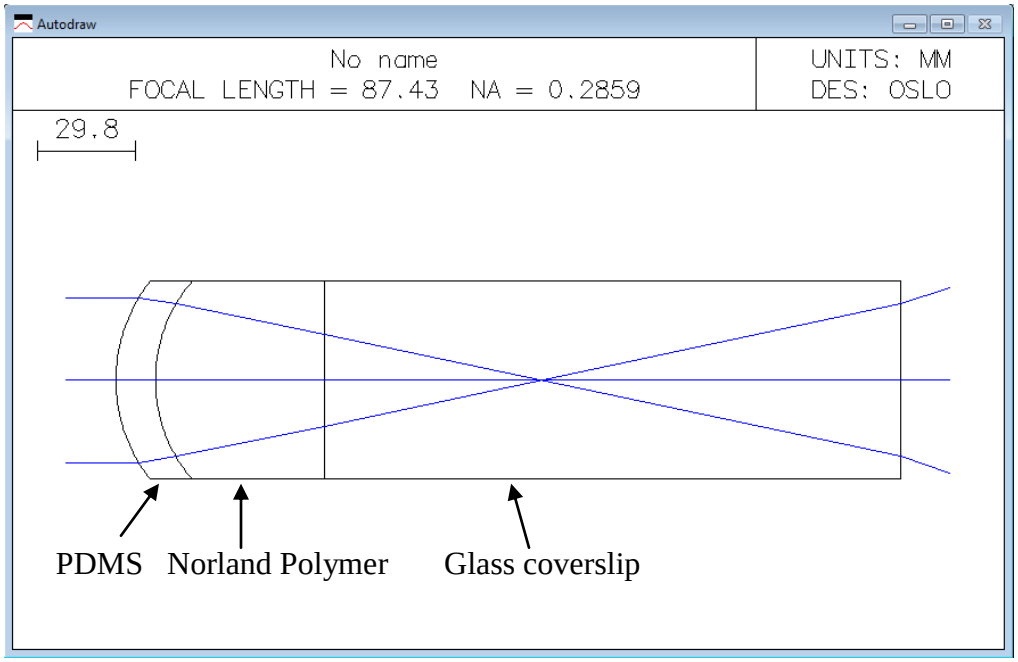

Figure B.2: Simulation of microlens' focal length and numerical aperture using OLSO software. **(A)** Lens surface data spreadsheet used for entering the lens material and geometrical properties into the software. **(B)** A ray diagram obtained from the OSLO software demonstrating the microlens' focusing properties.

BIBLIOGRAPHY

BIBLIOGRAPHY

[1] "Global report: UNAIDS report on the global AIDS epidemic 2010," Joint United Nations Programme on HIV/AIDS (UNAIDS) 2010.

[2] "World malaria report: 2011," World Health Organization 2011.

[3] "Global tuberculosis control: WHO report 2011," World Health Organization 2011.

[4] J. Cohen, "The New World of Global Health," *Science,* vol. 311, pp. 162-167, 2006.

[5] T. M. Brown, M. Cueto, and E. Fee, "The World Health Organization and the Transition From "International" • to "Global" • Public Health," *American journal of public health (1971),* vol. 96, pp. 62-72, 2006.

[6] S. Okie, "Global Health - The Gates-Buffett Effect," *The New England journal of medicine,* vol. 355, pp. 1084-1088, 2006.

[7] N. Ravishankar, P. Gubbins, R. J. Cooley, K. Leach-Kemon, C. M. Michaud, D. T. Jamison, and C. J. L. Murray, "Financing of global health: tracking development assistance for health from 1990 to 2007," *The Lancet (North American edition),* vol. 373, p. 2113, 2009.

[8] T. Peter, A. Badrichani, E. Wu, R. Freeman, B. Ncube, F. Ariki, J. Daily, Y. Shimada, and M. Murtagh, "Challenges in implementing CD4 testing in resource-limited settings," *Cytometry. Part B, Clinical cytometry,* vol. 74B, pp. S123-S130, 2008.

[9] W. G. Lee, Y. Kim, B. G. Chung, U. Demirci, and A. Khademhosseini, "Nano/Microfluidics for diagnosis of infectious diseases in developing countries," *Advanced drug delivery reviews,* vol. 62, pp. 449-457, 2010.

[10] K. Rogers, *Blood: physiology and circulation*. New York: Britannica Educational Publishing, 2011.

[11] S. Sell, *Immunology, immunopathology and immunity*. Washington, DC: ASM Press, 2001.

[12] T. H. McConnell, *The nature of disease: pathology for the health professions*. Baltimore: Lippincott Williams & Wilkins, 2007.

[13] L. Bonetta, "Flow cytometry smaller and better," *Nat Meth,* vol. 2, pp. 785-795, 2005.

[14] L. A. Herzenberg, D. Parks, B. Sahaf, O. Perez, M. Roederer, and L. A. Herzenberg, "The History and Future of the Fluorescence Activated Cell Sorter and Flow Cytometry: A View from Stanford," *Clinical Chemistry,* vol. 48, pp. 1819-1827, 2002.

[15] G. M. Whitesides, "The origins and the future of microfluidics," *Nature (London),* vol. 442, pp. 368-373, 2006.

[16] P. Abgrall and A.-M. Gue, "Lab-on-chip technologies: making a microfluidic network and coupling it into a complete microsystem - a review," *Journal of micromechanics and microengineering,* vol. 17, pp. R15-R49, 2007.

[17] T. Thorsen, S. J. Maerkl, and S. R. Quake, "Microfluidic Large-Scale Integration," *Science (New York, N.Y.),* vol. 298, pp. 580-584, 2002.

[18] R. Daw and J. Finkelstein, "Lab on a chip," *Nature,* vol. 442, pp. 367-367, 2006.

[19] H. Craighead, "Future lab-on-a-chip technologies for interrogating individual molecules," *Nature,* vol. 442, pp. 387-393, 2006.

[20] D. Psaltis, S. R. Quake, and C. Yang, "Developing optofluidic technology through the fusion of microfluidics and optics," *Nature,* vol. 442, pp. 381-386, 2006.

[21] A. J. deMello, "Control and detection of chemical reactions in microfluidic systems," *Nature,* vol. 442, pp. 394-402, 2006.

[22] J. El-Ali, P. K. Sorger, and K. F. Jensen, "Cells on chips," *Nature,* vol. 442, pp. 403-411, 2006.

[23] P. Yager, T. Edwards, E. Fu, K. Helton, K. Nelson, M. R. Tam, and B. H. Weigl, "Microfluidic diagnostic technologies for global public health," *Nature,* vol. 442, pp. 412-418, 2006.

[24] C. D. Chin, V. Linder, and S. K. Sia, "Lab-on-a-chip devices for global health: Past studies and future opportunities," *Lab on a Chip,* vol. 7, pp. 41-57, 2007.

[25] E. D. Pratt, C. Huang, B. G. Hawkins, J. P. Gleghorn, and B. J. Kirby, "Rare cell capture in microfluidic devices," *Chemical Engineering Science,* pp. 1508-1522, 2011.

[26] W. R. Rodriguez, N. Christodoulides, P. N. Floriano, S. Graham, S. Mohanty, M. Dixon, M. Hsiang, T. Peter, S. Zavahir, I. Thior, D. Romanovicz, B. Bernard, A. P. Goodey, B. D. Walker, and J. T. McDevitt, "A Microchip CD4 Counting Method for HIV Monitoring in Resource-Poor Settings," *PLoS Med,* vol. 2, pp. 663-672, 2005.

[27] H. M. Ji, V. Samper, Y. Chen, C. K. Heng, T. M. Lim, and L. Yobas, "Silicon-based microfilters for whole blood cell separation," *Biomedical Microdevices,* vol. 10, pp. 251-257, 2008.

[28] W. C. Chang, L. P. Lee, and D. Liepmann, "Adhesion-based capture and separation of cells for microfluidic devices," *MRS proceedings,* vol. 729, p. 155, 2002.

[29] W. C. Chang, L. P. Lee, and D. Liepmann, "Biomimetic technique for adhesion-based collection and separation of cells in a microfluidic channel," *Lab on a Chip,* vol. 5, pp. 64-73, 2005.

[30] S. K. Murthy, A. Sin, R. G. Tompkins, and M. Toner, "Effect of Flow and Surface Conditions on Human Lymphocyte Isolation Using Microfluidic Chambers," *Langmuir,* vol. 20, pp. 11649-11655, 2012/05/31 2004.

[31] A. Sin, S. K. Murthy, A. Revzin, R. G. Tompkins, and M. Toner, "Enrichment using antibody-coated microfluidic chambers in shear flow: Model mixtures of human lymphocytes," *Biotechnology and Bioengineering,* vol. 91, pp. 816-826, 2005.

[32] X. Cheng, D. Irimia, M. Dixon, K. Sekine, U. Demirci, L. Zamir, R. G. Tompkins, W. R. Rodriguez, and M. Toner, "A microfluidic device for practical label-free CD4 T cell counting of HIV-infected subjects," *Lab on a Chip,* vol. 7, pp. 170-178, 2007.

[33] X. Cheng, A. Gupta, C. Chen, R. G. Tompkins, W. R. Rodriguez, and M. Toner, "Enhancing the performance of a point-of-care CD4 T-cell counting microchip through monocyte depletion for HIV/AIDS diagnostics," *Lab on a Chip,* vol. 9, pp. 1357-1364, 2009.

[34] N. Nguyen, "Micro-optofluidic lenses: a review," *Biomicrofluidics,* vol. 4, p. 031501, 2010.

[35] M.-H. Wu and G. M. Whitesides, "Fabrication of two-dimensional arrays of microlenses and their applications in photolithography," *Journal of micromechanics and microengineering,* vol. 12, p. 747, 2002.

[36] H. Yang, C. Chao, M. Wei, and C. Lin, "High fill-factor microlens array mold insert fabrication using a thermal reflow process," *Journal of micromechanics and microengineering,* vol. 14, p. 1197, 2004.

[37] S. Biehl, R. Danzebrink, P. Oliveira, and M. A. Aegerter, "Refractive Microlens Fabrication by Ink-Jet Process," *Journal of Sol-Gel Science and Technology,* vol. 13, pp. 177-182-182, 1998.

[38] C. H. Tien, C. H. Hung, and T. H. Yu, "Microlens Arrays by Direct-Writing Inkjet Print for LCD Backlighting Applications," *Journal of display technology,* vol. 5, pp. 147-151, 2009.

[39] C. Yi, H. Chien-Hsun, and H. Ying-Chien, "High Numerical-Aperture Microlens Fabricated by Focused Ion Beam Milling," in *Optical Data Storage*, 2007, p. MC6.

[40] D. Wu, S.-Z. Wu, L.-G. Niu, Q.-D. Chen, R. Wang, J.-F. Song, H.-H. Fang, and H.-B. Sun, "High numerical aperture microlens arrays of close packing," *Applied physics letters,* vol. 97, p. 031109, 2010.

[41] M. V. Kunnavakkam, F. M. Houlihan, M. Schlax, J. A. Liddle, P. Kolodner, O. Nalamasu, and J. A. Rogers, "Low-cost, low-loss microlens arrays fabricated by

soft-lithography replication process," *Applied physics letters,* vol. 82, p. 1152, 2003.

[42] X. C. Yuan, W. X. Yu, M. He, J. Bu, W. C. Cheong, H. B. Niu, and X. Peng, "Soft-lithography-enabled fabrication of large numerical aperture refractive microlens array in hybrid SiO_2-TiO_2 sol-gel glass," *Applied physics letters,* vol. 86, p. 114102, 2005.

[43] J. Zhu, J. Shi, Y. Wang, and P. He, "Spherical micro-lens array of PMMA produced by micro-molding," *Chinese Journal of Chemical Physics,* vol. 19, pp. 443-446, 2006.

[44] J. Albero, L. Nieradko, C. Gorecki, H. Ottevaere, V. Gomez, H. Thienpont, J. Pietarinen, B. Päivänranta, and N. Passilly, "Fabrication of spherical microlenses by a combination of isotropic wet etching of silicon and molding techniques," *Optics express,* vol. 17, p. 6283, 2009.

[45] C. A. Janeway, *Immunobiology: the immune system in health and disease*, 1996.

[46] L. J. Eales, *Immunology for Life Scientists*: John Wiley & Sons, Incorporated, 2003.

[47] D. W. Brown, W. H. Giles, and J. B. Croft, "White blood cell count:: An independent predictor of coronary heart disease mortality among a national cohort," *Journal of clinical epidemiology,* vol. 54, p. 316, 2001.

[48] B. D. Cheson, J. M. Bennett, M. Grever, N. Kay, M. J. Keating, S. O'Brien, and K. R. Rai, "National Cancer Institute-sponsored Working Group guidelines for chronic lymphocytic leukemia: revised guidelines for diagnosis and treatment," *Blood,* vol. 87, p. 4990, 1996.

[49] M. F. Liu, C. R. Wang, L. L. Fung, and C. R. Wu, "Decreased CD4 CD25 T Cells in Peripheral Blood of Patients with Systemic Lupus Erythematosus," *Scandinavian journal of immunology,* vol. 59, pp. 198-202, 2004.

[50] S. Ohshima, Y. Saeki, T. Mima, M. Sasai, K. Nishioka, H. Ishida, M. Shimizu, M. Suemura, R. McCloskey, and T. Kishimoto, "Long-term follow-up of the changes in circulating cytokines, soluble cytokine receptors, and white blood cell subset counts in patients with rheumatoid arthritis (RA) after monoclonal anti-TNFÎ± antibody therapy," *Journal of clinical immunology,* vol. 19, pp. 305-313, 1999.

[51] J. Sunyer, A. Munoz, Y. Peng, J. Margolick, J. S. Chmiel, J. Oishi, L. Kingsley, and J. M. Samet, "Longitudinal relation between smoking and white blood cells," *American journal of epidemiology,* vol. 144, p. 734, 1996.

[52] N. Nakanishi, K. Suzuki, and K. Tatara, "Association between lifestyle and white blood cell count: a study of Japanese male office workers," *Occupational medicine (Oxford),* vol. 53, pp. 135-137, 2003.

[53] N. Nishitani and H. Sakakibara, "Subjective poor sleep and white blood cell count in male Japanese workers," *Industrial health,* vol. 45, p. 296, 2007.

[54] D. Pappas and K. Wang, "Cellular separations: A review of new challenges in analytical chemistry," *Analytica Chimica Acta,* vol. 601, pp. 26-35, 2007.

[55] A. Y. Fu, C. Spence, A. Scherer, F. H. Arnold, and S. R. Quake, "A microfabricated fluorescence-activated cell sorter," *Nature biotechnology,* vol. 17, p. 1109, 1999.

[56] A. Y. Fu, H. Chou, C. Spence, F. H. Arnold, and S. R. Quake, "An Integrated Microfabricated Cell Sorter," *Analytical chemistry (Washington),* vol. 74, pp. 2451-2457, 2002.

[57] D. Huh, Y. Tung, H. Wei, J. B. Grotberg, S. J. Skerlos, K. Kurabayashi, and S. Takayama, "Use of air-liquid two-phase flow in hydrophobic microfluidic channels for disposable flow cytometers," *Biomedical microdevices,* vol. 4, pp. 141-149, 2002.

[58] J. Voldman, M. L. Gray, M. Toner, and M. A. Schmidt, "A Microfabrication-Based Dynamic Array Cytometer," *Analytical Chemistry* vol. 74, pp. 3984-3990, 2002.

[59] D. Holmes, D. Pettigrew, C. H. Reccius, J. D. Gwyer, C. Van Berkel, J. Holloway, D. E. Davies, and H. Morgan, "Leukocyte analysis and differentiation using high speed microfluidic single cell impedance cytometry," *Lab on a chip,* vol. 9, pp. 2881-2889, 2009.

[60] S. C. Hur, H. T. K. Tse, and D. Di Carlo, "Sheathless inertial cell ordering for extreme throughput flow cytometry," *Lab on a chip,* vol. 10, pp. 274-280, 2010.

[61] Z. Wang, S. Y. Chin, C. D. Chin, J. Sarik, M. Harper, J. Justman, and S. K. Sia, "Microfluidic CD4+ T-Cell Counting Device Using Chemiluminescence-Based Detection," *Analytical Chemistry*, vol. 82, pp. 36-40, 2010.

[62] X. Cheng, Y. Liu, D. Irimia, L. Yang, Z. Lee, W. R. Rodriguez, M. Toner, and R. Bashir, "Cell detection and counting through cell lysate impedance spectroscopy in microfluidic devices," *Lab on a Chip*, vol. 7, pp. 746-755, 2007.

[63] A. Osei-Bimpong, C. Jury, R. McLean, and S. M. Lewis, "Point-of-care method for total white cell count: an evaluation of the device," *International Journal of Laboratory Hematology*, vol. 31, pp. 657-664, 2009.

[64] K. C. Tang, E. Liao, W. L. Ong, J. D. S. Wong, A. Agarwal, R. Nagarajan, and L. Yobas, "Evaluation of bonding between oxygen plasma treated polydimethyl siloxane and passivated silicon," *Journal of Physics: Conference Series*, vol. 34, pp. 155-161, 2006.

[65] K. W. Oh, K. Lee, B. Ahn, and E. P. Furlani, "Design of pressure-driven microfluidic networks using electric circuit analogy," *Lab on a chip*, vol. 12, pp. 515-545, 2012.

[66] H. Bruus, *Theoretical Microfluidics*: Oxford University Press, 2008.

[67] J. Hu, "The evolution of commercialized glucose sensors in China," *Biosensors & bioelectronics*, vol. 24, p. 1083, 2009.

[68] G. Shao, J. Wang, Z. Li, L. Saraf, W. Wang, and Y. Lin, "Poly (dimethylsiloxane) microchip-based immunoassay with multiple reaction zones: Toward on-chip multiplex detection platform," *Sensors and actuators. B, Chemical*, vol. 159, pp. 44-50, 2011.

[69] S. U. Son, J.-H. Seo, Y. H. Choi, and S. S. Lee, "Fabrication of a disposable biochip for measuring percent hemoglobin A1c (%HbA1c)," *Sensors and Actuators A: Physical*, vol. 130-131, pp. 267-272, 2006.

[70] J. Steigert, T. Brenner, M. Grumann, L. Riegger, S. Lutz, R. Zengerle, and J. Ducree, "Integrated siphon-based metering and sedimentation of whole blood on a hydrophilic lab-on-a-disk," *Biomedical microdevices*, vol. 9, pp. 675-679, 2007.

[71] I. K. Dimov, L. Basabe-Desmonts, J. L. Garcia-Cordero, B. M. Ross, A. J. Ricco, and L. P. Lee, "Stand-alone self-powered integrated microfluidic blood analysis system (SIMBAS)," *Lab on a chip,* vol. 11, p. 845, 2011.

[72] F. B. McCormick, F. A. P. Tooley, T. J. Cloonan, J. M. Sasian, H. S. Hinton, K. O. Mersereau, and A. Y. Feldblum, "Optical interconnections using microlens arrays," *Optical and quantum electronics,* vol. 20, p. S465, 1992.

[73] H. Hamam, "A two-way optical interconnection network using a single mode fiber array," *Optics Communications,* vol. 150, pp. 270-6, 1998.

[74] Y. P. Huang, H. P. D. Shieh, and S. T. Wu, "Applications of multidirectional asymmetrical microlens-array light control films on reflective liquid crystal displays for image quality enhancement," *Applied Optics,* vol. 43, pp. 3656-3663, 2004.

[75] H. Peng, Y. L. Ho, X. J. Yu, M. Wong, and H. S. Kwok, "Coupling efficiency enhancement in organic light-emitting devices using microlens array-theory and experiment," *Journal of display technology,* vol. 1, p. 278, 2005.

[76] K. Cai-Jun, Y. Xin-Jian, L. Jian-Jun, and C. Si-Hai, "Fabrication, Testing and Integration Technologies of Polymer Microlens for Pt/Si Schottky-Barrier Infrared Charge Coupled Device Applications," *Chinese Physics Letters,* vol. 22, pp. 135-138, 2005.

[77] B. Javidi, S.-H. Hong, and O. Matoba, "Multidimensional optical sensor and imaging system," *Appl. Opt.,* vol. 45, pp. 2986-2994, 2006.

[78] M.-H. Wu, K. E. Paul, J. Yang, and G. M. Whitesides, "Fabrication of frequency-selective surfaces using microlens projection photolithography," *Applied Physics Letters,* vol. 80, pp. 3500-3502, 2002.

[79] K. F. Chan, Z. Feng, R. Yang, A. Ishikawa, and W. Mei, "High-resolution maskless lithography," *Journal of Microlithography, Microfabrication, and Microsystems,* vol. 2, pp. 331-339, 2003.

[80] M. Eisner, N. Lindlein, and J. Schwider, "Confocal microscopy with a refractive microlens-pinhole array," *Opt. Lett.,* vol. 23, pp. 748-749, 1998.

[81] J. C. Roulet, R. Volkel, H. P. Herzig, E. Verpoorte, N. F. de Rooij, and R. Dandliker, "Fabrication of multilayer systems combining microfluidic and microoptical elements for fluorescence detection," *Journal of microelectromechanical systems,* vol. 10, pp. 482-491, 2001.

[82] K. Aljasem, D. Mader, A. Werber, H. Zappe, and S. Reichelt, "Pneumatically-actuated tunable microlens for endoscopic optical coherence tomography Transducers 2007 - 2007 International Solid-State Sensors Actuators and Microsystems Conference," 2007, pp. 2557-2560.

[83] D. A. Fletcher, K. B. Crozier, K. W. Guarini, S. C. Minne, G. S. Kino, C. F. Quate, and K. E. Goodson, "Microfabricated silicon solid immersion lens," *Journal of microelectromechanical systems,* vol. 10, p. 450, 2001.

[84] N. S. Ong, Y. H. Koh, and Y. Q. Fu, "Microlens array produced using hot embossing process," *Microelectronic Engineering,* vol. 60, pp. 365-379, 2002.

[85] S. D. Moon, S. Kang, and J. U. Bu, "Fabrication of polymeric microlens of hemispherical shape using micromolding," *Optical Engineering,* vol. 41, pp. 2267-2270, 2002.

[86] P. Nussbaum, I. Philipoussis, A. Husser, and H. P. Herzig, "Simple technique for replication of micro-optical elements " *Optical Engineering,* vol. 37, pp. 6283-6292, 1998.

[87] S. Kopetz, D. Cai, E. Rabe, and A. Neyer, "PDMS-based optical waveguide layer for integration in electrical-optical circuit boards," *AEU - International Journal of Electronics and Communications,* vol. 61, pp. 163-167, 2007.

[88] F. Schneider, T. Fellner, J. Wilde, and U. Wallrabe, "Mechanical properties of silicones for MEMS," *Journal of Micromechanics and Microengineering,* vol. 18, p. 065008, 2008.

[89] K. L. Mills, X. Y. Zhu, S. C. Takayama, and M. D. Thouless, "The mechanical properties of a surface-modified layer on polydimethylsiloxane," *Journal of materials research,* vol. 23, pp. 37-48, 2008.

[90] N. Chronis, G. Liu, K. H. Jeong, and L. P. Lee, "Tunable liquid-filled microlens array integrated with microfluidic network," *Optics Express,* vol. 11, pp. 2370-2378, 2003.

[91] X. Yu, Z. Wang, and Y. Han, "Microlenses fabricated by discontinuous dewetting and soft lithography," *Microelectronic Engineering,* vol. 85, pp. 1878-1881, 2008.

[92] D. S. Reichmuth, S. K. Wang, L. M. Barrett, D. J. Throckmorton, W. Einfeld, and A. K. Singh, "Rapid microchip-based electrophoretic immunoassays for the detection of swine influenza virus," *Lab on a Chip,* vol. 8, pp. 1319-1324, 2008.

[93] E. Wilder, M. Fasolka, S. Guo, C. Stafford, and S. Lin-Gibson, "Measuring the modulus of soft polymer networks via a buckling-based metrology," *Macromolecules,* vol. 39, pp. 4138-4143, 2006.

[94] M. Oikawa, H. Nemoto, K. Hamanaka, and E. Okuda, "High numerical aperture planar microlens with swelled structure," *Applied optics-OT,* vol. 29, pp. 4077-4080, 1990.

[95] S. Inoué, *Video microscopy: the fundamentals,* 1997.

[96] J. R. Polimeni, E. L. Schwartz, D. Granquist-Fraser, and R. J. Wood, "Physical limits to spatial resolution of optical recording: clarifying the spatial structure of cortical hypercolumns," *Proceedings of the National Academy of Sciences of the United States of America,* vol. 102, pp. 4158-63, 2005.

[97] K. Itakura, T. Nobusada, N. Kokusenya, R. Nagayoshi, and R. Ozaki, "A 1-mm 50 k-Pixel IT CCD image sensor for miniature camera system," *I.E.E.E. transactions on electron devices,* vol. 47, p. 65, 2000.

[98] W. Yang, D. B. Conkey, B. Wu, D. Yin, A. R. Hawkins, and H. Schmidt, "Atomic spectroscopy on a chip," *Nature photonics,* vol. 1, p. 331, 2007.

[99] E. Verpoorte, "Chip vision-optics for microchips," *Lab on a chip,* vol. 3, pp. 42N-52N, 2003.

[100] H. P. D. Shieh, Y. P. Huang, and K. W. Chien, "Micro-optics for liquid crystal displays applications," *Journal of display technology,* vol. 1, p. 62, 2005.

[101] J. Lim, S. S. Oh, D. Y. Kim, S. H. Cho, I. T. Kim, S. H. Han, H. Takezoe, E. H. Choi, G. S. Cho, Y. H. Seo, S. O. Kang, and B. Park, "Enhanced out-coupling factor of microcavity organic light-emitting devices with irregular microlens array," *Optics express,* vol. 14, p. 6564, 2006.

[102] S.-C. Shen, C.-T. Pan, H.-P. Chou, and M.-C. Chou, "Batch Assembly Micro-Ball Lens Array for Si-Based Optical Coupling Platform in Free Space," *Optical review,* vol. 8, p. 373, 2001.

[103] M. He, X. C. Yuan, N. Ngo, J. Bu, and S. Tao, "Low-cost and efficient coupling technique using reflowed sol-gel microlens," *Optics express,* vol. 11, p. 1621, 2003.

[104] S. C. Shen, C. T. Pan, K. H. Liu, C. H. Chao, and J. C. Huang, "Fabrication of an eyeball-like spherical micro-lens array using extrusion for optical fiber coupling," *Journal of micromechanics and microengineering,* vol. 19, p. 125017, 2009.

[105] C. Oconnell, R. Sherlock, and T. J. Glynn, "Fabrication of a reusable microlens array for laser-based structuring," *Optical engineering,* vol. 49, p. 014201, 2010.

[106] K. Aljasem, A. Werber, A. Seifert, and H. Zappe, "Fiber optic tunable probe for endoscopic optical coherence tomography," *Journal of optics. A, Pure and applied optics,* vol. 10, p. 044012, 2008.

[107] R. P. J. Barretto, B. Messerschmidt, and M. J. Schnitzer, "In vivo fluorescence imaging with high-resolution microlenses," *Nature Methods,* vol. 6, p. 511, 2009.

[108] T. Mogi, K. Hatakeyama, T. Taguchi, H. Wake, T. Tanaami, M. Hosokawa, T. Tanaka, and T. Matsunaga, "Real-time detection of DNA hybridization on microarray using a CCD-based imaging system equipped with a rotated microlens array disk," *Biosensors & bioelectronics,* vol. 26, pp. 1942-6, 2011.

[109] Z. D. Popovic, R. A. Sprague, and G. A. N. Connell, "Technique for monolithic fabrication of microlens arrays," *Applied optics,* vol. 27, p. 1281, 1988.

[110] H.-T. Hsieh and G.-D. J. Su, "A novel boundary-confined method for high numerical aperture microlens array fabrication," *Journal of micromechanics and microengineering,* vol. 20, p. 035023, 2010.

[111] J. Y. Kim, N. B. Brauer, V. Fakhfouri, D. L. Boiko, E. Charbon, G. Grutzner, and J. Brugger, "Hybrid polymer microlens arrays with high numerical apertures fabricated using simple ink-jet printing technique," *Opt. Mater. Express,* vol. 1, pp. 259-269, 2011.

[112] A. Tripathi, T. V. Chokshi, and N. Chronis, "A high numerical aperture, polymer-based, planar microlens array," *Optics express,* vol. 17, p. 19908, 2009.

[113] Y. R. Huang and H. P. Chou, "Fabrication of ball-type spherical microlens array for optical fiber coupling," *Proceedings of SPIE, the international society for optical engineering,* vol. 5347, pp. 281-286, 2004.

[114] M.-H. Wu and G. M. Whitesides, "Fabrication of arrays of two-dimensional micropatterns using microspheres as lenses for projection photolithography," *Applied physics letters,* vol. 78, p. 2273, 2001.

[115] J.-Y. Huang, Y.-S. Lu, and J. A. Yeh, "Self-assembled high NA microlens arrays using global dielectricphoretic energy wells," *Optics express,* vol. 14, p. 10779, 2006.

[116] G. Schlingloff, H.-J. Kiel, and A. Schober, "Microlenses as Amplification for CCD-Based Detection Devices for Screening Applications in Biology, Biochemistry, and Chemistry," *Appl. Opt.,* vol. 37, pp. 1930-1934, 1998.

[117] H. Ren, Y.-H. Fan, and S.-T. Wu, "Liquid-crystal microlens arrays using patterned polymernetworks," *Opt. Lett.,* vol. 29, pp. 1608-1610, 2004.

[118] C.-Y. Chen, W.-C. Su, Y.-F. Wang, and C.-H. Chen, "Reduction of distortion aberration in imaging systems by using a microlens array," *Optics Communications,* vol. 283, pp. 2798-2802, 2010.

[119] R. Guo, D. Yuan, and S. Das, "Large-area microlens arrays fabricated on flexible polycarbonate sheets via single-step laser interference ablation," *Journal of micromechanics and microengineering,* vol. 21, p. 015010, 2011.

[120] M. Malinauskas, H. Gilbergs, A. Zukauskas, V. Purlys, D. Paipulas, and R. Gadonas, "A femtosecond laser-induced two-photon photopolymerization technique for structuring microlenses," *Journal of optics (2010),* vol. 12, p. 035204, 2010.

[121] E. Schonbrun, P. E. Steinvurzel, and K. B. Crozier, "A microfluidic fluorescence measurement system using an astigmatic diffractive microlens array," *Optics express,* vol. 19, p. 1385, 2011.

[122] D. A. Chang-Yen, R. K. Eich, and B. K. Gale, "A Monolithic PDMS Waveguide System Fabricated Using Soft-Lithography Techniques," *J. Lightwave Technol.,* vol. 23, p. 2088, 2005.

[123] B. Neumann, M. Held, U. Liebel, H. Erfle, P. Rogers, R. Pepperkok, and J. Ellenberg, "High-throughput RNAi screening by time-lapse imaging of live human cells," *Nature Methods,* vol. 3, p. 385, 2006.

[124] K. Handique, D. T. Burke, C. H. Mastrangelo, and M. A. Burns, "Nanoliter Liquid Metering in Microchannels Using Hydrophobic Patterns," *Analytical chemistry* vol. 72, pp. 4100-4109, 2000.

[125] J. W. Suk and J. Cho, "Capillary flow control using hydrophobic patterns," *Journal of micromechanics and microengineering,* vol. 17, pp. N11-N15, 2007.

[126] L. Riegger, M. M. Mielnik, A. Gulliksen, D. Mark, J. Steigert, S. Lutz, M. Clad, R. Zengerle, P. Koltay, and J. Hoffmann, "Dye-based coatings for hydrophobic valves and their application to polymer labs-on-a-chip," *Journal of micromechanics and microengineering,* vol. 20, p. 045021, 2010.

[127] P. Sethu, M. Anahtar, L. L. Moldawer, R. G. Tompkins, and M. Toner, "Continuous Flow Microfluidic Device for Rapid Erythrocyte Lysis," *Analytical chemistry,* vol. 76, pp. 6247-6253, 2004.

[128] C. Lee, C. Chang, Y. Wang, and L. Fu, "Microfluidic Mixing: A Review," *International journal of molecular sciences,* vol. 12, pp. 3263-3287, 2011.